Physical and Chemical Properties of Carbon Nanotubes and Silica Nano-Composites on the Photo-Catalytic Activity of Titania Nanoparticles for Selected Organic Pollutants

By

Nteseng Ouma Ramoraswi

Submitted in fulfilment of the academic requirements for the degree of Master of Science in the School of Chemistry and Physics University of KwaZulu-Natal Durban

November 2014

As the candidate's supervisor I have approved this dissertation for submission.

Signed Name Date

Preface

This thesis describes experimental work that was carried out in the School of Chemistry at University of KwaZulu-Natal, Durban, South Africa, from February 2013 to November 2014, under the supervision of Dr Patrick G. Ndungu.

These studies present original work by the author and have not been submitted in any form for any qualification, degree or diploma at any tertiary institution. Where use has been made of the work of others, it is accordingly acknowledged in the text.

This dissertation has been prepared according to the format outlined in the guidelines from the College of Agriculture, Engineering and Science of UKZN, (FHDR Approved 13 March 2007).

Declaration 1 – Plagiarism

I, Nteseng Ouma Ramoraswi declare that:

1. The research reported in this thesis, except where otherwise started, is my original work.

2. This thesis has not been submitted for any degree or examination at any other university.

3. This thesis does not contain other persons' data, pictures, graphs or other information, unless specifically acknowledged as being sourced from other persons.

4. This thesis does not contain other persons' writing, unless specifically acknowledged as being sourced from other researchers. Where other sources have been quoted then:

    - Their words have been re-written but the general information attributed to them has been referenced.
    - Where their exact words have been used, then their writing has been placed in italics and inside quotation marks, and referenced.

5. This thesis does not contain text, graphics or tables copied and pasted from the Internet, unless specifically, and the source being detailed in the thesis and in the reference sections.

Signed Date

Declaration 2 – Presentations

1. Nteseng O. Ramoraswi and Patrick G. Ndungu. 2013. Photo-catalytic properties of titania nanoparticle supported on silica/carbon nanotubes nanocomposite. Cataysis Society of South Africa (CATSA) conference. Wild Coast Sun, Port Edward, South Africa, November 17-20, 2013.

2. Nteseng O. Ramoraswi and Patrick G. Ndungu. 2014. Physico-chemical properties of titania nanoparticle supported on silica coated carbon nanotubes. 5th International IUPAC Conference on Green Chemistry. Durban, South Africa, August 17-20, 2014.

3. Nteseng O. Ramoraswi and Patrick G Ndungu. 2014. Photo-catalytic properties of supported TiO_2 nano-particles. College of Agriculture, Engineering and Science Postgraduate Research Day. Durban, South Africa, 27 October 2014.

Signed Date

Abstract

High surface area materials were synthesized in order to support titanium dioxide (TiO_2) photo-catalysts with the aim of enhancing the overall photo-catalytic properties of the catalyst. Mesoporous silica dioxide (SBA-15), multi-walled carbon nanotubes (CNTs), and silica dioxide coated multi-walled carbon nanotubes (SBA-CNTs) were prepared using a sol-gel method with structure directing agents (surfactants) to ensure mesoporosity and maximize the available surface area. A loading of 10 wt. % TiO_2 was chosen to study the effects of the supports, SBA-15, CNTs and 30 wt. % SBA-CNT composite respectively. Physical and chemical properties of the materials were evaluated with Transmission electron microscope (TEM); high resolution electron microscope (HRTEM); scanning electron microscope (SEM); powder x-ray diffraction (XRD); thermo-gravimetric analysis (TGA); Nitrogen (N_2) sorption; Raman spectroscopy; UV-Vis Diffuse reflectance spectroscopy; Fluorescence spectroscopy; and UV-Vis spectroscopy.

Photo-catalytic properties of the materials were tested using a 10 mg L^{-1} methylene blue (MB) dye solution. The best photo-catalytically performing material (10 wt. % TiO_2/SBA-CNT) was identified and regarded as an optimum catalyst composite for further studies to be conducted. The effect of TiO_2 loading (5 and 20 wt. % TiO_2 on SBA-CNT composite) was studied, and the physical-chemical properties of the catalyst were further evaluated and tested on MB de-colorization experiments. The activity of the most efficient catalyst in the MB test was further evaluated on the degradation of 2-chloro-4-methylphenoxyacetic acid (MCPA) herbicide, a known real-world refractory organic pollutant. High performance liquid chromatography (HPLC) with a DAD detector was employed for the quantitative analysis of the herbicide degradation.

The study of different substrates showed that the efficiency of the photo-catalyst was highly influenced by the pollutant structure as opposed to the physical-chemical properties of the catalyst system.

Additionally, these studies showed that composites of TiO_2 with electron trapping species such as CNTs reduce one of the core problems associated with TiO_2 semiconductor which is electron – hole recombination rate. Plus the composite offer the advantage of using the catalyst under visible light energy and the catalyst can be employed to degrade organic pollutants in solution medium.

Keywords:
Titanium Dioxide, ordered mesoporous silica, carbon nanotube, carbon nanotube metal oxide nanocomposites, photo-catalysis, methylene blue, MCPA.

Acknowledgements

To God be the glory in all things. I thank God for His sufficient Grace and everlasting love in my life.

Foremost, I would like to appreciate my supervisor, Dr P.G. Ndungu for his mentorship. Through him I have withdrawn so much wisdom, love and understanding of what was once a boring subject (Physical Chemistry).

I am grateful to the Central Teaching Office and technical team in the School of Chemistry at UKZN. To the microscopy unit team, thank you so much for introducing me to the use of all microscopy techniques employed in this work. I appreciate the help of iThemba Labs for the powder X-ray diffraction pattern data. Thank you to the PhysChem laboratory mates for walking with me through this path of academic growth.

I sincerely appreciate the roles played by Ekemena, Mothusi, Bheki and Lucy, you guys have made coping with the hardships of research seem easy at times. Your presence through this journey will forever be acknowledged and appreciated. I would love to appreciate the bible interaction team, for all the word of encouragement and empowerment. I cannot forget my childhood friends who have been a part of my life and development, thank you all good friends.

My sincere gratitude goes to my family, mother Mokgadi and sisters (Minah, Ntebatje and Mahlatse), who have been the pillars of my strength. I am grateful for the faith you had in me and for the opportunity to begin and end this study program. I cannot forget the support and patience of Skhu. I owe my loving appreciation to my son, Bosele, you have been the beautiful end to each hard day I have ever endured through this study. Thank you for pretending to understand my absence and thank you for being strong.

This work would not have been possible without the financial support of National Research Founding (NRF) and University of KwaZulu-Natal. Thank you.

Dedication

This dissertation is dedicated to my lovely son Bosele M. Ramoraswi.

Table of Contents

List of Figures

List of Tables

Abbreviations

TiO_2	Titanium Dioxide
TEOS	Tetraethyl orthosilicate
MWCNTs	Multi-walled carbon nanotubes
P123	Poly(ethylene glycol)-block-poly(propylene glycol)-block-poly(ethylene glycol) P123
F127	Poly(ethylene glycol)-block-poly(propylene glycol)-block-poly(ethylene glycol) F127
TIP	Titanium (IV) isopropoxide
aCNTs	Acid treated multi-walled carbon nanotubes
rCNTs	Pristine multi-walled carbon nanotubes
SBA-15	Santa Babara Acid (Mesoporous Silica Dioxide)
MCPA	4-chloro-2-methylphenoxy acetic acid
MB	Methylene blue
SEM	Scanning Electron Microscope
TEM	Transmission Electron Microscope
HRTEM	High Resolution Transmission Electron Microscope
XRD	X-Ray Diffraction
TGA	Thermo-gravimetric Analysis
N_2 sorption	Nitrogen Adsorption-Desorption
ICP-OES	Inductively induced plasma - optical emission spectroscopy
HPLC	High Performance Liquid Chromatography
UV-Vis	Ultra Violet Visible
W	Watt
Wt.	Weight
a.u	Arbitrary units
e -h	Electron - hole
≈	Almost equal to
p.	Page

Chapter 1
Introduction

Clean water and sanitation are a basic need and fundamental right (United Nations Resolution 64/292) for all human kind [1]. The World Health Organization (WHO)/UNICEF Joint Monitoring Programme defined basic sanitation as "the lowest cost technology ensuring hygienic excreta and sewage disposal, a clean and healthy living environment both at home and in the neighbourhood of all users" [2]. The definition points to the significance of safe, accessible and sustainable waters. It has been reported, statistically, that the world population is expected to reach up to 9.3 billion in the next three centuries, with the global consumption of water doubling every 20 years, which is more than twice the rate of human population growth [1, 3]. Furthermore, the Solar Disinfection of Drinking Water (SODISWATER) project reported that globally a billion people lack access to safe water while 2.6 billion people have no access to basic sanitation [4]. These numbers are expected to grow rapidly over the coming years as a result of population growth, pollution and persistent water contamination.

1.1 Background

Water contamination is mainly attributed to anthropogenic activities either through industrialization, commercial endeavours, or from domestic activities [5]. Industrial wastewater effluents such as dyes, pharmaceuticals, oils plus various hydrocarbons, and metals are amongst the largest contributors to aquatic body contamination. Agricultural pesticides can and often do find their way into surface, ground, and drinking waters over time, especially after their use for agricultural purposes [6, 7]. The variety of pollutants, the different levels of toxicity and persistence can present risk to the health of the ecosystem and humans in general [8]. As such, degrading them into less toxic or completely mineralized products is crucial. Various methods have been proposed and studied as means of de-polluting water bodies, such as, adsorption, membrane filtration, ion exchange, and chemical coagulation amongst others. However, these methods have limitations.

For instance adsorption and coagulation methods simply transform the target pollutants into different phases that are still not completely destroyed [9], while sedimentation, filtration, and chemical treatment methods operate at high costs and are likely to generate toxic secondary pollutants [10]. These drawbacks require additional treatment and increases cost in recycling water. On the other hand the most common and widely used disinfection process, chlorination, is reported to produce by-products that are mutagenic and carcinogenic [11-13].

A promising route that can be low cost with less negative effects is nanotechnology in the form of Heterogeneous Photo-catalytic Oxidation (HPO). This method has gained favor over the other methods because of its ability to destroy a wide range of pollutants over time. The technology involves use of a hydrophilic semiconductor such as nano titanium dioxide (TiO_2) as the catalyst, UV light and/or visible light as the energy source and an oxidizing agent such as oxygen or air [8, 14]. HPO becomes even more affordable and advantageous when sunlight is used as the source of irradiation. **Figure 1.1** illustrates the basic principle in photo-catalytic oxidation reactions in an aqueous solution.

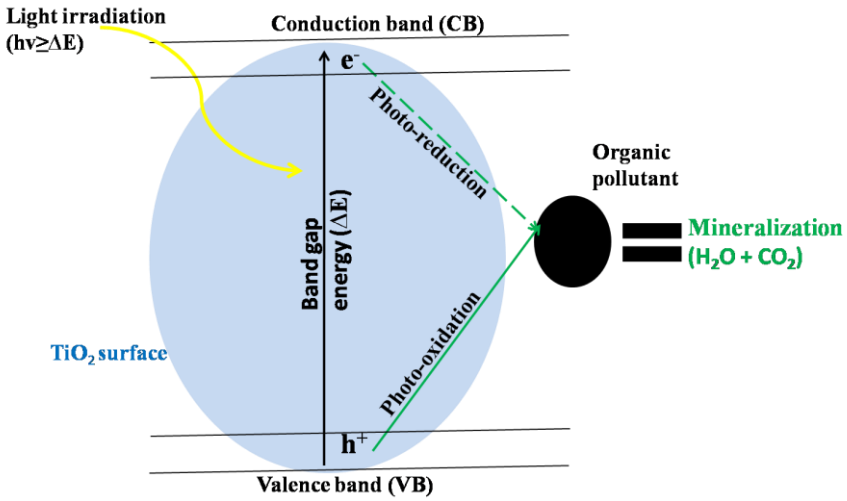

Figure 1. 1 Schematic diagram of TiO_2 nanoparticle photo-catalyst.

The principle is believed to be that a semiconductor (TiO_2) surface is excited by light irradiation through photons (hv) that are equal or higher in energy than the catalyst band gap energy (ΔE).

The excitation promotes an electron from the valence band to the conduction band, and then generates an electron-hole pair which undertakes either one or both the photo-oxidation or photo-reduction route. These routes may undergo a series of reactions before eventually producing hydroxyl radicals and oxidative holes, which are species important in photo-induced reactions [10, 15]. This route effectively degrades persistent organic pollutants while producing more biologically degradable and less toxic by-products such as CO_2 and H_2O [8, 16].

It is important to note that there are several other heterogeneous photo-catalyst semiconductors such as ZnO_2, ZnS, WO_3, and $SrTiO_3$ to name a few [17], although TiO_2 has received much research attention as a photo-catalyst semiconductor. The interesting physical and chemical properties of TiO_2 afford it to be tailored during synthesis at a molecular level and thus enhance its photo-catalytic efficiency, especially under visible light irradiation. The possibilities of using green chemistry principles to fabricate an effective TiO_2 catalyst make it even more interesting to study. In this study the fabrication, modification effects and use of a visible region active TiO_2 nano-catalyst semiconductor photo-catalyst is investigated. This is to degrade and mineralize methylene blue as the model dye for industrial effluents and 4-chloro-2-methylphenoxy acetic acid (MCPA) herbicide as a refractory pollutant generated from the agricultural industry. Selective herbicide MCPA is commonly used for control of annual perennial weeds in cereal, grassland and turf throughout the year worldwide.

1.2 Problem Statement

Water scarcity and pollution are global concerns that call for innovative methods for the preservation and de-pollution of water resources. Main causes of water pollution are attributed to commercial and industrial activities, which release wastewaters that may contain dyestuffs, agricultural pesticides or other types of organic or inorganic pollutants. These pollutants can find their way to surface, ground, or drinking waters over time. Organic pollutants are of growing concern because there are hundreds of new chemicals being produced on a regular basis for various commercial reasons (emerging organic pollutants), or can be persistent within the environment.

1.3 Aims and Objectives

The aim of this project was to develop inexpensive nanomaterials which would effectively degrade toxic dyestuffs (methylene blue) and pesticides such as MCPA through heterogeneous photo-catalysis using modified anatase titanium dioxide (TiO_2) photo-catalyst, that can operate in the visible region of the spectrum.

To achieve the aim, the objectives were carried out as follows:

1. Synthesize and modify supporting frameworks for titania nano-particles.
2. Synthesize mesoporous anatase phase TiO_2 catalysts using sol-gel chemistry.
3. Synthesize nano-composites of TiO_2 particles on different supports (multi-walled carbo nanotubs (MWCNTs), ordered mesoporous silica (SBA-15) and SBA-15 coated MWCNTs).
4. Characterize the synthesized materials and investigate their physical and chemical properties.
5. Evaluate the activity of the photo-catalysts on the degradation of the organic pollutants of interest (methylene blue and MCPA).

1.4 Research Approach

Sol-gel methods assisted by surfactants were used to prepare mesoporous TiO_2, supports and TiO_2 composites. Physical and chemical properties of the materials were studied before conducting photo-catalytic tests. This study will focus on the characteristics of the supports and the catalyst materials prepared by the sol-gel methods. The photo-catalytic experiments were employed to understand the influence of the physical and chemical properties of materials during heterogeneous oxidation catalysis.

1.5 Research Scope

The work within the thesis focuses on material preparation, characterization and modifications. Materials will only be prepared through the sol-gel methods. Photo-catalytic studies will evaluate the degradation efficiency of the various catalysts before and after irradiation with visible light. The operating parameters such as pH, catalyst concentration and pollutant concentration will be optimized during the degradation of the organic pesticide.

1.8 References

1. Human Right Counsel, United Nation, *Human rights and access to safe drinking water and sanitation* (A/HRC/15/L.14). 2010.
2. Gupta, J., Ahlers, R. and Ahmed, L., *The human right to water: moving towards consensus in a fragmented world.* Review of European Community & International Environmental Law, 2010. **19**(3): p. 294-305.
3. Han, F., Kambala, V. S. R., Srinivasan, M., Rajarathnam, D. and Naidu, R., *Tailored titanium dioxide photocatalysts for the degradation of organic dyes in wastewater treatment: A review.* Applied Catalysis A: General, 2009. **359**(1–2): p. 25-40.
4. SODISWATER, Solar Disinfection of Drinking Water for use in Developing Countries or in Emergency Situations. 2010 (European Union Contract Number FP6 2006 INCO-DEV 031650).
5. Kanu, I. and Achi, O., *Industrial effluents and their impact on water quality of receiving rivers in Nigeria.* Journal of Applied technology in Environmental sanitation, 2011. **1**(1): p. 75-86.
6. Agrawal, A., Pandey, R. S. and Sharma, B., *Water pollution with special reference to Pesticide Contamination in India.* Journal of Water Resource and Protection, 2010. **2**(5): p. 432-448.
7. Wauchope, R., The pesticide content of surface water draining from agricultural fields—a review. Journal of environmental quality, 1978. **7**(4): p. 459-472.
8. Ahmed, S., Rasul, M. G., Martens, W. N., Brown, R. and Hashib, M. A., *Heterogeneous photocatalytic degradation of phenols in wastewater: A review on current status and developments.* Desalination, 2010. **261**(1–2): p. 3-18.
9. Padmanabhan, P. V. A., Sreekumar, K. P., Thiyagarajan, T. K., Satpute, R. U., Bhanumurthy, K., Sengupta, P., Dey, G. K. and Warrier, K. G. K., *Nano-crystalline titanium dioxide formed by reactive plasma synthesis.* Vacuum, 2006. **80**(11-12): p. 1252-1255.

10. Gaya, U. I. and Abdullah, A. H., *Heterogeneous photocatalytic degradation of organic contaminants over titanium dioxide: A review of fundamentals, progress and problems*. Journal of Photochemistry and Photobiology C: Photochemistry Reviews, 2008. **9**(1): p. 1-12.
11. Chong, M. N., Jin, B., Chow, C. W. K. and Saint, C., *Recent developments in photocatalytic water treatment technology: A review.* Water Research, 2010. **44**(10): p. 2997-3027.
12. Yang, H. and Cheng, H., *Controlling nitrite level in drinking water by chlorination and chloramination.* Separation and purification technology, 2007. **56**(3): p. 392-396.
13. Lu, J., Zhang, T., Ma, J. and Chen, Z., *Evaluation of disinfection by-products formation during chlorination and chloramination of dissolved natural organic matter fractions isolated from a filtered river water.* Journal of Hazardous Materials, 2009. **162**(1): p. 140-145.
14. Ibhadon, A. O. and Fitzpatrick, P., *Heterogeneous Photocatalysis: Recent Advances and Applications.* Catalysts, 2013. **3**(1): p. 189-218.
15. Carp, O., Huisman, C. L. and Reller, A., *Photoinduced reactivity of titanium dioxide.* Progress in Solid State Chemistry, 2004. **32**(1–2): p. 33-177.
16. Rauf, M., Meetani, M. and Hisaindee, S., *An overview on the photocatalytic degradation of azo dyes in the presence of TiO_2 doped with selective transition metals.* Desalination, 2011. **276**(1): p. 13-27.
17. Pirkanniemi, K. and Sillanpää, M., *Heterogeneous water phase catalysis as an environmental application: a review.* Chemosphere, 2002. **48**(10): p. 1047-1060.

Chapter 2
Literature Review

2.1 General Introduction to Titanium Dioxide

Titanium Dioxide (TiO_2) is amongst the most widely studied metal oxides, it t is a simple, well characterized and inexpensive semiconductor [1]. It has intriguing properties that make it an ideal photo-catalyst. It is a very chemically stable material which can generate highly oxidizing (photo-generated) holes. This relatively high surface area semiconductor, with a band gap of 3.0 – 3.4 eV, can be considered nontoxic and is widely available, since its parent metal, titanium (Ti) is the world's fourth most abundant metal and the ninth most abundant element [2]. Ti is found in almost all rocks and sediments; it is also present in plants, natural waters and animals [3].

Titanium ore refers to a natural or industrial resource that can be used as raw (feedstock) material to produce titanium dioxide or titanium metal. The most common ores for TiO_2 production are mined from nature as ilmenite, rutile, anatase, titanomagnetite and leucoxene [4, 3]. Rutile and ilmenite are the most economic minerals for TiO_2, with ilmenite contributing about 91% of the world's use of titanium minerals. It is interesting to note that only 5% of the mined minerals contribute to metal production, while 95% contributes to titanium dioxide (TiO_2) pigment [5].

South Africa (SA) is reported to be the second largest producer of titanium containing minerals in the globe after Australia. Countries such as Sri Lanka, USA and India also contribute to the production of more than half of the world's titanium from ilmenite and rutile [5]. The South African Richards Bay Mine (RBM) employs the dredge mining operation to extract and separate TiO_2 minerals. Approximately 95% of the TiO_2 mineral concentrates are sold from SA to the international markets [5, 3]. Further processes following either the sulphate or the chloride process would be considered to produce the TiO_2 pigments, or alternatively the Kroll process to produce the titanium metal [3, 6, 7].

Ti metals are widely used in the chemical, petrochemical and the heat exchanger industries. Commercially, Ti metal is used in tennis rackets, electronics, jewelry, and as an artificial hip in the medical sector [3]. Whereas TiO_2 has found use in various industries such as, the food industry where TiO_2 is used as a food coloring agent [8], and the textile industry where TiO_2 is used to dye synthetic fibers. In the pharmaceutical sectors, TiO_2 is used as a block for UV radiation in sunscreens, and it is also used as a pigment for various pills and syrups [9]. Several cosmetic and personnel care products such as ointments, toothpaste, shampoos, lipsticks, hair dyes and lotions amongst others, contain TiO_2. TiO_2 is also used as a pigmentation agent for paper and printing inks because of its whitening properties and opacifying ability [0].

Current research developments on TiO_2 include the development of nano-structured titanium dioxide materials. These materials are developed for applications in energy, cancer treatment, self-cleaning surfaces and clothes, environmental remediation studies, water treatment and catalysis. TiO_2 nano-particles are the most studied materials in photo-catalytic studies because the particles can break down organic compounds and destroys various water microorganisms [11-13].

2.1.1 Crystalline Structure of Titanium Dioxide

TiO_2 exists in different crystalline forms, the common forms are rutile (band gap 3.0 eV) and anatase (band gap 3.2 eV). Anatase is the most stable form, and can be transformed to rutile by heating to temperatures above 600 ˚C [14]. Most studies have shown that brookite, a third thermodynamically stable crystalline form of TiO_2, is the least common and studied form [15, 16, 2, 17-19, 12]. In all TiO_2 crystals, the basic building block consists of a titanium atom clustered by six oxygen atoms (TiO_6) in a distorted octahedral configuration. The stacking of the octahedral building blocks results in a three-fold coordinated oxygen atoms. The distinctive feature in these crystals is the modes of arrangement and links of the TiO_6 octahedra [20, 4]. **Figure 2.1** illustrates the three major crystalline forms of TiO_2 resulting from the TiO_6 octahedra arrangement. The most employed and photoactive commercial TiO_2 is Degussa P25, it constitutes approximately 25% rutile and 75% anatase. P25 has been employed a lot in photo-catalytic studies and it has been suggested as reference material for such studies [15].

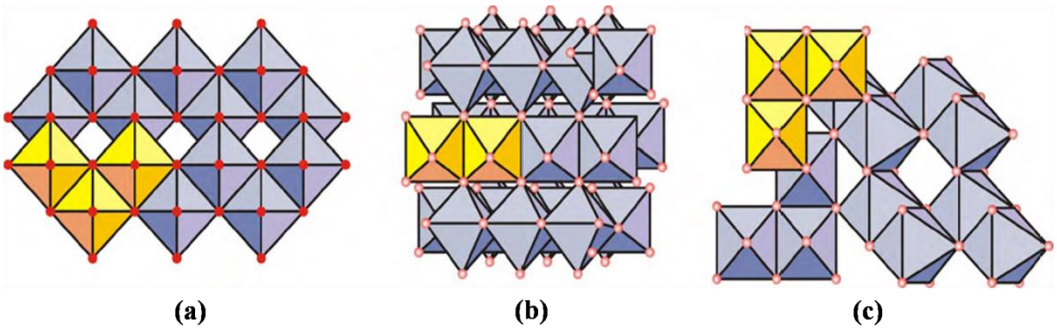

Figure 2. 1 TiO_6 octahedra arrangement in anatase (a), brookite (b) and rutile (c) [4].

The different phases of titania can be differentiated through characterization techniques such as powder X-ray diffraction (XRD) and/or Raman spectroscopy. For instance, with XRD, characteristic peaks of the phases of titania are well known and can be found within readily accessible databases, such as the Joint Committee on Powder Diffraction Standards (JCPDS), International Center for Diffraction Data. Anatase titania is identified by an intense diffraction peak at approximately $2\theta = 26^{\circ}$, rutile phase gives off sharp diffractions at $2\theta = 28$ and 55° and brookite diffracts intensely at $2\theta = 25^{\circ}$. JCPDS cards 21-1272, 21-1276 and 03-0380 are available for anatase, rutile and brookite respectively. Raman spectroscopy complements XRD through vibration modes which are typical for characteristic phase of metals. The experimental section (**Chapter 3, section 3.7**) will give more information on the instruments and descriptions for their use. Industrially, TiO_2 powders are common, however, current research and development is focused on nano-structural designs, properties and preparation methods.

2.2 Morphology and Synthetic Approaches to Nanostructured Titanium Dioxide

TiO_2 nanostructures can be prepared in the form of powder [21], thin films [22], or crystals. Powder and thin film forms can be built up from crystallites in the nanometer (10^{-9} m) to micrometer (10^{-6} m) range. Nanosized crystallites usually form agglomerated particles. Nanostructure shapes are not limited to nanoparticles but also includes nanofibres, nanotubes, nanocombs, nanorings, nanosprings, nanobelts, nanosheets and nanorods [23].

Various synthestic routes exist amongst the gas phase route and the solution route. The gas phase route includes techniques such as the chemical vapor deposition (CVD), physical vapor deposition (PVD) and spray pyrolysis deposition (SPD). In the solution route, methods such as (co-) precipitation, solvothermal, electrochemical synthesis and the sol-gel methods are common [2]. The solution methods, especially sol gel, are more advantageous because they offer control over stoichiometry, produces homogeneous material, and allow for formation of complex shapes and composite materials unsupported or supported on various substrates [2, 17, 24].

Ward and Ko [25] highlighted the potential advantages of the sol-gel method which are (i) the ability to control structure and composition at a molecular level, (ii) the ability to introduce several components in a single step, (iii) the ability to impose kinetic constraints on a system and thereby stabilize metastable phases, and (iv) the ability to fine tune the activation behaviour of a sample and thereby trace the genesis of active species. To date many other reviews are evident to contribute to the sol-gel chemistry on different materials [26]. The sol-gel methods afford the synthesis of mesoporous TiO_2 nano-particles, fibers and tubes. Two types of routes are common, the non alkoxide and the alkoxide route. The non alkoxide route employs inorganic salts and the alkoxide route employs metal oxides as starting material. Generally sol-gel chemistry involves two key steps, first is the formation of a gel or sol as a result of slightly hydrolyzed species or precipitation. The gel structure forms into a three dimensional polymeric network. Second is the condensation of the precursor (metal alkoxide), a phase whereby the gel undergoes phase change that will give the material its properties [27-30]. At this stage a lot of sol parameters play a crucial role, parameters such as type of precursor used, type of solvent; water content, acid or base content; precursor concentration, temperature, and ageing period.

To gain control on the material properties (pore size, pore geometry, wall thickness, porosity, thermal stability, and crystal size) the hydrolysis and condensation phases need to be separated [29, 31-33, 30]. Several approaches have been adopted and include modifying the alkoxide with complex coordination ligands that hydrolyze slower than the alkoxide ligand [27]. Base catalysis can also be used to separate the hydrolysis and condensation steps in sol-gel chemistry. Base catalysis is thought to promote condensation and ultimately forms amorphous material.

Meanwhile, acid catalysis promote hydrolysis and eventually form crystalline materials from fully hydrolyzed precursor [2]. Recently Debecker and co-workers [34] reviewed the non-hydrolytic sol-gel (NHSG) routes for the preparation of mixed mesoporous oxide catalyst. Their scope revolved on the processes based on the reaction of chloride precursors with ether or alkoxide oxygen donors. The NHSG route affords the synthesis of mesoporous materials without the use of structure directing agents and supercritical drying conditions, as a result the route is unable to produce ordered arrays of pores. It becomes important then to employ additives in order make structured porous TiO_2, which could also improve porosity, order, physical and chemical properties of the material.

2.2.1 Templates for Mesoporous TiO_2 Fabrication

Recently advances have been made in synthesizing ordered mesoporous TiO_2 crystals with high surface area through coupling the sol-gel and templating synthetic methods. Templates are structure directing agents which can be surfactants, polymers or inorganic particles. They can be eliminated after use via thermal treatment, washing, or chemical treatment. Synthesis of mesoporous TiO_2 with different mesostructures, and the resultant differing physical and chemical properties have been explored through the use of different structure directing agents, precursors and synthetic chemistry (**Table 2.1**). Ionic, neutral and block copolymers have been successfully used as templates to direct the formation of titanium dioxide mesopores.

Table 2. 1 Synthesis reagents, post treatment and material properties of mesoporous TiO_2.

Ti precursor	Template	Surface area (m^2 g^{-1})	Method for template removal	Ref.
Titanium isopropoxide (TIP)	Tetradecyl-phosphate	150 - 200	Calcination and solvent extraction	[35]
$Ti(OPr^i)_4$; $Ti(OEt)_4$; $Ti(OBu^t)_4$	P123	333 - 383	Boiling ethanol under reflux	[36]
Tetrabutyl titanate (TBT)	Urea-alcohol	224 - 276	Distilled H_2O (3 days); oven dry at 100 ˚ C.	[37]
TIP	P123	N/A	Oxygen and Argon plasma etching technique	[38]
Tetra (*i*-propyl) orthotitanate	Alkylamine	170 - 215	Washed with i-propanol; calcination	[39]

Early studies on mesoporous titanium dioxide include work by Peres-Durand et al. [40], where a gel was prepared by dissolving TIP into a solution of decane/TX35/H_2O or H_2O_2. The surfactant in this composition was Triton-X35 and the gel was aged for three months before washing and drying. Antonelli D M [41] reported what was proposed to be the first non-phosphated mesoporous titanium dioxide through use of ligand-assisted templating, and dodecylamine as the structure directing agent. The results of their work led to an ordered but amorphous material. This report followed an earlier report from same authors on a ligand assisted strategy which brought about limitations since that earlier procedure could only work for surfactants with phosphate head groups.

Micellar surfactant, alkylamine, were employed by Koshitani et al. [39] to fabricate anatase titania nanocrystals. Mesoporous titania spheres were synthesized from the use of triblock copolymer surfactants P123 and F127 with titanium (IV) isopropoxide [42, 43]. Calleja et al. [36] studied the effect of solvent system, type of precursor, precursor: surfactant ratio with an anionic surfactant P123 system to synthesis and study the physical chemical properties of ordered mesoporous TiO_2. Cetyl trimethylammonium bromide (CTAB) has been employed successfully to fabricate mesoporous titanium structure with good physical and chemical properties [44]. Song et al. [45] also employed CTAB to direct the pore geometry of titania based materials. Structure directing agents such as hydroxypropyl cellulose (HPC) and diblock copolymer PEO-*b*-PS have also been reported to yield ordered mesoporous titania [46, 47].

One of the most significant applications of mesoporous TiO_2 are in photo-catalysis, and include its use as a photo-catalyst for cancer treatments [48], self-sterilizing, self and air cleaning [49, 13], cosmetics [50] and environmental (water and air) purification [51-53, 17, 19]. Of the various applications, the most active field of TiO_2 photo-catalyst is in the degradation of organic compounds in waters [19, 2, 15]. Effective organic pollutant degradation in water can be achieved by the use of a TiO_2 photo-catalyst, a light source, and an oxidizing agent (air or oxygen). The desired end products of the process should be biologically degradable and substances with less toxicity than the parent material, ideal degradation products should be H_2O and CO_2 [52].

2.3 Principle of TiO_2 in Heterogeneous Photo-catalysis

Heterogeneous photo-catalytic oxidation includes the transfer of reactants (pollutants) in the aqueous media onto the surface of the catalyst. The reactants get adsorbed on the catalyst surface and various reactions take place, then desorption of the final product and finally removal of the final products in the aqueous media [1]. An idealized scheme that summarizes the mechanism of degradation on the surface of TiO_2 is presented in **Figure 2.2**.

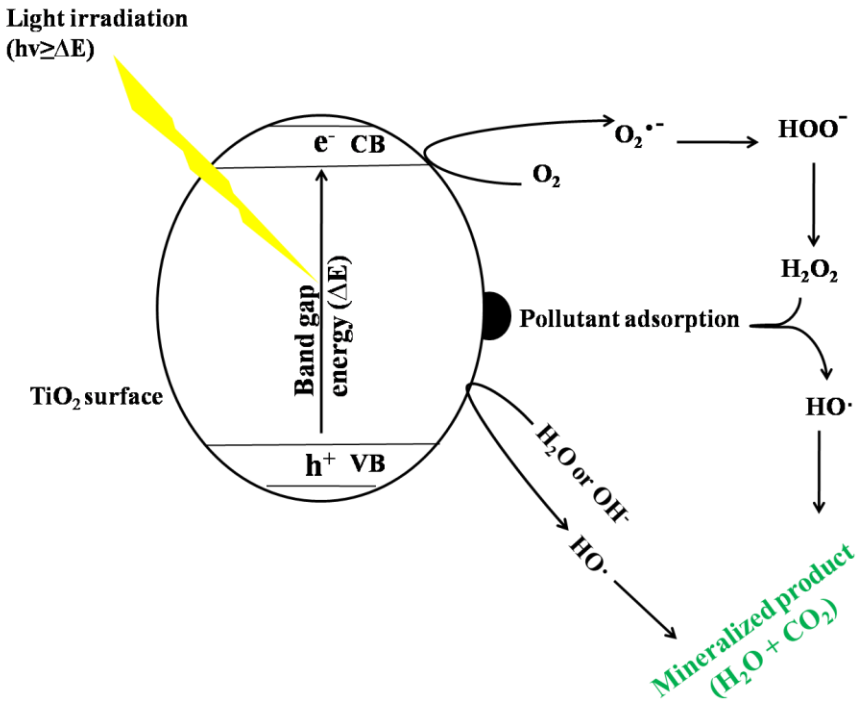

Figure 2. 2 Schematic diagram illustrating the photo and chemical activities that take place on the surface of TiO_2 in an aqueous solution in the presence of an organic pollutant and light irradiation.

When photons of higher or equal energy than the band gap are incident on the photo-catalyst surface, they are absorbed. This causes electrons in the valence band to be excited and promoted to the conduction band (cb) [54].

$$\text{Catalyst} + h\nu \rightarrow e^-_{cb} + h^+_{vb} \qquad (2.1)$$

Migration of electrons causes vacant holes in the valence band (vb), the holes are highly oxidative, once they reach the surface of the particle. At the surface, oxidizing agents (hydroxyl radicals and superoxide anions) are also generated. Often, h^+_{vb} reacts with surface bound water (H_2O) to produce hydroxyl radicals ($^{\cdot}OH$), whereas e^-_{cb} are responsible for the production of superoxide radical anion of oxygen from the reaction with O_2.

$$h^+_{vb} + H_2O \rightarrow {}^{\cdot}OH + H^+ \qquad (2.2)$$

$e^-_{cb} + O_2 \rightarrow O_2^{\bullet -}$ (2.3)

The above reactions (2.2 and 2.3) delay the rate of recombination of the e^-_{cb} and h^+_{vb} which are produced in reaction (2.1). The generated species ($^{\bullet}OH$ and $O_2^{\bullet -}$) can react with any pollutant that may be present to form other species and to eventually degrade the pollutants to various products.

$^{\bullet}OH$ + pollutant = Oxidation products (2.4)

$O_2^{\bullet -}$ + pollutant = Reduction products (2.5)

It is important to note that water molecules and dissolved oxygen aid in the generation of the highly reactive hydroxyl radicals [1]. In a nutshell, the excited electrons and hydroxyl radicals can be used to drive the degradation of harmful organic compounds (photo-catalytic reactions) [15, 2, 55]. Possibilities of undesired side reactions do exist, for instance, recombination of the electron-hole may occur and give off the adsorbed energy as heat. In such cases, the adsorbed species does not react, thus degradation of organic pollutants cannot be achieved.

2.4 Operational Factors that Influence Photo-catalytic Efficiency of TiO_2

Photo-catalytic degradation is influenced by various operational parameters. The parameters are discussed in the subsequent section. Their importance suggests that preliminary experiments should be conducted in order to find optimal conditions for each parameter during the degradation of pollutants of interest.

2.4.1 Catalyst makeup

The photo-catalytic activity of TiO_2 is dependent on the physical and chemical properties of the catalyst. Properties of particular significance include crystal composition, surface area, surface defects, particle size distribution, porosity, the energy of the band-gap, and surface hydroxyl density. In heterogeneous catalysis particle size is critical to consider since it is related to the efficiency of catalyst through its definition of specific surface area [52].

Often the difference in photo-catalytic activity is related to the variation of the specific surface area, degree of structural defects in the crystalline framework, impurities, or density of hydroxyl groups on the catalyst surface [56].

2.4.2 Light intensity and wavelength

Light intensity (Wm^{-2}) facilitates the initial rate of electron-hole formation, the initiator step in photo-catalytic reactions and it determines the extent of light absorbed by the catalyst at a particular wavelength [52]. Futjishima et al. [19] investigated the effect of low light intensity on the decomposition of organic pollutants and postulated that TiO_2 photo-catalysis depends on the energy of the incident photons rather than on their light intensity. However, in water treatment, a high light intensity is required to sufficiently provide the surface of the nano-particle active site with the necessary photon energy [11]. Kaneco et al. [57] observed a rapid increase of degradation efficiency of bisphenol A when light intensity was increased.

Light wavelength affects the photo-catalytic reaction rate, depending on the catalyst type (crystallinity). The crystal structure, physical and chemical composition of the material influences the band gap energy of the catalyst; hence different kinds will require different wavelengths of light. For instance, Degussa P25 TiO_2 is sufficiently photo activated by a light with a wavelength of $\lambda < 380$ nm because it is made of anatase and rutile crystal phases in a (80:20) ratio. Though, the rutile TiO_2 with band gap energy of 3.02 eV would be sufficiently photo activated by light with a wavelength of up to 411 nm [55, 11]. **Figure 2.3** demonstrates the common TiO_2 phases and the wavelengths required to initiate excitation.

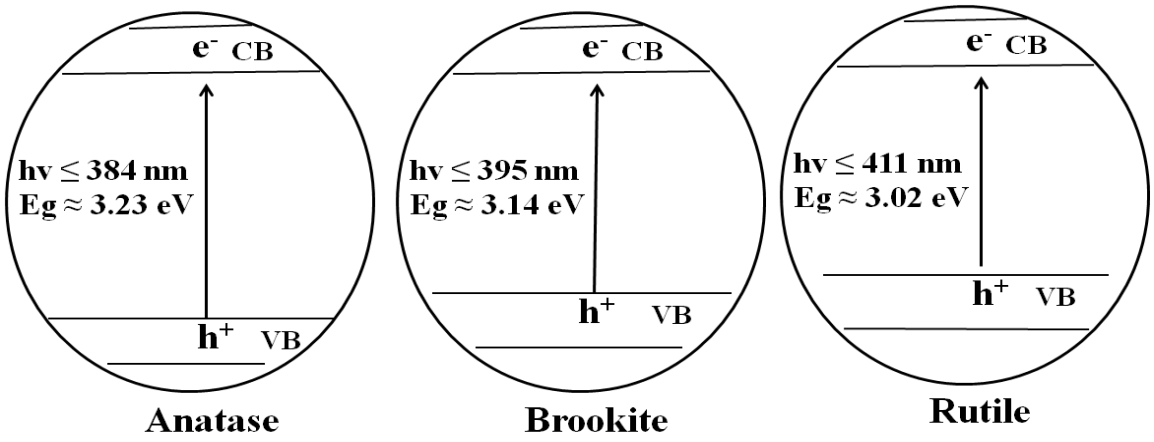

Figure 2. 3 Schematic presentation of wavelength energies required to activate different TiO_2 surfaces.

2.4.3 Catalyst loading

In a heterogeneous regime the photo-catalytic reaction rate is directly proportional to the mass of catalyst present within the system of interest [54]. Initially photo-catalytic degradation increases with an increase in the amount of catalyst, but then decreases at higher mass values of catalyst. This is because of light scattering and screening effects. At higher catalyst loadings the tendency of particles to agglomerate is increased, thus a decrease in the catalyst surface area that is exposed to light absorption. Excess particle concentration compromises light penetration into solution. Therefore optimum catalyst loading must be determined to avoid wasting catalyst and inhibition of photon absorption [54, 11].

2.4.4 pH

The pH of a solution plays a crucial role in photo-catalytic degradation of organic contaminants, since organics exhibit different properties in waters. Organic pollutants exhibit in H_2O varying properties which include hydrophobicity, speciation behaviour and solubility in water. The pH of a solution becomes significant in photo-catalytic degradation as it dictates the surface charge of catalyst, agglomeration size of catalyst particles, and the electrostatic interactions between the catalysts surface and the pollutant of interest [52].

The point of zero charge (PZC) has been employed to study the effect of pH on TiO_2 catalyst during photo-catalytic reactions. PZC refers to the pH at which a surface has a net neutral charge. Under acidic (pH < PZC) or alkaline (pH > PZC) condition the surface of titania can be protonated or deprotonated respectively according to the following reactions [54, 1, 11]:

$$TiOH + H^+ \rightarrow TiOH_2^+ \quad (2.6)$$

$$TiOH + OH^- \rightarrow TiO^- + H_2O \quad (2.7)$$

In acidic medium (pH < 6.9) the titania surface will remain positively charged and negatively charged in alkaline medium (pH > 6.9). Depending on the pollutant charge, adsorption Coulombic attraction or repulsion can be favoured. For instance, if the pH of solution is lower than the PZC of catalyst, the surface of the catalyst tends to be positively charged and can cause enhanced absorption of a pollutant (e.g. 4-chlrorphenol) onto the surface [53, 58].

2.4.5 Nature and concentration of organic pollutants

Photo-catalytic degradation rate is dependent on pollutant concentration and constituent [4, 1]. When similar parameters are maintained with varied pollutant concentration it becomes necessary to vary the irradiation period in order to archive mineralization. Very high concentrations of pollutants are said to saturate the TiO_2 surface and deactivate the catalyst surface by reducing photon efficiency or producing species that can poisen the surface. As the concentration of pollutant increases, more pollutant molecules get absorbed on the catalyst surface, and if the pollutant absorbs in the UV-Vis range that corresponds to the photo-catalysts band-gap energy, decrease the penetration of light onto the surface. Since the intensity of light and irradiation periods are constant, photo-catalytic activity tends to decrease at higher pollutant concentration [59]. Additionally, highly concentrated pollutants can produce intermediates which may adsorb on the catalyst surface and cause catalyst deactivation as they may diffuse slowly from the catalyst surface [11]. The best degradation condition is highly dependent on the kind of pollutant [59].

The corresponding nature and substituent on the target pollutant also influences the degradation efficiency under certain concentrations. For instance, pollutants with electron withdrawing groups are most susceptible to direct oxidation than those with electron donating groups [11, 4, 60].

2.5 Challenges of TiO_2 Nanoparticles in Heterogeneous Photo-catalytic Oxidation

TiO_2 sold as Degussa P25 catalyst is employed as a commercial catalyst throughout the world for various applications including photo-catalytic oxidation, though its efficiency is limited to certain extents. TiO_2 limitations lie in its low quantum efficiency and the wide band gap. The low quantum efficiency limitation is that the catalyst requires to be activated with light having wavelengths < 380 nm, which is a comparatively small portion of the electromagnetic spectrum that reaches the earth's surface. While the wide band gap leads to fast recombination rates of the electron-hole pairs. Most studies indicate that fast electron-hole recombination rates are the key drawbacks to photo-catalytic efficiency of titania catalyst systems [2, 17, 12, 61, 62].

Various aspects relating to a reduced performance have been related to the physical and chemical properties of the materials as well as morphological traits and parameters involved during the photo-catalytic tests. Surface properties play a crucial role in photo-activity of a catalyst since the reaction proceeds through surface interaction between the catalyst and the substrate [21]. Literature shows that improvement of photo-catalytic activity can be achieved by using porous TiO_2 nano-materials [63, 29, 64]; doping with heteroatoms [65-67] or noble metals [68, 69]; introducing organic or inorganic supports that immobilize and improve the dispersion of the catalyst [70-72]; modifying with transition metal ions [73-75]; coupling with small band gap semiconductors [75-77]; and modifying the morphology of the catalyst [78-80, 21].

Kako et al. [81] found that undoped TiO_2 in the rutile crystal phase was sensitive to visible light and had higher photo-catalytic activity when the surface area was increased. They attributed their findings to be a result of the Ti^{3+} located at the interstitial sites of their material.

Kumareshan et al. [73] reported that doping TiO_2 with the metal ions Zr^{4+}, La^{3+} and Ce^{3+}, allowed for incorporation of metals into the lattice and some metal binding to the surface of TiO_2. While, transition metal oxides, such as , were reported by Palanisamy et al. [82] to incorporate the metal ions into the interstitial sites in the photo-catalyst. In both cases, the lattice incorporation and interstitial substitution resulted in visible light adsorption by the doped TiO_2 [82, 73, 83, 74]. The morphology of a semiconductor photo-catalyst seems to play a crucial role in enhancing photo-catalytic activity of TiO_2 for different applications of interest.

Supporting the powder catalyst on other solid supports can enhance the physical and chemical properties of TiO_2 and it allows for catalyst recycling. It is worth mentioning that the use of the powder form is most common (at bench scale) since dispersing the catalyst in the contaminated solution increases the surface area and allows for better recovery after treatment [85, 54]. Studies are being conducted to modify existing or prepare and develop new materials that can be used under sunlight energy and lead to enhanced photo-degradation by overcoming the current limitations posed by TiO_2. Of interest to us are powder samples with high specific surface area, nanosized particles and ordered pores that have been proposed to offer better adsorption of the reactant molecules and to reduce recombination rate.

2.6 Modification/Support of TiO_2 with Mesoporous Nano-materials

2.6.1 Mesoporous Material Classes and Synthetic Approaches

Porous materials are classified into different groups according to the pore size. IUPAC classifies the pores as macroporous (>50 nm), microporous (<2 nm), and mesoporous (2 – 50 nm) [86]. The first reported ordered mesoporous material was MCM-41, which was a mesoporous form of silica, with hexagonal molecular sieves [87]. Since the discovery of MCM-41, ordered mesoporous materials have stirred a lot of interest because of their desirable traits, such as high surface area, tunable pore geometries, narrow pore size distributions and large pore volumes [87].

The two common silica based synthetic approaches for the formation of mesoporous material are presented in **Figure 2.4**.

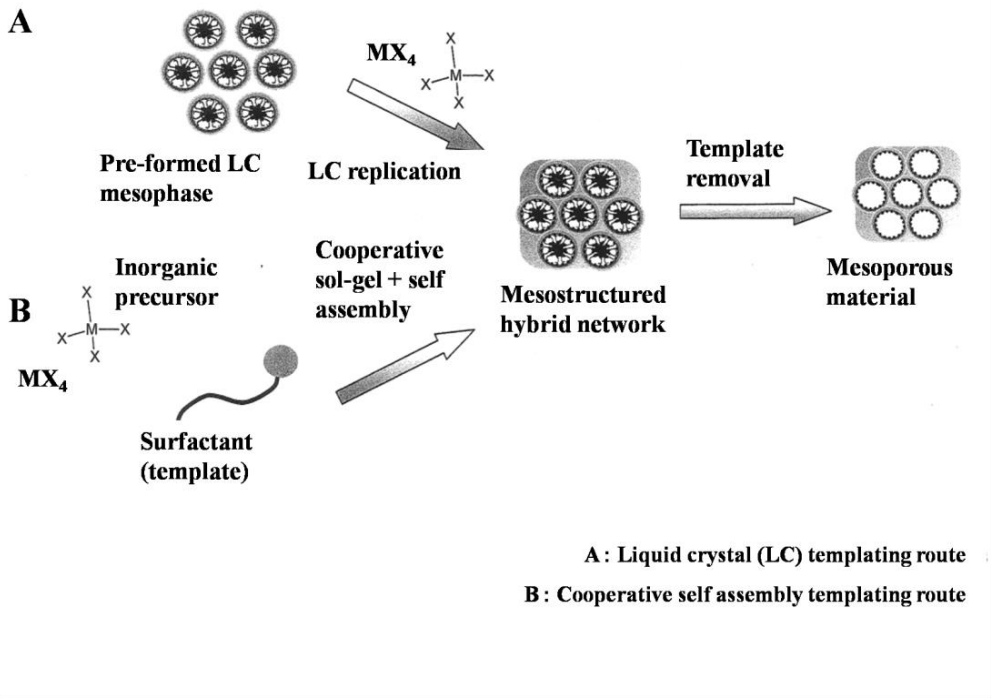

Figure 2. 4 Schematic presentation of mesoporous material formation from use of surfactants and precursors in the sol-gel chemistry [88].

Approach A describes the use of preformed materials with the desired structure, or supramolecular templates (micelle assemblies or liquid crystal forming templates) that have formed and stabilised in the solution. This is followed by the addition of the precursor (e.g. tetraethylorthosilicate) into the reaction medium, and finally the synchronized formation of the meso-structured hybrid network that deposits around the template. Replication of the inorganic species occurs at the accessible sites built by supramolecular or self-assembled templates. The replication process creates a meso-structured material. Approach B depicts an in-situ cooperative assembly of the surfactant and the precursor to yield organized meso-structured hybrid networks which upon removal of surfactant will result in the mesoporous material.Of utmost importance in route B is the delicate balance between two competitive processes, the phase organization/separation of the template and the inorganic polymerization phase [88].

Once the mesostructured hybrid is formed, the template can be removed through thermal or chemical treatment, including other methods that were presented in **Table 2.1**.

Applications of ordered mesoporous materials are well established in the electronics [89], medicinal [90], biotechnology [91], chemical, environmental [92], optics [93] and energy fields [94]. Their pore geometry, chemical inertness, and high surface area allow them to be used as supports, electrode materials, catalysts, and adsorbents depending on their properties [84, 95, 96, 29, 21, 63, 97-100]. Different synthesis approaches have yielded mesoporous materials with different properties. Zhao et al. [101] synthesized mesoporous silica dioxide (SiO_2), denoted SBA-15 for the acronym Santa Barbara Acids, with pore diameters ranging from 5 – 30 nm. Coleman and co-workers reported on the synthesis of SBA-15 from use of micellar solutions and liquid crystal phase and found that the order of the material was dependent on the surfactant concentration when synthesizing from micellar solutions. Whereas synthesis from liquid crystals replicated the morphology of the crystal phase [102]. The key differences between the first reported mesoporous silica MCM41, and these latter materials SBA-15, were the tunable and large pore sizes and thicker walls with SBA-15. As a result, SBA-15 has a much greater thermal stability than MCM41, and can have a larger more accessible surface area than MCM41. Since the physical-chemical properties of SBA-15 can be tailored via tuning the pore size and geometry, various efforts have been made into tuning the structure and pore size of these materials because of their properties which can be designed to suit various applications. They exist in different sizes and geometries, with microscopic morphologies such as spheres, helicoids, tops, fibers and thin films [63, 102, 103, 28, 101, 104].

Silica based materials are of great interest because of their flexibility and ease of controlling their physical and chemical properties. However, amongst ordered mesoporous materials in general, there are non-silicate materials with similar interesting physico-chemical properties and potential applications in various areas such as catalysis, photo-catalysis, sensors, separation techniques, smart coating, biomedical applications, electrochemical conversion systems, and other areas within nanotechnology [105]. Such materials include metal oxides, oxophospates, siliconitrides, polymers and carbon. However studies on kinetics and mechanisms of most ordered mesoporous materials are done on silica.

Additionally, synthesis methods of ordered mesoporous materials are based on the initial templates and sol-gel methods used for silica based materials. Similarly, composites of ordered mesoporous materials are often prepared from silica based methods.

2.6.2 TiO_2/SBA-15 Nano-composites

The use of TiO_2 supported on SBA-15 shows enhanced properties for photo-catalytic studies. Acosta et al. [106] prepared TiO_2/SBA-15 composites containing 7 – 31% TiO_2 through sol-gel chemistry. The composite properties where evaluated on the photo-degradation of methylene blue (MB) and the study found that composites with 31% TiO_2 were more photo-catalytically efficient than unsupported TiO_2 and commercial TiO_2. The enhanced activity of the composite was attributed to the highly crystalline TiO_2 with small crystallite sizes. Similarly, the study by Lachheb et al. [107] found that increasing the content of TiO_2 on SBA-15 increased the photo-activity of the composite in decomposing MB.

Busuioc et al. [70] used the acid catalyzed sol-gel method to deposit TiO_2 nano-particles into the pores of SBA-15, the composite was employed to degrade rhodamine yellow (R6G) in aqueous solution. The study found that composites with less TiO_2 loading had better activity. Naik et al. [69] reported on a composite of TiO_2-SBA-15 using a wet impregnation method, they noticed an enhanced photo-catalytic activity when degrading methyl orange in visible light even at low loadings. TiO_2/SiO_2 composites have also been immobilized on glass substrate through the sol-gel method, the composite material showed good degradation of methyl orange [108]. The study of Shindo et al. [109] showed that depositing titanium nano-particles inside the pores of SBA-15 improved the photo-activity of the composites more than depositing the particles on the surface of SBA-15. Efforts have been made by several authors in order to tune the physical and chemical properties of titana-silica based composites during synthesis to make them suitable for various applications [110-113]. Silica supported titania (TiO_2-SiO_2) or titania-silica mixed oxides fall into the class of most studied catalyst for selective oxidation reactions [114, 110] and they have been employed to understand the surface and nature of porous hybrids from a water thermo-desorption perspective [115]. The growing interest on these composites has also led to doping the TiO_2/SBA-15 composite with several metals such as Cu, Pt and Ag [69, 116, 117].

2.6.3 Multi-walled Carbon Nanotubes (MWCNT)

Carbon nanotubes (CNT) were first reported in 1991 by Iijima [118], the tubes consisted of multi layers of concentric graphite shells, and where named multi-walled carbon nanotubes (MWCNT). Since then, synthesis, characterization, properties modification and application of CNTs have received much attention. Single-walled carbon nanotubes (SWCNT) were reported by Iijima and co-workers two years after the discovery of MWCNT [119]. SWCNTs are made up of single layers of graphene sheets rolled into a cylindrical tube. CNTs also exist as double walled carbon nanotubes (DWCNT), which have been shown to be very important for theoretical and experimental researchers [120, 121]. **Figure 2.5** depicts the main structures of CNTs, one composed of a single and the other composed of multiple concentric cylinders of graphene.

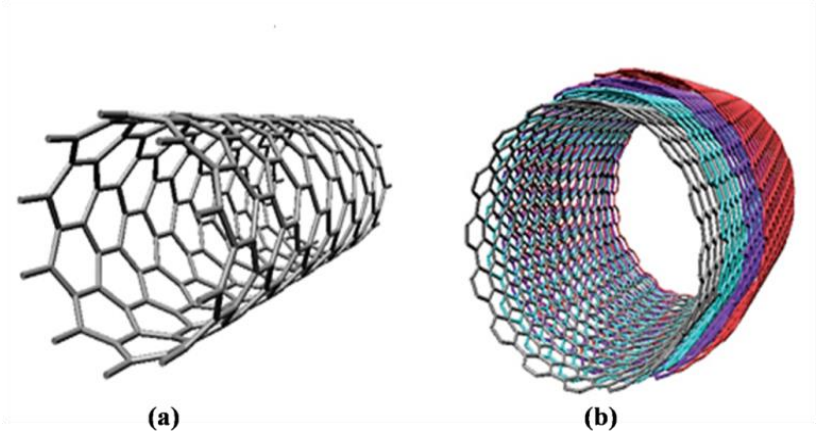

Figure 2. 5 Schematic illustration of single walled carbon nanotubes (a) and multi walled carbon nanotubes (b) [122].

CNTs have a high surface area, high tensile strength and low density [123], and CNTs also have good mechanical, electrical, vibrational and thermal properties [124-128]. Overney et al. [127] showed that MWCNT have a very high structural rigidity and speculated their possible use in composite materials with improved mechanical properties. To date a lot of literature has been reported on the ease of synthesis and advantages of CNT nano-composites. Some of the CNT applications are found in the chemical industry, were they are used as gas adsorbents, templates, catalyst supports, composite reinforcements, chemical sensors, nano-pipes, rechargeable batteries, automotive parts, thin-film electronics and large area coatings [128, 129].

Recent advances on CNTs structures include CNT yarns and sheets which show promising performance in super-capacitors, actuators, and light weight electromagnetic shields [129]. CNTs are of interest in photo-catalysis because of their electronic properties, which are associated with their 1D structure that facilitates the charge separation and transfer process [23]. The scope of this study includes the use of MWCNTs as they are an appropriate substrate for metal oxide coatings. Their surface defects and atomic vacancies [130, 131] enable modification of their surface, especially once they are functionalized [132].

Functionalizing MWCNTs is important since the surface is highly resistant to chemical modification and they are not be soluble in a majority of common solvents [126, 128, 123]. Surface groups on the outside walls of CNTs serve as initiators for further chemistry on the tubes [124]. A variety of oxidizing agents for MWCNTs exist as illustrated by Satishkumar et al. [133] who functionalized MWCNTs structures with concentrated nitric acid, concentrated sulphuric acid, aqua regia, HF-BF_3, aqueous OsO_4, and $KMnO_4$. Amongst the available oxidizing agents that have been reported, nitric acid treatment is the most preferred because it does not cause a lot of damage to the CNT structure, in contrast to nitric acid/sulphuric acid treatment [134, 131]. Nitric acid treatment introduces surface groups such as carboxylic groups, carbonyl and alcohol to the outer walls and possibly inner walls of the CNTs, and the tube ends also get modified and can result in tube opening [126]. Another advantage with nitric acid treatment is it does not introduce secondary impurities [135]. Acid treatment does purify CNT samples and allows for scientists to improve, explore various applications and also find new applications for CNTs since the surface is enabled for further chemistry [124, 135, 136]. The great physical-chemical properties of MWCNTs make them stand out as good supports for various catalysts, and more notably TiO_2.

2.6.4 TiO_2/MWCNTs Nano-composite

The use of MWCNTs coated with TiO_2 nano-particles to enhance photo-catalytic activity is well established in literature. Chen et al. [137] coated MWCNTs with TiO_2 nano-particles using the sol-gel method and annealed the composite with an infrared lamp.

They reported that the composite was much improved (homogeneity) by the polar group interaction from both materials. TiO_2 sensitivity was enhanced by the presence of MWCNTs of lower content than those of high content. Yoneyama and Torimoto [138] conducted a study on the significance of an adsorbent as support for TiO_2 and they showed that the support creates a surface that is highly concentrated with pollutants (by adsorption) near the TiO_2 surface and allows for faster degradation of more pollutants. The same mechanism can be said to be true for MWCNTs used as supports for the photo-catalyst. The authors also stated that the activity of the adsorbent performance vary according to the pollutants to be degraded.

Da Dalt et al. [18] prepared TiO_2-MWCNT composite via sol-gel and thermally treated the materials at different temperature. They used the composite to degrade methyl orange and were able to confirm heterojunctions in the composite. Fu et al. [71] also prepared TiO_2-MWCNT composites and degraded methyl orange. The enhanced photo-catalytic activity of the catalyst was attributed to the increased ability of tubes to be dispersed in ethanol. Furthermore, the authors confirmed the presence of heterojunctions (interface between two dissimilar crystalline materials) in the composite, a view supporting the study of Da Dalt et al. [18]. These studies mean that sol gel method yields good TiO_2-CNT interactions which enhances their catalytic properties.

Gao et al. [139] reported on individually wrapped MWCNTs with uniform nano sized TiO_2. The sol-gel method was employed for synthesis and the composite could photo-electro catalytically enhance the decomposition of methylene blue in aqueous solution. Yen et al. [140] discovered that the photo-catalytic activity of the nano-composite was greatly affected by the morphology and physico-chemical properties possessed. Whereas the properties were influenced by the synthesis technique employed. In particular (to the study of Yen et al.) the samples prepared by the sol-gel method were more efficient in the degradation of phenol and NO_x than samples prepared by hydrothermal treatment. Jitianu et al. [141] synthesized crystalline TiO_2 of anatase phase using cetylmethylammonium bromide (CTAB), a cationic surfactant, and two separate alkoxide precursors titania tetra-ethoxide and titanium tetra-isopropoxide. They observed that the presence of CTAB slowed down the anatase crystallization rate and resulted in a disorder coating of TiO_2 layer on the nanotubes.

Depending on the kind of precursor used in the sol-gel method, MWCNTs can be coated with either thin film TiO_2 or with TiO_2 nano-particles as observed in Jitianu's report [142].

The use of titanium tetra-ethoxide ($Ti(OEt)_4$) gave continuous thin film while use of titanium tetra-isopropoxide ($Ti(OPr^i)_4$) gave nano-particle coating [141]. Titanium tetra-chloride ($TiCl_4$) in acid was used by Omidavar [132] to coat TiO_2 nano-particle on the modified surface of CNTs. They reported that the coating was due to the formation of a bond between the incomplete surface of TiO_2 and functionalized CNT surface. Sampaio et al. [22] used different TiO_2 sources to prepare TiO_2-CNT composites on a glass substrate using the doctor blade technique. The composite degraded methylene blue effectively and they attributed the results to the creation of an electronic interface interaction that existed in the composite. Hence leading to decreased band gap energy of the composite. Improved photo-catalytic activity can also be attributed to the high dispersion of semiconductor nano-particles on the CNT surface [143].

2.6.5 TiO_2/SBA-15-MWCNTs Nano-composite

Work on the enhancement of TiO_2 properties on mesoporous silica coated MWCNTs composite has not been reported for any study to the best of our knowledge. The TiO_2/SBA-CNT composite will be reported in this work for the first time. The photo-catalytic properties of the composite will be explored on the degradation of selected organic pollutants found in water.

2.7 Photo-catalytic Degradation of Organic Pollutants

Heterogeneous photo-catalysts are effective for the degradation of pollutants in aqueous medium. Recycling waste water as an attempt to meet the increasing demand for potable water has been the central focus for many research groups all over the world. Waste water is not easily recycled because of the various sources of contaminants [2]. Pollutants may exist as organic or inorganic pollutants. With most being organics that are not easily biodegradable, or removed [60, 55, 12]. These pollutants can be found in dams and rivers that are key sources for potable water treatment plants.

Methylene blue (MB) [3,7-bis(dimethylamino)phenothiazi-5-ium chloride] is a cationic thiazine organic dye with a chemical formulae of $C_{16}H_{18}N_3SCl.3H_2O$ (**Figure 2.6a**). MB has dominant absorption peak at approximately 665 nm. It is commonly employed in textile, cosmetic, food, and pharmaceutical industries for use such as dyeing leather, cotton, wood, silk and printing calico [106, 144]. In this thesis, MB will be studied as a model pollutant.

Pesticides are chemicals used as herbicides; insecticides; rodenticides; nematicides; plant growth regulators that can control weeds, pests and diseases in crops; and as a health care option for humans and animals (e.g. removal of ticks). They are categorized according to the pests they control, categories are: herbicides, fungicides, insecticides and bactericides [145].
Pesticides are used to enhance crop/food production and reduce vector borne diseases [146]. However, at certain concentrations and periods of exposure they are highly toxic to humans.

4-Chloro-2-methylphenoxy acetic acid (**Figure 2.6b**) is a herbicide that is used worldwide under the trade name MCPA. It belongs to a large group of commonly employed herbicide, chlorophenoxyacetic acids. MCPA is a herbicide employed to control annual perennial weeds in cereal, grassland and turf. It is absorbed by leaves, roots and stem tissues. It is reported to have a pKa value of 3.07 with a solubility of 273.9 mg L^{-1} at pH 7 in water [147]. MCPA can leach from the soils, and release its free acids, salts and esters as the active ingredients. Although MCPA can be metabolized by bacteria and can be photo-chemically degraded, these do not exclude them from the list of persistent organic pollutants. The United States Environmental Protection Agency (EPA) classifies the herbicide as ground water contaminant with possible mutagenic and carcinogenic properties [148]. Detection of MCPA in surface and ground water has been reported at concentrations below 0.5 and 5.5 µg L^{-1} [149].

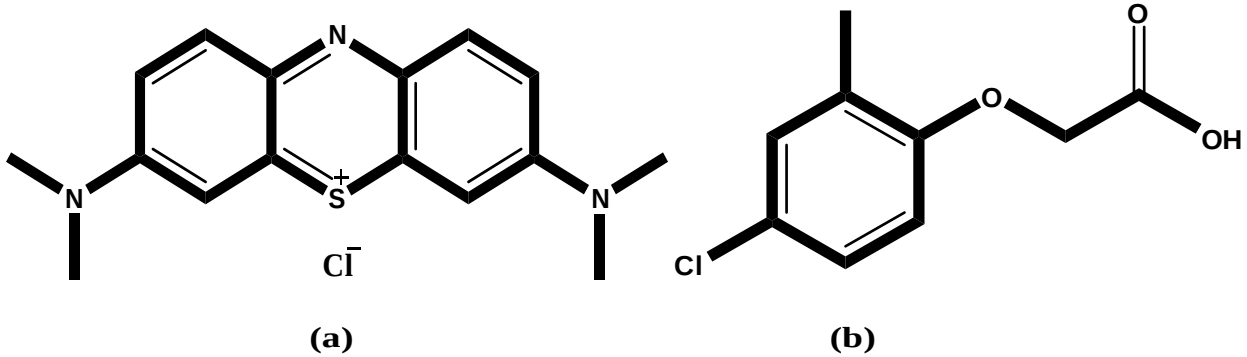

(a) **(b)**

Figure 2. 6 Chemical structure of methylene blue (a) and MCPA (b).

Several studies have been conducted to monitor the transformation of MCPA. Photo-catalytic transformation of MCPA is commonly reported using TiO_2 photo-catalyst. Djebbar et al. [150] proposed a transformation mechanism after irradiating 5 x 10^{-4} M MCPA aqueous solution with 15/5 TLAD fluorescent lamp. The study demonstrated an enhanced photo-degradation at pH greater than 12. The major degradation product was identified as 2-chloro-4-methylphenol, which was reported as less toxic. The same authors demonstrated the dependency of pollutant transformation on pH rather than irradiation wavelengths [151]. Photo-dehalogenation studies of MCPA have also been conducted through UV irradiation using XeBr and KrCl excilamps to produce 2-methylhydroquinone and 2-hydro-3-methyl-5-chlorophenoxyacetic acid respectively as the major products [152]. Sanchis et al. [153] have reported on the use of Fenton and biological oxidation process to degrade MCPA.

MCPA transformation is thought to proceed mainly through reaction of hydroxyl radicals in acidic solution as illustrated by the radiolytic studies of Czajka et al. [154]. Recently Pirozzi and Sannino [155] conducted sorption studies to remove MCPA through use of metal catalysts Al_2O_3 and Fe_2O_3. N and Fe doped TiO_2 was employed to photo-catalytically degrade MCPA at natural pH reported to be approximately 2.8 [156]. The study concluded that doping TiO_2 did not enhance the degradation; rather the molecular structure of the target compound was more influential. To the best of our knowledge, no studies have reported the photo-catalytic transformation of MCPA with carbon nanotubes catalyst composites. Although sorbent and titania structures have been studied separately.

2.8 Summary

The literature review showed that heterogenous photo-catalysis using TiO_2 nano-particles can be used in remediation studies. TiO_2 catalysts can improve the catalysis process and efficiency, through modification of catalyst properties. The sol-gel method have proven to be successfully in preparing materials with enhanced photo-catalytic properties. Anatase TiO_2 composites are preffered over pure anatase titanium for use under visible light irradiation. The composite materials offer superior activity in the visible region of the solar spectrum through reduced band gap energies, smaller crystal sizes, narrow pore size distributions, slow rates of electron – hole recombination, and synergic effects of the different materials. Of the various ways of modifying TiO_2, mesoporous TiO_2 with ordered pores and supporting TiO_2 on high surface area materials appear to be superior over other modification strategies.

2.9 References

1. Rauf, M., Meetani, M. and Hisaindee, S., *An overview on the photocatalytic degradation of azo dyes in the presence of TiO_2 doped with selective transition metals*. Desalination, 2011. **276**(1): p. 13-27.
2. Carp, O., Huisman, C. L. and Reller, A., *Photoinduced reactivity of titanium dioxide.* Progress in Solid State Chemistry, 2004. **32**(1–2): p. 33-177.
3. Gázquez, M. J., Bolívar, J. P., Garcia-Tenorio, R. and Vaca, F., *A Review of the Production Cycle of Titanium Dioxide Pigment.* Materials Sciences and Applications, 2014. **5**(07): p. 441.
4. Khataee, A. and Kasiri, M. B., *Photocatalytic degradation of organic dyes in the presence of nanostructured titanium dioxide: Influence of the chemical structure of dyes*. Journal of Molecular Catalysis A: Chemical, 2010. **328**(1): p. 8-26.
5. Maphango, L., *Overview of south africa's titanium industry and global market review, 2012. Key features between 2002 and 2011, in Department of Mineral Sciences, Republic of South Africa*, 2013.
6. Zhang, W., Zhu, Z. and Cheng, C. Y., *A literature review of titanium metallurgical processes.* Hydrometallurgy, 2011. **108**(3): p. 177-188.
7. Ikeshima, T., Iseki, J. and Naritomi, T., *Recent developments in titanium sponge production.* Titanium--Science and Technology., 1984. **1**: p. 3-14.
8. Hsu, C. K. and Chiang, B. H., *Effects of water, oil, starch, calcium carbonate and titanium dioxide on the colour and texture of threadfin and hairtail surimi gels*. International journal of food science & technology, 2002. **37**(4): p. 387-393.
9. Sahu, K. K., Alex, T. C., Mishra, D. and Agrawal, A., *An overview on the production of pigment grade titania from titania-rich slag.* Waste management & research, 2006. **24**(1): p. 74-79.
10. Hsu, W. P., Yu, R. and Matijević, E., *Paper whiteners: I. Titania coated silica.* Journal of colloid and interface science, 1993. **156**(1): p. 56-65.
11. Chong, M. N., Jin, B., Chow, C. W. K. and Saint, C., *Recent developments in photocatalytic water treatment technology: A review.* Water Research, 2010. **44**(10): p. 2997-3027.

12. Ibhadon, A. O. and Fitzpatrick, P., *Heterogeneous Photocatalysis: Recent Advances and Applications.* Catalysts, 2013. **3**(1): p. 189-218.
13. Qi, K., Daoud, W. A., Xin, J. H., Mak, C., Tang, W. and Cheung, W., *Self-cleaning cotton.* Journal of materials chemistry, 2006. **16**(47): p. 4567-4574.
14. Elgh, B. and Palmqvist, A. E., *Controlling anatase and rutile polymorph selectivity during low-temperature synthesis of mesoporous TiO_2 films*. Journal of Materials Chemistry A, 2014.
15. Al-Rasheed, R. A. *Water treatment by heterogeneous photocatalysis an overview. in 4th SWCC Acquired Experience Symposium, Jeddah*, 2005.
16. Bell, N., *On the design and synthesis of titanium dioxide–graphene nanocomposites for enhanced photovoltaic and photocatalytic performance*. 2011.
17. Chatterjee, D. and Dasgupta, S., *Visible light induced photocatalytic degradation of organic pollutants.* Journal of Photochemistry and Photobiology C: Photochemistry Reviews, 2005. **6**(2–3): p. 186-205.
18. Da Dalt, S., Alves, A. K. and Bergmann, C. P., *Photocatalytic degradation of methyl orange dye in water solutions in the presence of MWCNT/TiO_2 composites*. Materials Research Bulletin, 2013. **48**(5): p. 1845-1850.
19. Fujishima, A., Rao, T. N. and Tryk, D. A., *Titanium dioxide photocatalysis.* Journal of Photochemistry and Photobiology C: Photochemistry Reviews, 2000. **1**(1): p. 1-21.
20. Takeda, H. and Ishitani, O., *Development of efficient photocatalytic systems for CO_2 reduction using mononuclear and multinuclear metal complexes based on mechanistic studies*. Coordination Chemistry Reviews, 2010. **254**(3): p. 346-354.
21. Yu, J., Wang, W., Cheng, B. and Su, B.-L., *Enhancement of photocatalytic activity of mesporous TiO_2 powders by hydrothermal surface fluorination treatment.* The Journal of Physical Chemistry C, 2009. **113**(16): p. 6743-6750.
22. Sampaio, M. J., Silva, C. G., Marques, R., Silva, A. M. and Faria, J. L., *Carbon nanotube–TiO_2 thin films for photocatalytic applications.* Catalysis Today, 2011. **161**(1): p. 91-96.
23. Di Paola, A., García-López, E., Marcì, G. and Palmisano, L., *A survey of photocatalytic materials for environmental remediation.* Journal of hazardous materials, 2012. **211**: p. 3-29.

24. Chena, L., Pangb, X., Yua, G. and Zhanga, J., *In-situ coating of MWNTs with sol-gel TiO_2 nanoparticles.* Adv Mater Lett, 2010. **1**(1): p. 75-8.
25. Ward, D. A. and Ko, E. I., *Preparing catalytic materials by the sol-gel method.* Industrial & engineering chemistry research, 1995. **34**(2): p. 421-433.
26. Zhang, R., Elzatahry, A. A., Al-Deyab, S. S. and Zhao, D., *Mesoporous titania: From synthesis to application.* Nano Today, 2012. **7**(4): p. 344-366.
27. Ciriminna, R., Fidalgo, A., Pandarus, V., Béland, F. o., Ilharco, L. M. and Pagliaro, M., *The Sol–Gel Route to Advanced Silica-Based Materials and Recent Applications.* Chemical reviews, 2013. **113**(8): p. 6592-6620.
28. Meynen, V., Cool, P. and Vansant, E., *Verified syntheses of mesoporous materials.* Microporous and Mesoporous Materials, 2009. **125**(3): p. 170-223.
29. Taguchi, A. and Schüth, F., *Ordered mesoporous materials in catalysis.* Microporous and Mesoporous Materials, 2005. **77**(1): p. 1-45.
30. Zaiku, X., Zhicheng, L., Yangdong, W., Qihua, Y., Longya, X. and Ding, W., *An Overview of Recent Development in Composite Catalysts from Porous Materials for Various Reactions and Processes.* International Journal of Molecular Sciences, 2010. **11**(5): p. 2152-2187.
31. Tanaka, S. and Nishiyama, N., *Morphology Control of Ordered Mesoporous Carbon Using Organic-Templating Approach - From Analysis and Modeling to Technology Applications*, 2011. Prof. Angelo Carpi (Ed.), ISBN: 978-953-307-268-52011.
32. Tao, Y., Endo, M., Inagaki, M. and Kaneko, K., *Recent progress in the synthesis and applications of nanoporous carbon films.* Journal of Materials Chemistry, 2011. **21**(2): p. 313-323.
33. Vautier-Giongo, C. and Pastore, H. O., *Micellization of CTAB in the presence of silicate anions and the exchange between bromide and silicate at the micelle surface: A step to understand the formation of mesoporous molecular sieves at extremely low surfactant and silicate concentrations.* Journal of Colloid and Interface Science, 2006. **299**(2): p. 874-882.
34. Debecker, D. P., Hulea, V. and Mutin, P. H., *Mesoporous mixed oxide catalysts via non-hydrolytic sol–gel: a review.* Applied Catalysis A: General, 2013. **451**: p. 192-206.

35. Antonelli, D. M. and Ying, J. Y., *Synthesis of hexagonally packed mesoporous TiO_2 by a modified sol–gel method.* Angewandte Chemie International Edition in English, 1995. **34**(18): p. 2014-2017.
36. Calleja, G., Serrano, D. P., Sanz, R., Pizarro, P. and García, A., *Study on the synthesis of high-surface-area mesoporous TiO_2 in the presence of nonionic surfactants.* Industrial & engineering chemistry research, 2004. **43**(10): p. 2485-2492.
37. Zheng, J.-Y., Pang, J.-B., Qiu, K.-Y. and Wei, Y., *Synthesis and characterization of mesoporous titania and silica–titania materials by urea templated sol–gel reactions.* Microporous and mesoporous materials, 2001. **49**(1): p. 189-195.
38. Bian, Y., Wang, X. and Hu, Z., *Synthesis of mesoporous titania thin films by a simple route at low-temperature via plasma treatment.* Journal of Materials Science, 2013. **48**(11): p. 4088-4096.
39. Koshitani, N., Sakulkhaemaruethai, S., Suzuki, Y. and Yoshikawa, S., *Preparation of mesoporous titania nanocrystals using alkylamine surfactant templates.* Ceramics international, 2006. **32**(7): p. 819-824.
40. Peres-Durand, S., Rouviere, J. and Guizard, C., *Sol-gel processing of titania using reverse micellar systems as reaction media.* Colloids and Surfaces A: Physicochemical and Engineering Aspects, 1995. **98**(3): p. 251-270.
41. Antonelli, D., *Synthesis of phosphorus-free mesoporous titania via templating with amine surfactants*. Microporous and Mesoporous Materials, 1999. **30**(2): p. 315-319.
42. Kim, H.-J., Jeon, J.-D. and Kwak, S.-Y., *Highly dispersed mesoporous TiO_2 spheres via acid treatment and its application for dye-sensitized solar cells*. Powder Technology, 2013. **243**: p. 130-138.
43. Luo, H., Wang, C. and Yan, Y., *Synthesis of mesostructured titania with controlled crystalline framework.* Chemistry of materials, 2003. **15**(20): p. 3841-3846.
44. Zeng, J., *CTAB-assisted fabrication of TiO_2 with improved photocatalytic performance*. Materials Letters, 2013. **100**: p. 195-197.
45. Song, C., Wang, D., Xu, Y. and Hu, Z., *Preparation of Ag-TiO_2 hollow structures with enhanced photocatalytic activity.* Materials Letters, 2011. **65**(5): p. 908-910.

46. Feng, D., Luo, W., Zhang, J., Xu, M., Zhang, R., Wu, H., Lv, Y., Asiri, A. M., Khan, S. B. and Rahman, M. M., *Multi-layered mesoporous TiO_2 thin films with large pores and highly crystalline frameworks for efficient photoelectrochemical conversion*. Journal of Materials Chemistry A, 2013. **1**(5): p. 1591-1599.
47. Joo, J. B., Dahl, M., Li, N., Zaera, F. and Yin, Y., *Tailored synthesis of mesoporous TiO_2 hollow nanostructures for catalytic applications.* Energy Environ. Sci., 2013. **6**(7): p. 2082-2092.
48. Lagopati, N., Kitsiou, P. V., Kontos, A. I., Venieratos, P., Kotsopoulou, E., Kontos, A. G., Dionysiou, D. D., Pispas, S., Tsilibary, E. C. and Falaras, P., *Photo-induced treatment of breast epithelial cancer cells using nanostructured titanium dioxide solution.* Journal of Photochemistry and Photobiology A: Chemistry, 2010. **214**(2–3): p. 215-223.
49. Abidi, N., Cabrales, L. and Hequet, E., *Functionalization of a cotton fabric surface with titania nanosols: applications for self-cleaning and UV-protection properties*. American Chemical Society Applied Materials and Interfaces, 2009. **1**(10): p. 2141-2146.
50. Tiano, L., Armeni, T., Venditti, E., Barucca, G., Mincarelli, L. and Damiani, E., *Modified TiO_2 particles differentially affect human skin fibroblasts exposed to UVA light.* Free Radical Biology and Medicine, 2010. **49**(3): p. 408-415.
51. Ollis, D. F., *Photocatalytic purification and remediation of contaminated air and water.* Comptes Rendus de l'Académie des Sciences-Series IIC-Chemistry, 2000. **3**(6): p. 405-411.
52. Ahmed, S., Rasul, M. G., Martens, W. N., Brown, R. and Hashib, M. A., *Heterogeneous photocatalytic degradation of phenols in wastewater: A review on current status and developments.* Desalination, 2010. **261**(1–2): p. 3-18.
53. Ameta, R., Benjamin, S., Ameta, A. and Ameta, S. C., *Photocatalytic degradation of organic pollutants: A review*, 2013. p. 247-272.
54. Gaya, U. I. and Abdullah, A. H., *Heterogeneous photocatalytic degradation of organic contaminants over titanium dioxide: A review of fundamentals, progress and problems.* Journal of Photochemistry and Photobiology C: Photochemistry Reviews, 2008. **9**(1): p. 1-12.

55. Herrmann, J. M., *Heterogeneous photocatalysis: state of the art and present applications* In honor of Pr. R.L. Burwell Jr. (1912–2003), Former Head of Ipatieff Laboratories, Northwestern University, Evanston (Ill). Topics in Catalysis, 2005. **34**(1-4): p. 49-65.
56. Ahmed, S., Rasul, M. G., Brown, R. and Hashib, M. A., *Influence of parameters on the heterogeneous photocatalytic degradation of pesticides and phenolic contaminants in wastewater: A short review*. Journal of Environmental Management, 2011. **92**(3): p. 311-330.
57. Kaneco, S., Rahman, M. A., Suzuki, T., Katsumata, H. and Ohta, K., *Optimization of solar photocatalytic degradation conditions of bisphenol A in water using titanium dioxide.* Journal of photochemistry and photobiology A: Chemistry, 2004. **163**(3): p. 419-424.
58. Irmak, S., Kusvuran, E. and Erbatur, O., *Degradation of 4-chloro-2-methylphenol in aqueous solution by UV irradiation in the presence of titanium dioxide*. Applied Catalysis B: Environmental, 2004. **54**(2): p. 85-91.
59. Saquib, M. and Muneer, M., *Titanium dioxide mediated photocatalyzed degradation of a textile dye derivative, acid orange 8, in aqueous suspensions.* Desalination, 2003. **155**(3): p. 255-263.
60. Atul, V. W., Gaikwad, G. S., Dhonde, M. G., Khaty, N. T. and Thakare, S. R., *Removal of Organic Pollutant from Water by Heterogenous Photocatalysis: A Review*. Research Journal of Chemistry and Environment, 2013. **17**(1): p. 84-94.
61. Kuwahara, Y. and Yamashita, H., *Efficient photocatalytic degradation of organics diluted in water and air using TiO_2 designed with zeolites and mesoporous silica materials*. Journal of Materials Chemistry, 2011. **21**(8): p. 2407-2416.
62. Minero, C. and Vione, D., *A quantitative evalution of the photocatalytic performance of TiO_2 slurries.* Applied Catalysis B: Environmental, 2006. **67**(3–4): p. 257-269.
63. Ariga, K., Vinu, A., Yamauchi, Y., Ji, Q. and Hill, J. P., *Nanoarchitectonics for mesoporous materials.* Bulletin of the Chemical Society of Japan, 2012. **85**(1): p. 1-32.
64. Deng, Y., Wei, J., Sun, Z. and Zhao, D., *Large-pore ordered mesoporous materials templated from non-Pluronic amphiphilic block copolymers.* Chemical Society Reviews, 2013.

65. Pany, S., Parida, K. M. and Naik, B., *Facile fabrication of mesoporosity driven N-TiO_2@CS nanocomposites with enhanced visible light photocatalytic activity*. RSC Advances, 2013. **3**(15): p. 4976-4984.
66. Raja, P. K., Chokkalingam, A., Priya, S. V., Balasubramanian, V. V., Benziger, M. R., Aldeyab, S. S., Jayavel, R., Ariga, K. and Vinu, A., *Highly Basic CaO Nanoparticles in Mesoporous Carbon Materials and Their Excellent Catalytic Activity.* Journal of Nanoscience and Nanotechnology, 2012. **12**(6): p. 4613-4620.
67. Shi, Z., Liu, F. and Yao, S., *Preparation and photocatalytic activity of B, Y co-doped nanosized TiO_2 catalyst.* Journal of Rare Earths, 2010. **28**(5): p. 737-741.
68. Subramanian, V., Wolf, E. E. and Kamat, P. V., *Influence of metal/metal ion concentration on the photocatalytic activity of TiO_2-Au composite nanoparticles*. Langmuir, 2003. **19**(2): p. 469-474.
69. Naik, B., Manoratne, C. H., Chandrashekhar, A., Iyer, A., Prasad, V. S. and Ghosh, N. N., *Preparation of TiO_2, Ag-doped TiO_2 nanoparticle and TiO_2-SBA-15 nanocomposites using simple aqueous solution-based chemical method and study of their photocatalytical activity.* Journal of Experimental Nanoscience, 2013. **8**(4): p. 462-479.
70. Busuioc, A. M., Meynen, V., Beyers, E., Mertens, M., Cool, P., Bilba, N. and Vansant, E. F., *Structural features and photocatalytic behaviour of titania deposited within the pores of SBA-15.* Applied Catalysis A: General, 2006. **312**(0): p. 153-164.
71. Fu, X., Yang, H., He, K., Zhang, Y. and Wu, J., *Enhanced photocatalytic activity of nano titanium dioxide coated on ethanol-soluble carbon nanotubes.* Materials Research Bulletin, 2013. **48**(2): p. 487-494.
72. Singh, S., Mahalingam, H. and Singh, P. K., *Polymer-supported titanium dioxide photocatalysts for environmental remediation: A review.* Applied Catalysis A: General, 2013. **462-463**: p. 178-195.
73. Kumaresan, L., Prabhu, A., Palanichamy, M., Arumugam, E. and Murugesan, V., *Synthesis and characterization of Zr^{4+}, La^{3+} and Ce^{3+} doped mesoporous TiO_2: Evaluation of their photocatalytic activity.* Journal of Hazardous Materials, 2011. **186**(2–3): p. 1183-1192.
74. Lu, X. C., Jiang, J. C., Sun, K. and Cui, D. D., *Characterization and photocatalytic activity of Zn^{2+}-TiO_2/AC composite photocatalyst.* Applied Surface Science, 2011. **258**(5): p. 1656-1661.

75. Sajjad, A. K. L., Shamaila, S. and Zhang, J. L., *Study of new states in visible light active W, N co-doped TiO_2 photo catalyst.* Materials Research Bulletin, 2012. **47**(11): p. 3083-3089.
76. Subash, B., Krishnakumar, B., Swaminathan, M. and Shanthi, M., *Enhanced photocatalytic performance of WO3 loaded Ag-ZnO for Acid Black 1 degradation by UV-A light.* Journal of Molecular Catalysis a-Chemical, 2013. **366**: p. 54-63.
77. Aguilar, T., Navas, J., Alcántara, R., Fernández-Lorenzo, C., Gallardo, J. J., Blanco, G. and Martín-Calleja, J., *A route for the synthesis of Cu-doped TiO_2 nanoparticles with a very low band gap.* Chemical Physics Letters, 2013. **571**: p. 49-53.
78. Jun, S., Joo, S. H., Ryoo, R., Kruk, M., Jaroniec, M., Liu, Z., Ohsuna, T. and Terasaki, O., *Synthesis of new, nanoporous carbon with hexagonally ordered mesostructure.* Journal of the American Chemical Society, 2000. **122**(43): p. 10712-10713.
79. Pal, M., Serrano, J. G., Santiago, P. and Pal, U., *Size-controlled synthesis of spherical TiO_2 nanoparticles: Morphology, crystallization, and phase transition.* Journal of Physical Chemistry C, 2007. **111**(1): p. 96-102.
80. Tomovska, R., Daniloska, V. and Asua, J. M., *Surface modification of TiO_2 nanoparticles via photocataliticaly induced reaction: Influence of functionality of silane coupling agent*. Applied Surface Science, 2013. **264**(0): p. 670-673.
81. Kako, T., Umezawa, N., Xie, K. and Ye, J. H., *Undoped visible-light-sensitive titania photocatalyst.* Journal of Materials Science, 2013. **48**(1): p. 108-114.
82. Palanisamy, B., Babu, C. M., Sundaravel, B., Anandan, S. and Murugesan, V., *Sol–gel synthesis of mesoporous mixed Fe_2O_3/TiO_2 photocatalyst: Application for degradation of 4-chlorophenol.* Journal of Hazardous Materials, 2013. **252–253**(0): p. 233-242.
83. Litter, M. I. and Navío, J. A., *Photocatalytic properties of iron-doped titania semiconductors.* Journal of Photochemistry and Photobiology A: Chemistry, 1996. **98**(3): p. 171-181.
84. Khan, M. A., Shaheer Akhtar, M. and Yang, O. B., *Synthesis, characterization and application of sol–gel derived mesoporous TiO_2 nanoparticles for dye-sensitized solar cells*. Solar Energy, 2010. **84**(12): p. 2195-2201.

85. Andronic, L., Perniu, D. and Duta, A., *Synergistic effect between TiO_2 sol–gel and Degussa P25 in dye photodegradation.* Journal of Sol-Gel Science and Technology, 2013: p. 1-9.
86. Rouquerol, J., Avnir, D., Fairbridge, C., Everett, D., Haynes, J., Pernicone, N., Ramsay, J., Sing, K. and Unger, K., *Recommendations for the characterization of porous solids (Technical Report).* Pure and Applied Chemistry, 1994. **66**(8): p. 1739-1758.
87. Beck, J., Vartuli, J., Roth, W., Leonowicz, M., Kresge, C., Schmitt, K., Chu, C., Olson, D. and Sheppard, E., *A new family of mesoporous molecular sieves prepared with liquid crystal templates.* Journal of the American Chemical Society, 1992. **114**(27): p. 10834-10843.
88. Soler-Illia, G. J. d. A., Sanchez, C., Lebeau, B. and Patarin, J., *Chemical strategies to design textured materials: from microporous and mesoporous oxides to nanonetworks and hierarchical structures.* Chemical Reviews, 2002. **102**(11): p. 4093-4138.
89. Corma, A., Moliner, M., Díaz-Cabañas, M. J., Serna, P., Femenia, B., Primo, J. and García, H., *Biomimetic synthesis of microporous and mesoporous materials at room temperature and neutral pH, with application in electronics, controlled release of chemicals, and catalysis*. New Journal of Chemistry, 2008. **32**(8): p. 1338-1345.
90. Zhang, M., Wu, Y., Feng, X., He, X., Chen, L. and Zhang, Y., *Fabrication of mesoporous silica-coated CNTs and application in size-selective protein separation.* Journal of Materials Chemistry, 2010. **20**(28): p. 5835-5842.
91. Vallet-Regí, M., Balas, F. and Arcos, D., *Mesoporous materials for drug delivery.* Angewandte Chemie International Edition, 2007. **46**(40): p. 7548-7558.
92. Wang, X., Lin, K. S. K., Chan, J. C. C. and Cheng, S., *Direct synthesis and catalytic applications of ordered large pore aminopropyl-functionalized SBA-15 mesoporous materials*. Journal of Physical Chemistry B, 2005. **109**(5): p. 1763-1769.
93. Xu, H., Pan, Y., Kou, H., Zhu, Y. and Guo, J., *Preparation of transparent ordered mesoporous carbon/silica composites and their optical limiting properties*. Journal of Alloys and Compounds, 2010. **502**(1): p. L6-L9.

94. Zhangxiong, W., Yunxia, Y., Dong, G., Yunpu, Z., Dan, F., Qiang, L., Bo, T., Webley, P. and Dong, Z., *Synthesis of Ordered Mesoporous Carbon Materials with Semi-Graphitized Walls via Direct In-situ Silica-Confined Thermal Decomposition of CH_4 and Their Hydrogen Storage Properties.* Topics in Catalysis, 2009. **52**(1/2): p. 12-26.
95. Pires, J., Borges, S., Carvalho, A. P. and Silva, A. R., *Porous Silicas and Respective Carbon Replicates for Adsorption and Catalysis.* Adsorption Science & Technology, 2010. **28**(8/9): p. 717-726.
96. Su, F., Li, X., Lv, L. and Zhao, X. S., *Ordered mesoporous carbon particles covered with carbon nanotubes.* Carbon, 2006. **44**(4): p. 801-803.
97. Bordoloi, A., Mathew, N. T., Lefebvre, F. and Halligudi, S. B., *Inorganic–organic hybrid materials based on functionalized silica and carbon: A comprehensive understanding toward the structural property and catalytic activity difference over mesoporous silica and carbon supports.* Microporous and Mesoporous Materials, 2008. **115**(3): p. 345-355.
98. Kim, S.-S. and Pinnavaia, T. J., *A low cost route to hexagonal mesostructured carbon molecular sieves.* Chemical Communications, 2001. **0**(23): p. 2418-2419.
99. Wang, D.-w., Li, F., Liu, M. and Cheng, H.-m., *Improved capacitance of SBA-15 templated mesoporous carbons after modification with nitric acid oxidation*. New Carbon Materials, 2007. **22**(4): p. 307-314.
100. Lysenko, N., Shvets, A., Yaremov, P. and Il'in, V., *Effect of the conditions of the matrix carbonization of sucrose on the structure and adsorption properties of mesoporous carbon materials.* Theoretical & Experimental Chemistry, 2008. **44**(6): p. 374-379.
101. Zhao, D., Feng, J., Huo, Q., Melosh, N., Fredrickson, G. H., Chmelka, B. F. and Stucky, G. D., *Triblock copolymer syntheses of mesoporous silica with periodic 50 to 300 angstrom pores.* science, 1998. **279**(5350): p. 548-552.
102. Coleman, N. R. B. and Attard, G. S., *Ordered mesoporous silicas prepared from both micellar solutions and liquid crystal phases.* Microporous and Mesoporous Materials, 2001. **44-45**: p. 73-80.
103. Lee, J., Kim, J. and Hyeon, T., *Recent progress in the synthesis of porous carbon materials.* Advanced Materials, 2006. **18**(16): p. 2073-2094.

104. Tanaka, S., Doi, A., Nakatani, N., Katayama, Y. and Miyake, Y., *Synthesis of ordered mesoporous carbon films, powders, and fibers by direct triblock-copolymer-templating method using an ethanol/water system.* Carbon, 2009. **47**(11): p. 2688-2698.
105. Boettcher, S. W., Fan, J., Tsung, C.-K., Shi, Q. and Stucky, G. D., *Harnessing the sol–gel process for the assembly of non-silicate mesostructured oxide materials.* Accounts of chemical research, 2007. **40**(9): p. 784-792.
106. Acosta-Silva, Y. J., Nava, R., Hernández-Morales, V., Macías-Sánchez, S. A., Gómez-Herrera, M. L. and Pawelec, B., *Methylene blue photodegradation over titania-decorated SBA-15.* Applied Catalysis B: Environmental, 2011. **110**: p. 108-117.
107. Lachheb, H., Ahmed, O., Houas, A. and Nogier, J. P., *Photocatalytic activity of TiO_2-SBA-15 under UV and visible light.* Journal of Photochemistry and Photobiology A: Chemistry, 2011. **226**(1): p. 1-8.
108. Rahmani, E., Ahmadpour, A. and Zebarjad, M., *Enhancing the photocatalytic activity of TiO_2 nanocrystalline thin film by doping with SiO_2.* Chemical Engineering Journal, 2011. **174**(2-3): p. 709-713.
109. Shindo, T., Koizumi, N., Hatakeyama, K. and Ikeuchi, T., *Post-synthesis of TiO_2 dispersed inside the pore channels of SBA-15 and its photocatalytic activity for the degradation of methylene blue.* International Journal of the Society of Material Engineering for Resources, 2011. **18**(1): p. 11-17.
110. Yang, H., Liu, Z., Gao, H. and Xie, Z., *Synthesis and characterization of hierarchical titania-silica monolith.* Catalysis Today, 2013. **216**: p. 90-94.
111. Wang, X. J., Li, F. T., Hao, Y. J., Liu, S. J. and Yang, M. L., *TiO_2/SBA-15 composites prepared using H_2TiO_3 by hydrothermal method and its photocatalytic activity.* Materials Letters, 2013. **99**: p. 38-41.
112. Son, S., Hwang, S. H., Kim, C., Yun, J. Y. and Jang, J., *Designed synthesis of SiO_2/TiO_2 core/shell structure as light scattering material for highly efficient dye-sensitized solar cells*. ACS applied materials & interfaces, 2013.

113. Mazinani, B., Beitollahi, A., Masrom, A. K., Yahya, N., Choong, T. S. Y., Ibrahim, S. M. and Javadpour, J., *Characterization and evaluation of the photocatalytic properties of wormhole-like mesoporous silica incorporating TiO_2, prepared using different hydrothermal and calcination temperatures*. Research on Chemical Intermediates, 2012. **38**(8): p. 1733-1742.
114. Lee, S. L., Nur, H., Koh, P. W., Ekhsan, J. M. and Wei, S. C., *Synthesis and characterization of acid modified silica-titania aerogel as oxidative-acidic bifunctional catalyst.* International Journal of Applied Physics and Mathematics, 2011. **1**(1): p. 43-47.
115. Skubiszewska-Zięba, J., Charmas, B., Leboda, R., Tertykh, V. A. and Yanishpolskii, V. V., *Complex investigations of structural and thermal properties of silica-titania adsorbents.* Journal of Thermal Analysis and Calorimetry, 2012. **108**(3): p. 1085-1092.
116. Sorolla, M. G., Dalida, M. L., Khemthong, P. and Grisdanurak, N., *Photocatalytic degradation of paraquat using nano-sized Cu-TiO_2/SBA-15 under UV and visible light.* Journal of Environmental Sciences (China), 2012. **24**(6): p. 1125-1132.
117. Li, X., Zheng, W., Pan, H., Yu, Y., Chen, L. and Wu, P., *Pt nanoparticles supported on highly dispersed TiO_2 coated on SBA-15 as an efficient and recyclable catalyst for liquid-phase hydrogenation*. Journal of Catalysis, 2013. **300**: p. 9-19.
118. Iijima, S., *Helical microtubules of graphitic carbon.* Nature, 1991. **354**(6348): p. 56-58.
119. Iijima, S. and Ichihashi, T., Single-shell carbon nanotubes of 1-nm diameter. 1993.
120. Pfeiffer, R., Pichler, T., Kim, Y. and Kuzmany, H., *Double-Wall Carbon Nanotubes*, in *Carbon Nanotubes*, A. Jorio, G. Dresselhaus, and M. Dresselhaus, Editors. 2008, Springer Berlin Heidelberg. p. 495-530.
121. Ren, W., Li, F., Chen, J., Bai, S. and Cheng, H.-M., *Morphology, diameter distribution and Raman scattering measurements of double-walled carbon nanotubes synthesized by catalytic decomposition of methane*. Chemical Physics Letters, 2002. **359**(3): p. 196-202.
122. engineringandbeyond.files.wordpress.com/2013/02/s10.jpeg, h., *CNTs image.*
123. Ruoff, R. S., Qian, D. and Liu, W. K., *Mechanical properties of carbon nanotubes: theoretical predictions and experimental measurements.* Comptes Rendus Physique, 2003. **4**(9): p. 993-1008.

124. Banerjee, S., Hemraj-Benny, T. and Wong, S. S., *Covalent surface chemistry of single-walled carbon nanotubes.* Advanced Materials, 2005. **17**(1): p. 17-29.
125. Calvert, P., *Nanotube composites: a recipe for strength.* Nature, 1999. **399**(6733): p. 210-211.
126. Kyotani, T., Nakazaki, S., Xu, W.-H. and Tomita, A., *Chemical modification of the inner walls of carbon nanotubes by HNO_3 oxidation.* Carbon, 2001. **39**(5): p. 782-785.
127. Overney, G., Zhong, W. and Tomanek, D., *Structural rigidity and low frequency vibrational modes of long carbon tubules.* Zeitschrift für Physik D Atoms, Molecules and Clusters, 1993. **27**(1): p. 93-96.
128. Popov, V. N., *Carbon nanotubes: properties and application.* Materials Science and Engineering: R: Reports, 2004. **43**(3): p. 61-102.
129. De Volder, M. F., Tawfick, S. H., Baughman, R. H. and Hart, A. J., *Carbon nanotubes: present and future commercial applications.* Science, 2013. **339**(6119): p. 535-539.
130. Thomsen, C., Reich, S. and Maultzsch, J., *Electronic Properties of Carbon Nanotubes.* Carbon Nanotubes: Basic Concepts and Physical Properties: p. 31-65.
131. Serp, P., Corrias, M. and Kalck, P., *Carbon nanotubes and nanofibers in catalysis.* Applied Catalysis A: General, 2003. **253**(2): p. 337-358.
132. Omidvar, H., Mirzaei, F., Rahimi, M. and Sadeghian, Z., *A method for coating carbon nanotubes with titanium.* New Carbon Materials, 2012. **27**(6): p. 401-408.
133. Satishkumar, B., Govindaraj, A., Mofokeng, J., Subbanna, G. and Rao, C., *Novel experiments with carbon nanotubes: opening, filling, closing and functionalizing nanotubes.* Journal of Physics B: Atomic, Molecular and Optical Physics, 1996. **29**(21): p. 4925.
134. Gerber, I., Oubenali, M., Bacsa, R., Durand, J., Gonçalves, A., Pereira, M. F. R., Jolibois, F., Perrin, L., Poteau, R. and Serp, P., *Theoretical and Experimental Studies on the Carbon-Nanotube Surface Oxidation by Nitric Acid: Interplay between Functionalization and Vacancy Enlargement.* Chemistry – A European Journal, 2011. **17**(41): p. 11467-11477.
135. Hou, P.-X., Liu, C. and Cheng, H.-M., *Purification of carbon nanotubes.* Carbon, 2008. **46**(15): p. 2003-2025.

136. Niyogi, S., Hamon, M., Hu, H., Zhao, B., Bhowmik, P., Sen, R., Itkis, M. and Haddon, R., *Chemistry of single-walled carbon nanotubes.* Accounts of Chemical Research, 2002. **35**(12): p. 1105-1113.
137. Chena, L., Pangb, X., Yua, G. and Zhanga, J., *In-situ coating of MWNTs with sol-gel TiO_2 nanoparticles.* Advanced Materials Letters, 2010. **1**(1), p. 75-78.
138. Yoneyama, H. and Torimoto, T., *Titanium dioxide/adsorbent hybrid photocatalysts for photodestruction of organic substances of dilute concentrations.* Catalysis Today, 2000. **58**(2): p. 133-140.
139. Gao, B., Peng, C., Chen, G. Z. and Li Puma, G., *Photo-electro-catalysis enhancement on carbon nanotubes/titanium dioxide (CNTs/TiO_2) composite prepared by a novel surfactant wrapping sol–gel method.* Applied Catalysis B: Environmental, 2008. **85**(1): p. 17-23.
140. Yen, C.-Y., Lin, Y.-F., Hung, C.-H., Tseng, Y.-H., Ma, C.-C. M., Chang, M.-C. and Shao, H., *The effects of synthesis procedures on the morphology and photocatalytic activity of multi-walled carbon nanotubes/TiO_2 nanocomposites*. Nanotechnology, 2008. **19**(4): p. 045604.
141. Jitianu, A., Cacciaguerra, T., Berger, M. H., Benoit, R., Béguin, F. and Bonnamy, S., *New carbon multiwall nanotubes - TiO_2 nanocomposites obtained by the sol-gel method.* Journal of Non-Crystalline Solids, 2004. **345-346**: p. 596-600.
142. Jitianu, A., Cacciaguerra, T., Benoit, R., Delpeux, S., Béguin, F. and Bonnamy, S., *Synthesis and characterization of carbon nanotubes-TiO_2 nanocomposites.* Carbon, 2004. **42**(5-6): p. 1147-1151.
143. Yang, H., Wu, S., Duan, Y., Fu, X. and Wu, J., *Surface modification of CNTs and enhanced photocatalytic activity of TiO_2 coated on hydrophilically modified CNTs*. Applied Surface Science, 2012. **258**(7): p. 3012-3018.
144. Kanu, I. and Achi, O., *Industrial effluents and their impact on water quality of receiving rivers in Nigeria.* Journal of Applied technology in Environmental sanitation, 2011. **1**(1): p. 75-86.
145. Jurado, A., Vàzquez-Suñé, E., Carrera, J., López de Alda, M., Pujades, E. and Barceló, D., *Emerging organic contaminants in groundwater in Spain: A review of sources, recent occurrence and fate in a European context.* Science of the Total Environment, 2012. **440**: p. 82-94.

146. Agrawal, A., Pandey, R. S. and Sharma, B., *Water pollution with special reference to Pesticide Contamination in India.* Journal of Water Resource and Protection, 2010. **2**(5): p. 432-448.
147. Zertal, A., Molnár-Gábor, D., Malouki, M., Sehili, T. and Boule, P., *Photocatalytic transformation of 4-chloro-2-methylphenoxyacetic acid (MCPA) on several kinds of TiO_2* Applied Catalysis B: Environmental, 2004. **49**(2): p. 83-89.
148. De Martino, A., Iorio, M., Xing, B. and Capasso, R., *Removal of 4-chloro-2-methylphenoxyacetic acid from water by sorption on carbon nanotubes and metal oxide nanoparticles*. RSC Advances, 2012. **2**(13): p. 5693-5700.
149. Organization, W. H., *Guidelines for drinking-water quality: recommendations*, 2004.**1**. World Health Organization.
150. Djebbar, K., Zertal, A. and Sehili, T., *Photocatalytic Degradation of 2, 4-Dichlorophenoxyacetic Acid and 4-Chloro-2-Methylphenoxyacetic Acid in Water by using TiO_2*. Environmental technology, 2006. **27**(11): p. 1191-1197.
151. Zertal, A., Sehili, T. and Boule, P., *Photochemical behaviour of 4-chloro-2-methylphenoxyacetic acid: Influence of pH and irradiation wavelength.* Journal of Photochemistry and Photobiology A: Chemistry, 2001. **146**(1–2): p. 37-48.
152. Tchaikovskaya, O. N., Karetnikova, E. A., Sokolova, I. V., Mayer, G. V. and Shvornev, D. A., *The phototransformation of 4-chloro-2-methylphenoxyacetic acid under KrCl and XeBr excilamps irradiation in water*. Journal of Photochemistry and Photobiology A: Chemistry, 2012. **228**(1): p. 8-14.
153. Sanchis, S., Polo, A. M., Tobajas, M., Rodriguez, J. J. and Mohedano, A. F., *Degradation of chlorophenoxy herbicides by coupled Fenton and biological oxidation.* Chemosphere, 2013. **93**(1): p. 115-122.
154. Bojanowska-Czajka, A., Drzewicz, P., Zimek, Z., Nichipor, H., Nałęcz-Jawecki, G., Sawicki, J., Kozyra, C. and Trojanowicz, M., *Radiolytic degradation of pesticide 4-chloro-2-methylphenoxyacetic acid (MCPA)—Experimental data and kinetic modelling.* Radiation Physics and Chemistry, 2007. **76**(11–12): p. 1806-1814.
155. Pirozzi, D. and Sannino, F., *Design of a multi-stage stirred adsorber using mesoporous metal oxides for herbicide removal from wastewaters*. Journal of Environmental Chemical Engineering, 2014. **2**(1): p. 211-219.

156. Šojić, D. V., Despotović, V. N., Abazović, N. D., Čomor, M. I. and Abramović, B. F., *Photocatalytic degradation of selected herbicides in aqueous suspensions of doped titania under visible light irradiation.* Journal of hazardous materials, 2010. **179**(1): p. 49-56.

Chapter 3
Experimental

This chapter entails details on how experiments were conducted to obtain the results described in chapters 4 and 5. The sol-gel method has been chosen for the synthesis of all materials due to the ease it offers in tailoring the properties of materials at a molecular level. The method can be used for preparing single or multi component materials. Instruments used and the corresponding measurements and characterizations of the physical and chemical properties of the materials synthesized are presented.

3.1 Materials and Chemicals

Materials used in all experiments were purchased and used without further modification except were specified. Tetraethyl orthosilicate (TEOS, 98%); poly(ethylene glycol)-block-poly(propylene glycol)-block-poly(ethylene glycol) also known as pluronic P123; pluronic F127; hydrochloric acid (HCl 32%); nitric acid (HNO_3, 69%); sulfuric acid (H_2SO_4, 98%); titanium (IV) isopropoxide (TIP, 97%); sodium hydroxide (NaOH, 97%); MCPA standard (95%); Methylene blue (MB), HPLC grade acetonitrile (99.99%), and Degussa P25 (a commercial TiO2 catalyst) were purchased from Sigma Aldrich (South Africa) and supplied by Capital Labs suppliers. Titanium spectrascan 1.002 ± 5 µg mL^{-1} ICP standard solution was supplied by Industrial Analytical; Terephtalic acid (TA) was purchased from Merk supplies Schuchardt, Germany. Multi walled carbon nanotues (MWCNTs, 95%) 8-15 nm outer diameter, 10-50 µm length, and 233 m^2/g surface area were purchased from Cheaptubes™ (Brattleboro, USA). Orthophosphoric acid (85%) was obtained from, Associated Chemical Suppliers, SA. Argon gas was purchased from Afrox Limited Gas Co., Durban, South Africa. 4-chloro-2-methylphenoxy acetic acid (MCPA) working solution was purchased from a hardware store, Durban, supplied by Grovinda, manufactured by Shaik-Agchem (MCPA registration holders). Ultrapure water with a resistivity of 18 MΩ cm was obtained from a Millpore Elix system.

Material synthesis was done on a Bibby HB502 single hotplate stirrer with optional operation of either one or both heating and stirring rate. Thermal values are stated were necessary in the synthesis details to follow, stirring speed was kept constant throughout all experiments at 400 revolutions per minute (RPM), unless stated otherwise. Conductivity measurements were recorded with an inoLab Cond Level 1 meter, supplied by Merck suppliers, Germany. A pH meter 8.27 pH lab (Metrohm Switzerland) equipped with an electrode (model 60220 100) stored in a 3 M KCl solution was used for all pH measurements. The weighing balance used was ta Mettler AE 200 and PJ3000 instruments. The ultra-sound probe employed was a UP400S ultrasonic processor (Hielscher Ultrasound Technology). The bath sonicator employed was a UMC 20 ultrasonic bath (Ultrasonic manufacturing company, SA). Micropipette 9001/13485 (100 – 1000 µL), from Dragon laboratories, USA was used to prepare certain solutions. The cuvettes used were Ultra Micro-Cell (range 220 – 900 nm; path-length 10 mm; volume 70 µL – 1.8 mL) supplied by Ocean Optics , Inc., Netherlands. The convection oven employed was a Labcon 1028K Ecoflomu which was manufactured by LABDESIGN ENGINEERING, SA. Filtrations were done in a Buchner filtration flask fitted with Whatman grade 4 filter papers.

All glassware used were soaked in acid and thoroughly washed with soap and warm water, then further rinsed with de-ionised water before use. The glass quartz reactor tube employed during calcinations was cleaned through heating to 800 ˚C in air for 2 hours and then rinsed with de-ionised water.

3.2 Characterization Instruments

The characterization instruments presented in this section were employed to investigate the physical and chemical properties of materials. Specifics on where materials were sent to external facilities for analysis are also clearly mentioned.

3.2.1 Nitrogen Sorption

Nitrogen desorption and adsorption isotherms and textural properties of materials were performed at -196 ˚C on the Micrometrics Tri-Star II 3030 version 1.03 instrument, supplied by Micrometrics, USA (**Figure 3.1**).

Figure 3. 1 Micrometrics Tri-Star II 3030 N_2 sorption instrument employed for textural analysis.

Total surface area and pore volume were determined using the Brunauer-Emmet-Teller (BET) equation and single point method respectively. Pore size distribution (PSD) was obtained from the adsorption branch of the nitrogen isotherm using the Barett-Joyner-Halenda (BJH) model.
The samples were prepared by degassing on Micrometrics Flow Prep (060) under nitrogen flow at 90 ˚C for 1 hour and 200 ˚C for a period of 4 hours before fitting them for analysis on the instrument.

3.2.2 Powder X-Ray Diffraction (XRD)

Materials were characterized by powder x-ray diffraction (XRD), low angle and wide angle XRD. XRD patterns were recorded on a D8 Advance diffractometer supplied by BRUKER AXS, Germany, with Cu-kα radiation of $\lambda K\alpha_1$ = 1.5406 Å using the PSD Vantec-1 detectors.
The angle was from range on 0 – 90 2theta degrees with a scanning speed of 0.5 seconds/step. X-ray tube voltage and current voltage were set at 40 kV and 40 mA respectively. Material analysis was done at iThemba LABS. The crystallite size was estimated from calculations of full-width at half-maximum (FWMH) of the XRD patterns using the Debye-Scherrer equation (**equation 3.1**) and the interplanar spacing were determined from Bragg's law (**equation 3.2**).

$$\text{Crystal size} = 0.9\lambda / B\cos\theta \qquad (\mathbf{3.1})$$

$$d = \frac{n\lambda}{2Sin\theta} \qquad (\mathbf{3.2})$$

3.2.3 Electron Microscopy

Images were obtained using a JEOL JEM 1010 transmission electron microscope (TEM), at an accelerating voltage of 100 kV. High resolution transmission electron microscopy (HRTEM) imaging were done on a JEOL JEM 2100 at an accelerating voltage of 100 kV. HRTEM employed the ECSI 10 digital micrographs software. The specimens for TEM and HRTEM imaging were prepared by dispersing ≈ 5 mg sample into 5 mL ethanol for 5 minutes using an ultra-sonic water bath. A Holey carbon grid was dipped into liquid sample and allowed to dry. **Figure 3.2** depicts the HRTEM instrument.

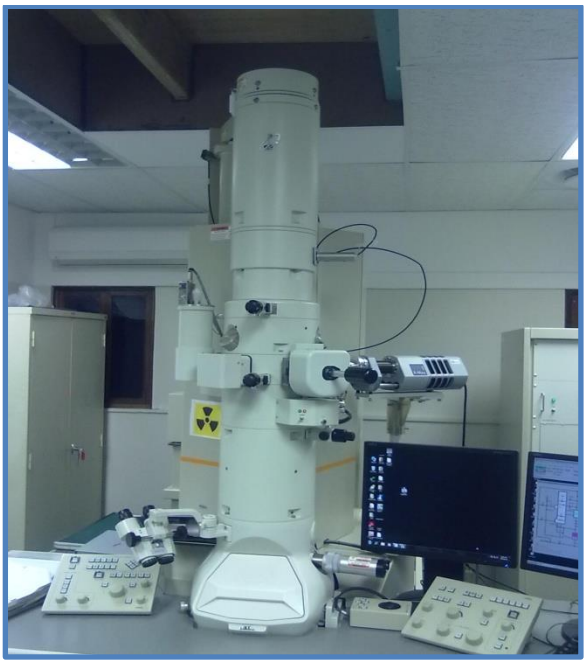

Figure 3. 2 JEOL JEM 2100 HRTEM instrument.

Other morphological investigations were carried out on a LEO 1450 scanning electron microscope (SEM), using the SmartSEM software Version 5.03.06 (**Figure 3.3**). The accelerating voltage on the SEM was set at 10 kV. The samples were prepared by firmly placing a piece of double sided sticky carbon tape onto aluminium stubs , and pressing the powder samples onto the exposed side of the tape. Excess samples was gently removed by tapping the stubs on the side of the work bench before mounting in the instrument. Electron dispersive X-ray (EDX) spectroscopy was used to determine the elemental composition of materials. EDX, Bruker X–ray spectroscopy was used in conjunction with the SEM LEO 1450 for EDX analysis with 80 mm^2 X-Max, Oxford instruments detector. The software employed was Edx Aztec. Parameters were a scanning rate between 5 to 10 kilocounts per second, accelerating voltage of 20 kV and a working distance between 5 – 10 mm. The samples were further treated by coating the stab with gold to avoid charging of the samples during analysis.

Figure 3. 3 LEO 1450 SEM instrument.

3.2.4 Thermo-Gravimetric Analysis

Thermal properties of materials were investigated through thermo-gravimetric analysis (TGA) **Figure 3.4**, is a photo of the PerkinElmer Simultaneous Thermal Analyzer (model STA 6000) that was used to analyse all of the samples. Samples were analysed with a heating rate of 10 ˚C min^{-1} under air flow. Air was introduced to the samples at a rate of 25 mL min^{-1} in order to maintain an oxidizing environment. Sample runs were carried out in 100 µL ceramic pan. Pans were equilibrated to 40 ˚C in the TGA and then heated to 1000 ˚C. Approximately 10 mg was used for analysis of all samples.

Figure 3. 4 STA 6000 TGA instrument employed for thermal properties of the materials.

3.2.5 Raman Spectroscope

Raman spectroscopy measurements were done using a DeltaNu Advantage 532^{TM} spectrometer (purchased from USA) with 1800 lines mm^{-1} grating (**Figure 3.5**). The spectrometer employed the NuSpec^{TM} software, with excitation using a class 3b diode laser operated at an excitation wavelength of 532 nm. The laser was operated at 15 mW, a 2D charge couple device (CCD) detector was used with an integration time of 60 seconds. The sample accessory employed was the Right Angle Input Optics, the sample was placed in the sample holder and the focal length was centred at the irradiation centre at 16.45 mm. The spectrometer was then covered with a black cloth before analysis.

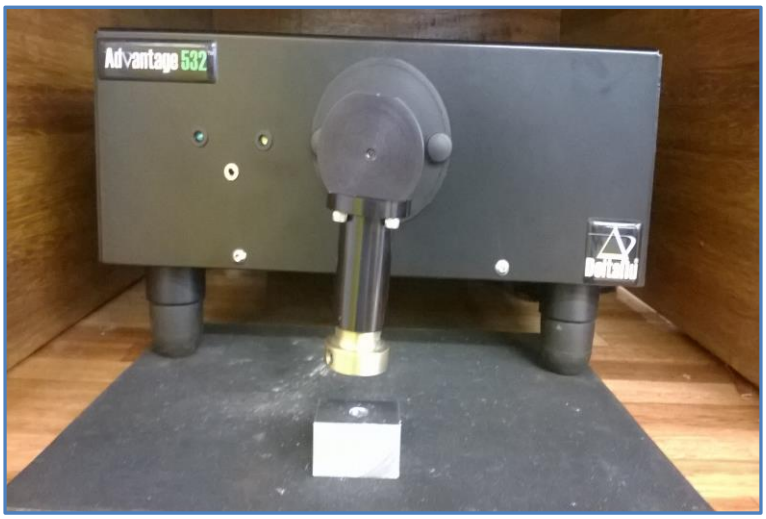

Figure 3. 5 DeltaNu Advantage 532^{TM} Raman spectrophotometer.

3.2.6 Fluorescence Spectroscope

Photoluminescence (PL) studies were carried out on a Fluorescence Spectrophotometer, FL WinLab version 4.00.03 Perkin Elmer Inc., graph server v1.60 software (model LS55, PerkinElmer) using a front probe surface accessory (LS55 model solid probe). The excitation wavelengths were varied at 310, 320, 350 and 390 nm, Operational parameters were set at an excitation slit of 5.0 nm; emission slit of 0.0 nm at a scan speed of 120 nm. min^{-1}.

3.2.7 Inductively Coupled Plasma-Optical Emission Spectroscopy (ICP-OES)

The weight percentage of TiO_2 on the SBA-CNT composites was estimated using the inductively coupled plasma-optical emission spectroscopy (ICP-OES), Perkin Elmer Optima 5300 DV equipped with concentric nebulizer (**Figure 3.6**).

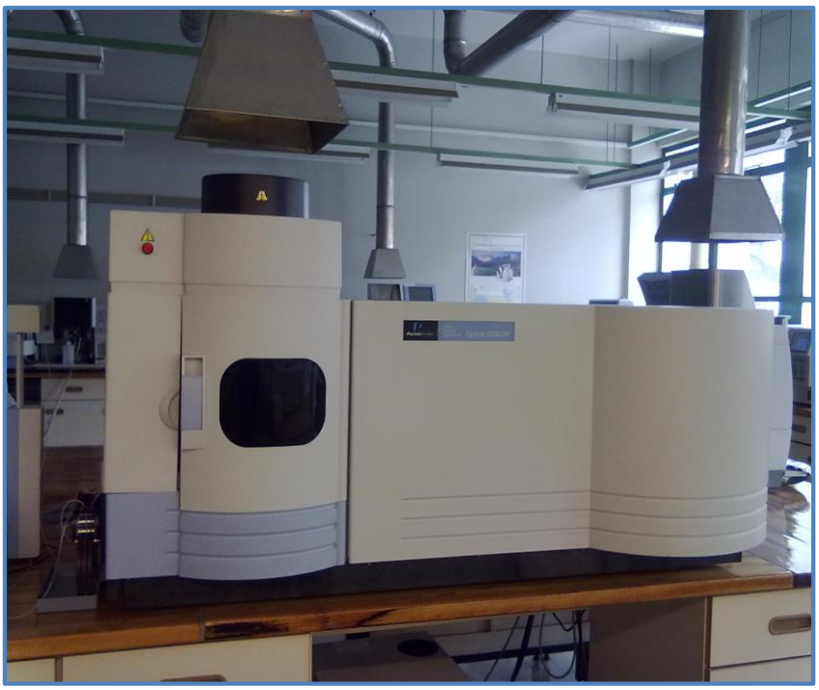

Figure 3. 6 ICP-OES (Perkin Elmer Optima, 5300 DV) employed for metal analysis.

The operating conditions of the ICP-OES instrument are given in **Table 3.1**.

Table 3. 1 ICP-EOS instrumental operating condition for analysis.

Power	1300 W
Plasma gas flow rate	15 L min^{-1}
Auxiliary gas flow rate	0.2 L min^{-1}
Nebulizer gas flow rate	0.8 L min^{-1}
Pump flow rate	1.5 mL min^{-1}
Wavelength	336.121 nm
Replicates	3

The calibration curve of Ti was prepared from a series of standard solutions of 0, 2, 4, 6, 8, and 10 mg L^{-1}. The regression co-efficient of the calibration was 0.9988.

To estimate the quantity of Ti metal in the TiO_2/SBA-CNT composite, 5 mg of the respective sample was dissolved in 10 mL of concentrated H_2SO_4 in a 50 mL beaker. The mixture was stirred at 140 RPM for 1 hour at 200 ˚C. The mixture was left to cool to room temperature and filtered through a PVDF 0.45 µm filter into the ICP vial for analysis.

The Ti standards were analyzed each time before analysis of the respective samples. **Equation 3.3** was then used to calculate the elemental quantity of TiO_2 in the composites.

$$\% \text{ of } TiO_2 \text{ in the composite} = [\text{conc (mg. } L^{-1}) \times \text{vol L} \times 1.67] / \text{sample (g)} \quad (\mathbf{3.3})$$

Whereby the concentration was given by the ICP-OES in mg L^{-1} for the Ti metal in the composite; the volume used was 50 mL for all the samples and the sample weight were 5 mg. The value of 1.67 results from the molar mass of TiO_2 divided by the molar mass of Ti. This conversion was necessary since the ICP-EOS reports only the concentration of Ti in the samples.

3.2.8 UV-Vis Diffuse Reflectance Spectrometer (DRS)

Diffuse Reflectance spectra were measured using an Ocean Optics spectrometer (high resolution HR 2000), employing the ocean optics Spectrasuite software and a tungsten halogen light source. Light was passed through fiber optic cables, to the sample and eventually to the spectrometer, the fiber optic cables (QP 600-2-vis-BX model 727-733-2447) were suitable for wavelengths between 187 and 2100 nm. The samples were analyzed on a 1/4" SS Dip Probe, T300-RT-UV-Vis, were barium sulphate was employed as a reference material prior to each analysis.

3.2.9 High Performance Liquid Chromatography (HPLC)

MCPA product analysis was performed using high performance liquid chromatography (HPLC) on an Agilent Technologies 1100 series liquid chromatography system. The instrument used a UV-Vis PDA (D2&W) lamp detector. Wavelength range for the detector was 190 – 800 nm. The Zorbax eclipse XDB C18 (150 mm x 4.6 mm), i.d. 5 µm particle size column was employed and oven temperature was set to 30 ˚C. The mobile phase was a 1:1 (V/V) ratio of acetonitrile and orthophosphoric acid acidified water with a pH between 2.70 – 2.80. Operational parameters of the HPLC were guided by Sojic et al. [1].

The MCPA calibration curve was obtained from running known concentrations of the MCPA standard. An MCPA stock solution was prepared by dissolving 10.00 mg MCPA into 100 mL Millipore water, and then employed to prepare 0.5 – 10 mg L^{-1}.

Equation 3.4 was used to calculate the volume of MCPA solution required to prepare concentrations of 0.5, 2, 4, 6, 8 and 10 mg L^{-1} respectively.

$$C_1V_1 = C_2V_2 \quad (\mathbf{3.4})$$

Standard working solutions of 2, 4, 6, 8 and 10 mg L^{-1} were also prepared from following similar calculations. During analysis, 20 µL of the analyte was injected at 1 mL min^{-1} flow rate. Analysis was done at the absorption wavelength of MCPA at 290 nm. The concentration of MCPA was quantified from the constructed calibration curve of area versus concentration with a regression co-efficient of 0.9999. For each analysis, the area of the peak (y) appearing at retention time of ≈ 3.85 minutes was converted to concentration through solving for x in **equation 3.5**.

$$y = 50077x - 129.16 \quad (\mathbf{3.5})$$

3.3 Synthesis Procedures

3.3.1 Acid Treatment of Multi-walled Carbon Nanotubes (MWCNTs)

The method utilized for functionalising CNTs were guided by Hou et al. and Shamsuddin et al. [2, 3]. In the typical experiment, 2.09 g of MWCNTs and 100.13 g HNO_3 were placed into a 250 mL beaker. The MWCNTs were dispersed in the acid using an ultrasound probe. The ultrasound energy was applied for 20 minutes at 30% amplitude with 0.4 cycles. The composition was refluxed at 80 ˚C for 4 hours. After refluxing in the acid, the mixture was allowed to cool to room temperature and then the CNTs were recovered by filtering under vacuum and washing with approximately 3 L H_2O until the filtrate had a pH of ≈ 5.95. The black product was dried in an oven at 100 ˚C for 18 hours, and these were denoted as “aCNTs” for acid treated MWCNTs. Several aCNT samples were prepared using the same procedure.

3.3.2 Synthesis of SBA-15

The following method was adapted from Meynen and Vansant [4]. During the preparation of SBA-15, a solution of H_2O : HCl (130.18 g : 20.26 g) was prepared in a 400 mL beaker.
To this solution 4.23 g of surfactant P123 was added and the mixture was stirred for 30 minutes at room temperature to ensure that surfactant (P123) was completely dissolved. The mixture was then transferred into a 500 mL three-necked round bottom flask (fixed with a thermometer, and a condenser opened to air) and was refluxed at 50 ˚C for 1 hour. 9.13 g of tetraethyl orthosilicate (TEOS) was added dropwise to the mixture and stirring was continued for a further 6 hours 30 minutes. The magnetic stirring was then stopped and the temperature was increased to 80 ˚C. The solution was cooled to room temperature after heating at 80 ˚C for 15 hours 30 minutes without stirring.

The product was recovered through filtration under vacuum and washed with 3 portions of 25.00 g de-ionized water. The pure white product was collected and dried in an oven set at 100 ˚C for 3 hours. After drying, the solid product was calcined in a muffle furnace system at 550 ˚C for 6 hours, with heating rate 1 ˚C per minute (˚C min^{-1}). In a typical experiment, 5.35 g was calcined and the recovered mass was 3.12 g. The synthesis of SBA-15 was done in duplicate.

3.3.3 Synthesis of SBA-15 Coated MWCNTs (SBA-CNT Composites)

This section describes the coating of the functionalized CNTs (aCNTs) with SBA-15. Similar method to SBA-15 synthesis was used with the exception of introducing CNTs at the initial stage of the synthesis method.

4.00 g of P123 and 0.50 g aCNTs were weighed and placed in a 400 mL beaker. 130.00 g de-ionized H_2O and 20.00 g HCl were then added to the beaker, the mixture was treated with an ultrasonic probe for 20 minutes. The mixture was then transferred into a 500 mL two-necked round bottom flask with a thermometer, and a condenser (opened to air) attached. The mixture was heated to 45 ˚C and 0.19 g TEOS (for an estimated 10 wt. % SBA-15 coating on the CNTs) was added dropwise.

Stirring was stopped and the temperature was increased to 80 ˚C and the mixture was left standing at 80 ˚C for 15.5 hours. The solution was allowed to cool to room temperature and the product was recovered through filtration under vacuum and washing with 3 portions of 25.00 g de-ionized water. The black product was dried in an oven at 100 ˚C for 18 hours. After drying, the solid product was calcined in a muffle furnace system at 400 ˚C for 6 hours, with a heating rate of 1 ˚C min^{-1}. The typical yield was 0.38 g.

The same procedure was followed to coat 20 and 30 wt. % SBA-15 on CNTs. For the 20 wt., approximately 0.44 g TEOS was used and for 30 wt. %, 0.79 g TEOS was used. The yields were 0.49 g and 0.57 g for 20 and 30 wt. % SBA-15 respectively. The synthesis of these materials was done in triplicate. The amounts of TEOS used during the respective experiments were calculated according to equations in **appendix A 1.2.**

3.3.4 Synthesis of Mesoporous Titanium Dioxide

Prior to synthesizing the catalyst, various optimization experiments were carried out using different weight ratios of the surfactant F127. The optimization was carried out in order to evaluate the critical micelle concentrations (CMC) for the surfactant F127 in the solvent system of choice and the effect of the number of moles of the titania precursor (TIP). The CMC experiments were modified from methods reported by Fuguet et al. [5]. In the conductivity experiments, 2.50 g – 25.00 g F127 was dissolved in varying solvent systems of EtOH:H_2O at room temperature. Different mass of F127 were completely dissolved in fixed volumes of the solvent systems according to **Table 3.2**. The conductivity of the solutions was measured and a plot of conductivity versus F127 concentration indicated the CMC of the surfactant ideal for the solvent system **Appendix A1**.

Table 3.2 Critical micelle concentration experimental compositions.

F127 (g)	2.50	5.00	7.50	10.00	12.50	15.00	17.50	20.00	22.50	25.00
Mass of solvent (g)	97.50	95.00	92.50	90.00	87.50	85.00	82.50	80.00	77.50	75.00
Solvent ratio (g)*	50:50		60:40		60:40		80:20		80:20	

*Solvent system was made of H_2O:EtOH.

3.3.4.1 Determination of CMC from Titanium Isopropoxide (0.005 moles) with [15%] and [25%] F127

After considering the CMC concentration of pluronic F127, the effect of TIP concentration was monitored. In the experiments, 15.00 g and 25.00g of F127 were weighed into respective 400 mL beakers. Ethanol (50.00 g) was added to each beaker and both beakers where treated in an ultrasound probe for 20 minutes and stirred for 10 minutes until the surfactant was fully dissolved. About 1.26 g of TIP was slowly added to the respective solutions and stirring was continued for 10 minutes. De-ionized water (50.00 g) of pH 1.09 was added drop-wise to the respective solutions and stirring was continued for another 1 hour before the respective mixtures were left to stand and age in air without stirring for 24 hours. The respective mixtures were transferred to an oven set at 100 ˚C for 6 days. The samples were then heat treated under Argon flow at 400 ˚C for 6 hours with a heating rate of 1 ˚C min^{-1}. They were further calcined in air at 400 ˚C for a period of 8 hours with a heating rate of 1 ˚C min^{-1}.

The mole ratio of the sol-gel solution of [15%] w/w surfactant was 0.0012:0.005:1.085:2.778 and of the mole ratio of the [25%] w/w surfactant was 0.0020:0.005:1.085:2.778 (F127:TIP:EtOH:H_2O).

3.3.4.2 Determination of Titanium Isopropoxide (0.015 moles) with [15%] and [25%] F127

Similar methods as in above were followed to prepare TiO_2 using higher concentrations of TIP. The differences in the experiments were the mole compositions of the solutions. The mole ratio of the sol-gel solution for the [15%] w/w surfactant was 0.0012:0.015:1.085:2.778 and that of the [25%] w/w surfactant was 0.0020:0.015:1.085:2.778 (F127:TIP:EtOH:H_2O). After stirring the respective beakers of [15%] and [25%] of F127 solution mixtures for 10 minutes, a slow addition of 3.78 g TIP was made to each solution. The solutions were stirred for a further 10 minutes before an addition of the de-ionized water (pH 1.06) was made. After stirring for 1 hour, the solutions were left to age in air. Similar aging and thermal treated as those in above (**section 3.3.4.1**) were considered for these samples.

The materials prepared from using the [15%] and [25%] of F127 with 0.005 and 0.015 moles of TIP were characterized and the method yielding desirable properties of mesoporous TiO_2 identified and these method was employed for the synthesis of the actual TiO_2 catalysts.

3.3.5 Synthesis of Mesoporous TiO_2 Nanoparticles Catalyst

In the actual catalyst synthesis, 15.01 g of F127 was weighed into a 400 mL beaker. To the beaker 50.00 g of ethanol was added and the mixture was treated with an ultrasonic probe for 20 minutes and stirred for 10 minutes. 1.26 g TIP was slowly added into the solution and stirring was continued for a further 30 minutes. De-ionized water solution (50.00 g) with pH 1.09 was added drop-wise to the stirring solution. Magnetic stirring was continued for a further 1 hour before the mixture was left to stand and age in air without stirring. The mole ratio of the sol-gel solution was 0.0012: 0.005: 1.085: 2.778 (F127: TIP: EtOH: H_2O). The solution was left to age at room temperature for 24 hours, and then transferred to age in an oven set at 100 ˚C for 6 days. The samples were transferred into a crucible quartz boat and then fixed in a glass quartz reactor tube for calcination experiments. The samples were then heat treated under Argon flow at temperatures of 400 ˚C for 6 hours with a heating rate 1 ˚C min^{-1}, then further calcined in air at 400 ˚C for 8 hours at 1 ˚C min^{-1} heating rate.

3.3.6 Synthesis of TiO_2 Nanoparticles Supported on Different Materials

The sol gel method was employed for the synthesis of all titania supported composites. In a typical synthesis, 15.00 g of F127 surfactant was mixed with 0.80 g of the supporting material (i.e CNTs, SBA-15 or 30 wt. % SBA-CNTs) and 50.00 g of ethanol in a 400 mL beaker. The mixture was treated with an ultrasonic probe for 20 minutes before they were stirred for 10 minutes. Thereafter, 0.44 g of TIP (to yield 10 wt. % TiO_2) was added in a drop-wise manner. The amount of TIP to be added was determined from a series of calculations (**appendix A 1.2)**. 50.00g de-ionized water of pH ±1.05 was added drop-wise into the solution mixture after 30 minutes. Stirring was continued for a further 1 hour and the solution was left to age at room temperature for a period of 24 hours, then transferred to age in an oven set at 100 ˚C for 6 days.

The same methodology was employed under the same conditions for the synthesis of the 5 and 20 wt. % TiO_2/SBA-CNT composites. The variation in the synthesis method was in the weight of the TIP solution that was added into the mixture. Respectively 0.26 g and 0.82 g of TIP were added drop-wise for the 5 and 20 wt. % TiO_2 composites respectively.

It is important to note that the mass of TIP calculated was added with 0.110 g of TIP during synthesis because TIP sticks to the walls of apparatus used for measurements and transferring. This addition was thus done to account for any TIP precursor which might be lost to the walls of the 50 mL beaker used to weigh it in and the pasteur pipette used to add it into the respective solutions.

After aging the respective samples, they were heat treated under Argon flow at 400 ˚C for 6 hours with a heating rate of 1 ˚C min^{-1}, then further calcined in air at 400 ˚C for 8 hours at a heating rate of 1 ˚C min^{-1}. **Figure 3.7** illustrates the muffle furnace set up employed during heat treatment of materials in an argon environment. The materials were synthesized in triplicate.

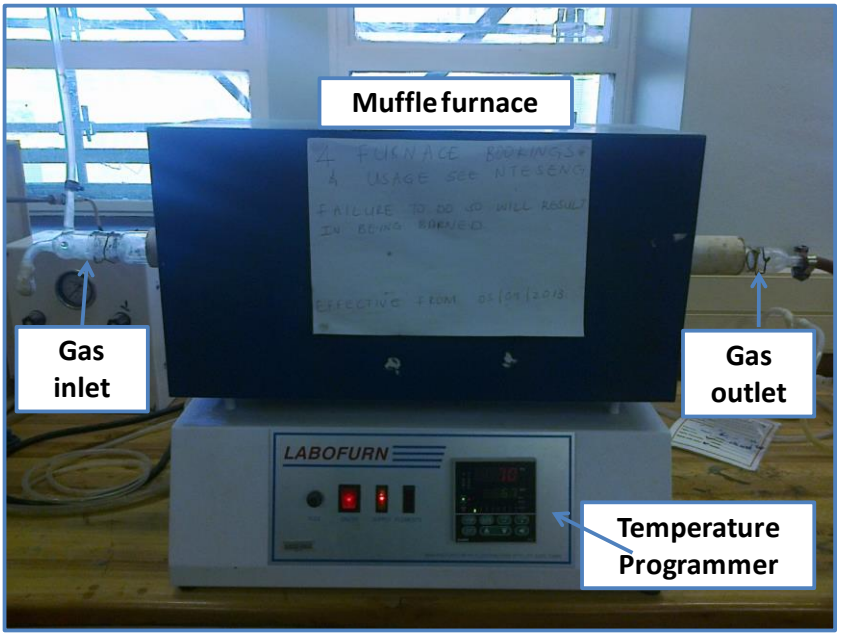

Figure 3. 7 labelled photograph of the experimental setup used for the heat treatment of materials in an inert environment using a tube furnace (LABOFURN).

3.4 Photo-catalytic Activity Experiments

Figure 3.8 depicts a sketch of the experimental setup used during the photo-catalytic activity tests. Whereby, the visible irradiation light source was a 32 Watt (W) model 220-240V/4U/6400K day light halogen lamp. The lamp was kept inside a borosilicate glass tube throughout the experiments.

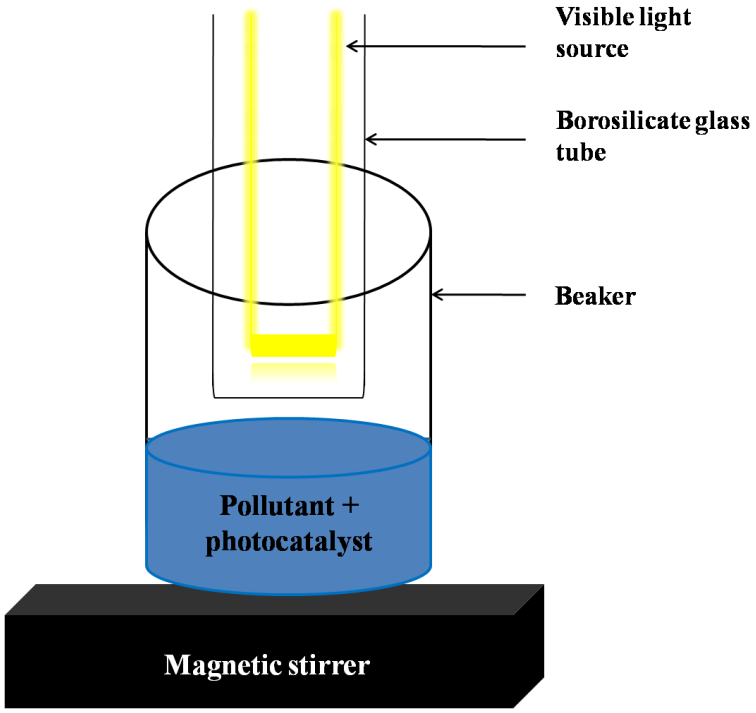

Figure 3. 8 Experimental set-up of the photo-catalytic activity test.

Solutions for photo-catalytic measurements were prepared by adding 20 mg of the respective catalyst to 150 mL aqueous solution of MB (10 mg L^{-1}) in a 400mL beaker. The solution was immediately covered with foil paper and ultra-sonicated in a bath for 10 minutes followed by stirring in the dark for 1 hour at room temperature. The solution was then exposed to visible light irradiation source while stirring at room temperature. 5 mL aliquots were withdrawn over 160 minutes at every 20 minutes intervals. The sample was then centrifuged (Hettich centrifuge, Mikro 120) for 10 minutes at 140 revolutions per minute (RPM) X100. The supernatant solution was transferred to a cuvette (path-length 10 mm; volume 70 µL – 1.8 mL) and placed in the UV-Vis spectrophotometer for analysis.

The de-colorization of the dye was then evaluated by measuring the absorption of methylene blue solution at the most intense band appearing at 665 nm with a UV-Vis spectrophotometer. MB was employed as a model pollutant in order to proof the concept and to determine the optimum catalyst composites prior to testing the activity of such catalyst on an environmentally problematic real world pollutant; specifically, 4-chloro-2-methylphenocyacetic acid (MCPA) herbicide.

For the transformation of MCPA, an aqueous solution of 8 mg L^{-1} MCPA was prepared from the purchased solution (containing 400 g L^{-1} MCPA) using de-ionised water. The photo-degradation setup was similar to the one presented for MB studies, **Figure 3.8**, and other experimental parameters were maintained as in for MB, though for MCPA transformation, 10 mg catalyst was dispersed in a 100 mL solution (0.1 mg L^{-1}). The solution was pre-treated in a similar manner as the one reported for MB studies. The activities of the catalysts were tested by withdrawing 1 mL at 20 minutes sampling intervals and the catalyst was then separated by filtering through 0.45 µm PVDF filters into HPLC vials. The vials were immediately covered with foil paper to prevent further interaction with light prior analysis on the HPLC.

Photo-catalytic transformation of MCPA was carried out under different conditions such as solution pH, catalyst concentration and MCPA concentration. These experiments were conducted in order to find optimum conditions for our employed composites during the reaction and also to test the efficiency of the materials under different conditions. Similar methods to those described for MB studies were followed. Solution pH was adjusted with 25 mM NaOH or (85%) H_2SO_4 and resulted in pH 2.9 and 8.2, while natural pH was measured and found to be at 4.68. Catalyst concentrations were 0.1, 0.5 and 1 g L^{-1}. MCPA concentrations ranged from 8 mg L^{-1} to 2 mg L^{-1}.

3.5 Data Analysis

Raw data from various experiments were collected and processed using Microsoft Excel. All plots were then drawn using the OriginPro 8 software.

3.6 References

1. Šojić, D. V., Despotović, V. N., Abazović, N. D., Čomor, M. I. and Abramović, B. F., *Photocatalytic degradation of selected herbicides in aqueous suspensions of doped titania under visible light irradiation.* Journal of hazardous materials, 2010. **179**(1): p. 49-56.
2. Hou, P.-X., Liu, C. and Cheng, H.-M., *Purification of carbon nanotubes.* Carbon, 2008. **46**(15): p. 2003-2025.
3. Shamsuddin, S. A., Halim, N. U. A., Deraman, N. and Hashim, U., *The Characterization Study of Functionalized Multi-Wall Carbon Nanotubes Purified by Acid Oxidation*, 2011. IEEE Regional Symposium on Micro and Nanoelectronics (RSM). p. 263-265.
4. Meynen, V., P. Cool, and E. Vansant, *Verified syntheses of mesoporous materials.* Microporous and Mesoporous Materials, 2009. **125**(3): p. 170-223.
5. Fuguet, E., Ràfols, C., Rosés, M. and Bosch, E., *Critical micelle concentration of surfactants in aqueous buffered and unbuffered systems.* Analytica Chimica Acta, 2005. **548**(1): p. 95-100.

Chapter 4
Results and Discussions on Physico-Chemical Properties of Nanocomposites

4.1 Effects of Acid Treatment on MWCNTs and Influence of SBA-15 Thin Film Coating on Acid Treated MWCNTs.

This section focuses on the physical and chemical properties of the prepared materials which will be employed to support the mesoporous TiO_2 nano-particles. The materials presented have been prepared according to Chapter3, section 3.3.1 – 3.3.3 and the materials have been characterised from methods presented in section 3.2. The section will begin with characteristics of the commercial and acid treated multi-walled carbon nanotubes, followed by the functionalization of the tubes with thin film SBA-15. Analysis on the effects of modifying CNTs will be presented together with an overview on the materials chosen as supports for TiO_2."

4.1.1 Raman Spectroscopy Data Analysis

Raman spectroscopy is an informative characterization technique for CNTs and their composites [1], and it also a powerful technique in the identification of incorporated framework materials such as metal oxides [2]. The relatively inert nature of MWCNTs inhibits further chemistry on the tube walls and usually results in sparse or few particles attaching to the sidewalls of CNTs. Therefore, acid treatment (or some form of pre-treatment step) is usually a very necessary step prior to any modification to the tubes [3, 4]. **Figure 4.1** exhibits Raman spectrum of raw MWCNTs (rCNTs) and acid treated MWCNT (aCNTs).

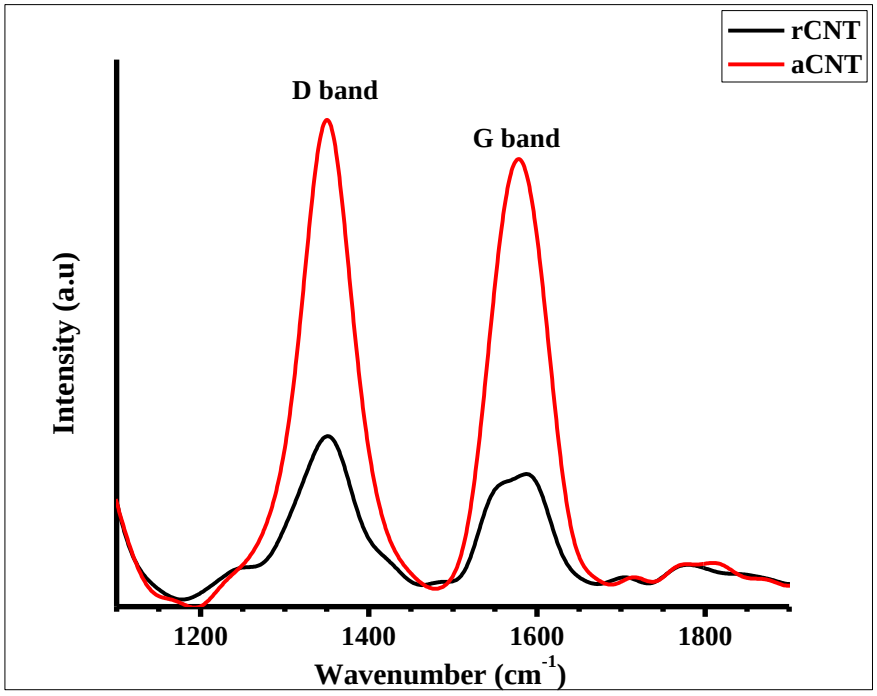

Figure 4. 1 Raman spectrum of raw and acid treated CNTs, rCNTs and aCNTs respectively.

The spectrum show characteristic bands of CNTs, the D and G bands at approximately 1350 and 1580 cm^{-1} respectively. Literature associates the D band with disorder (sp^3 carbons) and the G band is associated with the crystalline graphite structures (sp^2 carbons) of carbon nanotubes [5, 6]. The integrated area of the D and G band intensity ratio (I_D/I_G) for rCNTs and aCNTs were calculated to be 1.37 and 1.11 respectively. The bands were integrated from the mathematical area integration input method found within the OriginPro 8 software.

An increased I_D/I_G ratio of aCNTs as compared to rCNTs would have suggested an increase in the disordered carbons as a result of attached functional groups and openings of the tube ends [3, 6]. However, the observed decrease of I_D/I_G ratio suggest that there was an increase in the graphitic nature of the tubes, this increase in the graphitic (G) band is attributed to the removal of amorphous carbon which may have been on the tube walls, or separate particle of amorphous carbon. The study by Gerber et al. [7] explored the effects of temperature and time on the oxidation of CNTs with nitric acid, they observed similar phenomena of a decreasing I_D/I_G ratio and cleaner surface morphology for acid treated tubes.

Although the study by Fu et al. [6] attributed their decreasing I_D/I_G ratio to the formation (opening) of more tube ends. The FWHM for the D and G bands in acid treated CNTs is narrower than those in raw CNTs (**Table 4.1**). The decrease in FWHM is associated with increased crystallinity within the acid treated CNTs [8]. The I_D/I_G ratio and FWHM both show similar trends that suggest increase of graphitic carbon after acid treatment, as a result of removing amorphous carbons.

Table 4. 1 Raman spectrum parameters on CNTs and SBA-CNT composites.

Sample	**D band**		**G band**		**Ratio**
	Position (cm^{-1})	FWHM (cm^{-1})	Position (cm^{-1})	FWHM (cm^{-1})	**(I_D/I_G)**
rCNTs	1351	74.85	1587	85.16	1.37
aCNTs	1350	70.14	1578	76.52	1.11
10SBA-CNT	1352	65.92	1577	81.70	1.46
20SBA-CNT	1351	66.00	1576	76.90	1.21
30SBA-CNT	1352	35.09	1577	78.55	1.42

Raman spectrum of SBA-15 (**Figure 4.2**) exhibit spectroscopic features reported for amorphous SiO_2. The bands observed at 410 cm^{-1} and 813 cm^{-1} are assigned to siloxane linkage (Si-O-Si) and bands at 493 cm^{-1} and 654 cm^{-1} are assigned to the four- and three-fold membered siloxane rings respectively. The very intense band at approximately 1134 cm^{-1} is related to surface silone (O_3Si-OH) streching vibrations [2, 9].

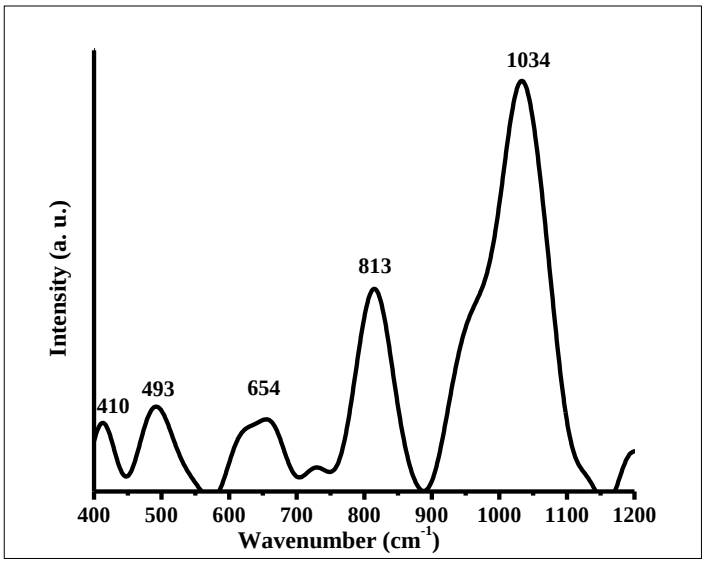

Figure 4. 2 Raman spectrum of SBA-15.

The SBA-CNT composites (**Figure 4.3**) show characteristic bands for both SBA-15 and CNTs at the expected wavenumbers. It was noted that the SBA-15 peaks at 654 and 813 cm^{-1} were not well resolved with the spectrum for the composites, and this was thought to be due to the low content of silica within all the composites. Within the composites, the most predominant peak of SBA-15 appeared at around 1050 cm^{-1} for the O_3Si-OH stretching vibrations.

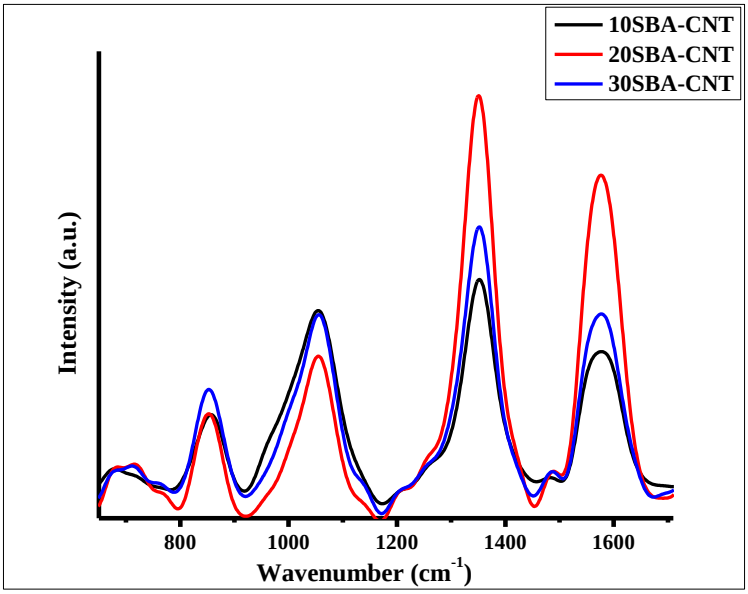

Figure 4. 3 Raman spectrum of SBA-15 coated CNTs composites.

The variation of the Raman spectrum analysis could indicate a covalent attachment between CNTs and SiO_2 [10]. The I_D/I_G ratio of the CNTs increased with the coating of SBA-15, when compared to aCNTs (**Table 4.1**). The increased ratio implies that the graphitic vibrations of the CNTs have been minimized as a result of the silica coating [11]. Similarly, the increase in D band intensity for functionalized samples is due to changes in the nanotube structure brought upon by interaction with SBA-15. When examining the FWHM for the D band, the value decreased significantly after incorporating SBA-15 on the CNTs. The decrease imply that the degree of disorder on the nano-tubes is being reduced. However the broad FWHM D band imply that the CNTs may have more defects introduced onto the sidewalls as the bonding interactions between silica and CNTs increases. Consequently the FWHM for the G band increased for the 10 wt. % sample, and remained largely unchanged for the 20 and 30 wt. % samples, these values could signify little to no change within the graphitic carbon structures which are not involved in bonding [8, 12]. During the growth of SBA-15 onto the CNTs, most of the vacant nucleattion sites on the CNT walls may have been occupied or made less accessible by the surfactant used. Thus relatively few defect sites may have been bonded by the SiO_2; however at the highest loading used, the greater decrease in the FWHM of the D-band may indicate that sufficient amount of silica was able to bind the defect sites of the CNTs despite the amount of surfactant used.

4.1.2 Electron Microscopy Investigations

Electron microscopy is a powerful technique that is used to study and understand structures at the nano level. It was through the use of high resolution transmission electron microscope (HRTEM) that the characteristic structure of the CNTs and SBA-15were identified [13].

4.1.2.1 Micrographic Analysis of Raw and Acid Treated Carbon Nanotubes

Figure 4.4 (**a and b**) show the commercial CNTs with amorphous carbons and closed tube ends. The amorphous carbon is identified from the tube wall roughness. Images c and d for aCNTs show a smooth nanotube wall with an open end.

The open tube ends were observed from various micrographs (insert in image d). The morphology results correlate well with the I_D/I_G ratio from the Raman analysis which suggested that the amorphous carbons on the wall of the CNTs may have been removed and also the tube ends of the CNTs may have been opened during acid treatment.

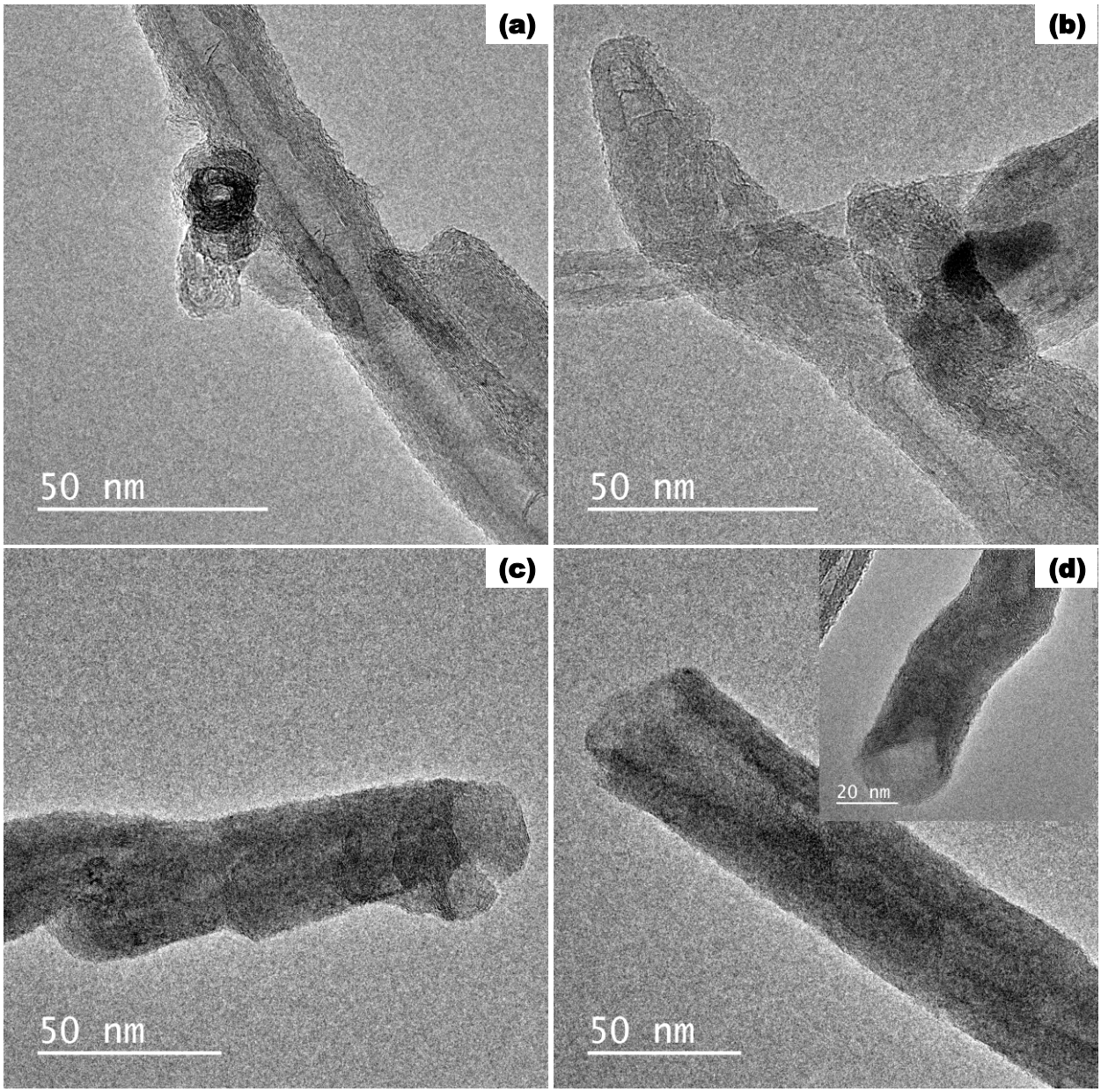

Figure 4. 4 Micrographs of commercial CNTs and acid treated CNTs, denoted rCNTs and aCNTs respectively. HRTEM images of rCNTs (a - b) and aCNTs (c – d) with insert showing open tube end (d).

4.1.2.2 Electron Microscopy Analysis on SBA-15

Figure 4.5 exhibit the morphological structure of SBA-15 with ordered pores arranged in a 2D hexagonal structure. The wall thickness has been measured from the micrographs using Image J software to be 4.68 nm. SBA-15 is reported to be hydrothermally, chemically and thermally stable because of this thick, uniform and ordered pore walls [14].

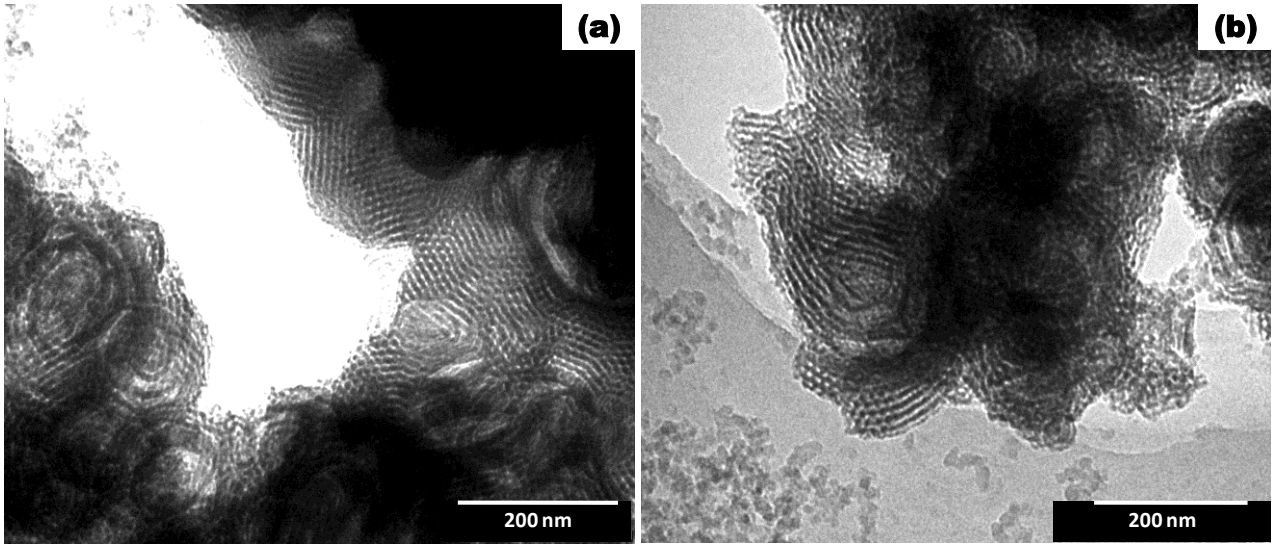

Figure 4. 5 TEM micrographs of SBA-15 depicting highly ordered pores (a and b).

SEM images (**Figure 4.6**) show the characteristic curved walls of SBA-15. Similar structures using SEM analysis have been observed by various authors in the literature [14]. Such walls are advantageous in catalysis since they could allow ease of transport of reactants and product molecules [14].

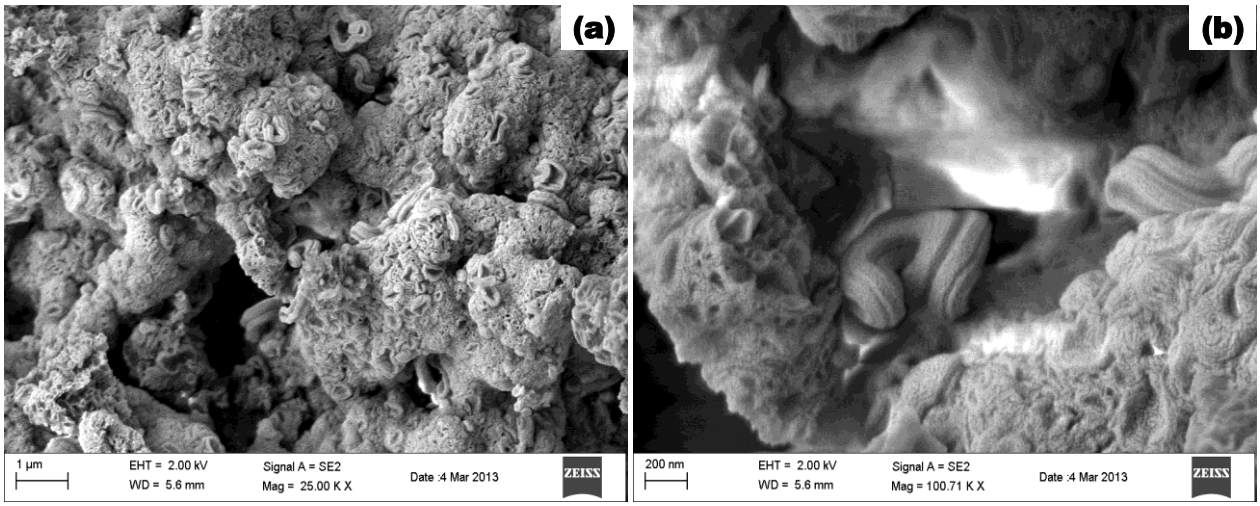

Figure 4. 6 SEM micrographs of SBA-15 at different magnifications.

4.1.2.3 Micrographic Analysis of SBA-15 Carbon Nanotube Composites

Micrographs of composites, **Figure 4.7** show thin film coatings with uniform and thicker layers of SBA-15 at 20 wt. % and 30 wt. % coatings (image b and c respectively) as opposed to aCNTs (image a). The measured thickness of SBA-15 was 3.90, 4.48 and 4.61 nm for 10, 20 and 30 wt. % SBA-CNT composites respectively. At 30 wt. % loading it was expected that the coating thickness would be significantly higher than the 20 wt. % coatings; however, the thickness measurements showed slight coating thickness increase for the 30SBA-CNT material. An average of 85 images was measured per sample with the image j software for the coating thickness measurements. In agreement with the morphological studies was the Raman spectrum analysis, which showed variations of the 20 wt. % coating as compared to other coatings.

This interesting observation on the 20 wt. % material could suggest that partial covering occurs at lower wt. % since lower amounts of silica is available; or perhaps, better coverage is achieved with increasing wt. % which allows the silica coating could grow along the CNT walls [10].

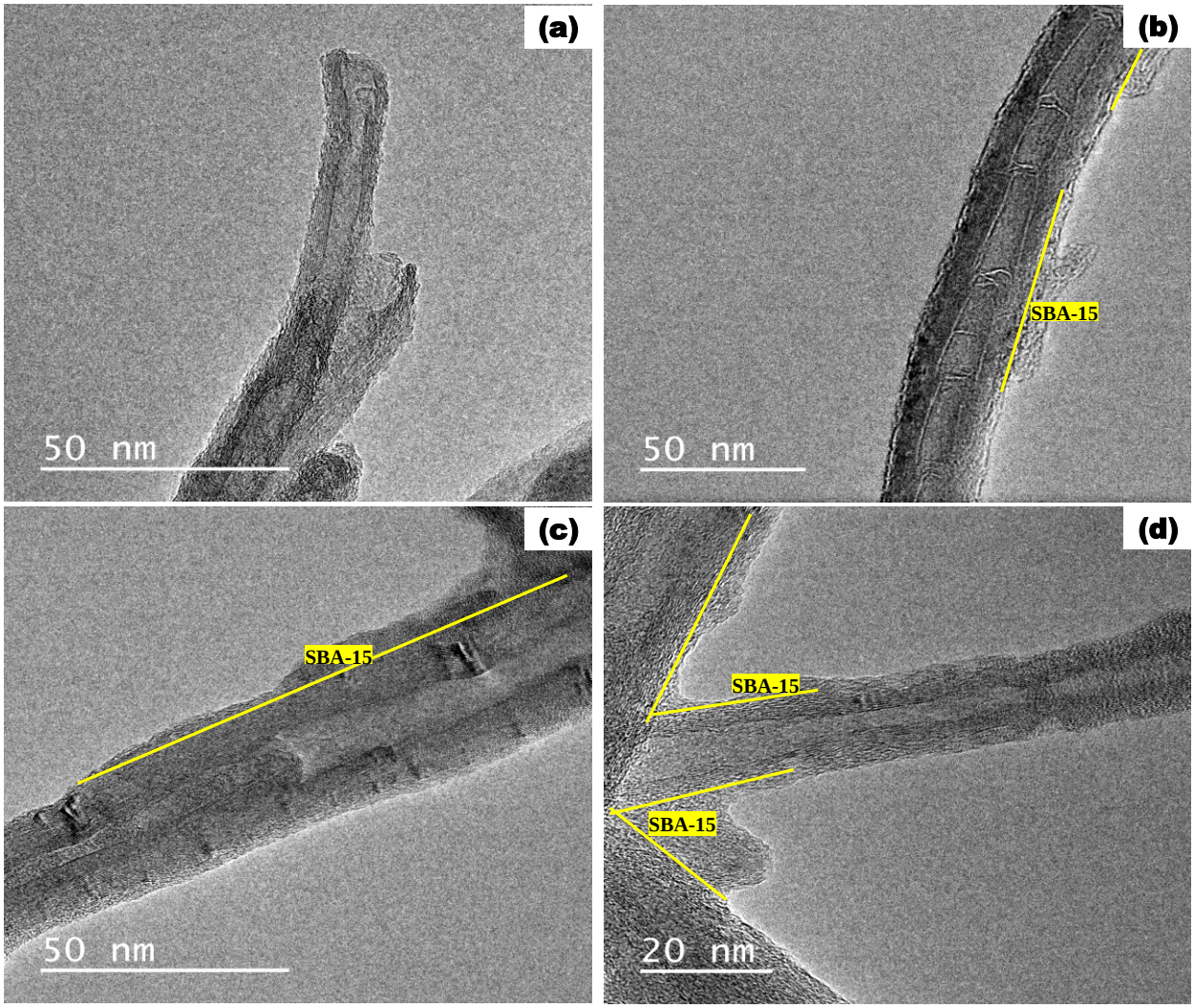

Figure 4. 7 HRTEM images of aCNTs (a) employed to prepare 10, 20 and 30 wt. % SBA-15 (b, c and d) respectively. The yellow line differentiates the silica coating from the aCNT wall in the respective composites.

SEM images **Figure 4.8** (**b, c and d**) suggest that the silica coated the CNTs (**image a**) through the exhibition of rough tube walls as compared to acid treated CNTs used to prepare the composites. It is worth noting that the 10 wt. % composite (image b) does not show the roughage on the tubes as clearly as the 20 and 30 wt. % composite. The nanotubes remain de-bundled even after SBA-15 coating.

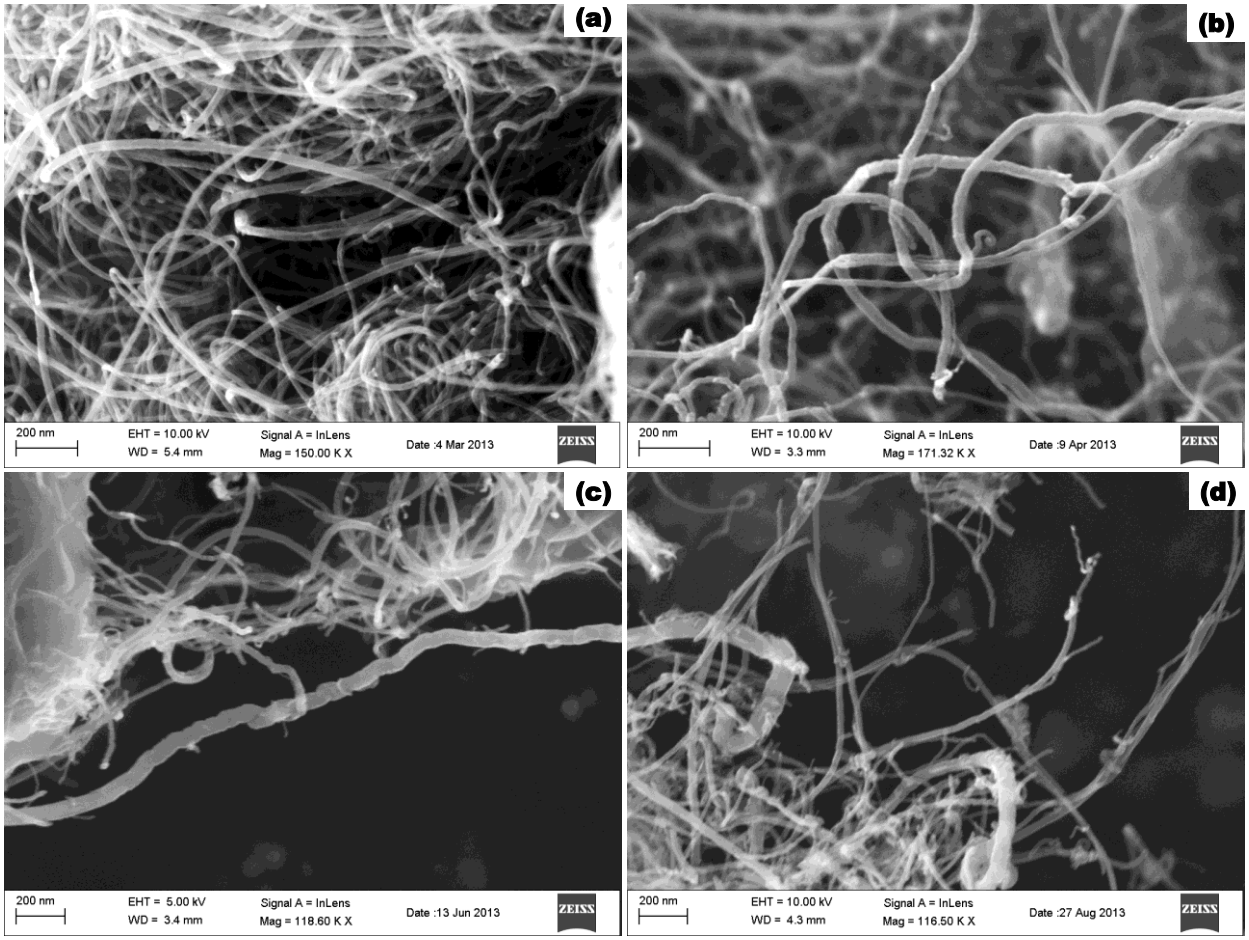

Figure 4. 8 SEM images of aCNTs, 10, 20 and 30 wt. % SBA-15 coated CNTs (a, b, c and d) respectively.

4.1.3 Thermo-gravimetric Analysis (TGA) Studies

TGA is a thermal characterization technique which studies the chemical and physical properties of materials as a function of increasing temperature using a programmed heating rate. Properties such as sorption, crystalline transition, decomposition, oxidative degradation and solid gas reactions can be studied through TGA methods [15].

4.1.3.1 Thermo-gravimetric analysis on Raw and Acid Treated Carbon Nanotubes

Thermograms presented in **Figure 4.9** show that the decomposition onset temperature for the acid treated CNTs is lower than that of raw CNTs. This could be as a result of aCNTs having functional groups which are prone to oxidation at low temperatures [16]. Raman analysis suggested that the aCNTs were more graphitic than the rCNTs, so it was expected that the aCNTs would be more thermally stable but the thermograms show otherwise. This observation suggests the presence of highly oxidative functionalities as a result of acid treatment, and in addition, the HRTEM analysis revealed significant tube openings on the CNTs which could also account for the lower onset oxidation temperature. From the decomposition of the rCNTs at ≈ 400 ˚C, the amount of impurities, either in the form of amorphous carbons or metal catalyst was relatively high, based on the residue of ≈ 7.1 wt. %.

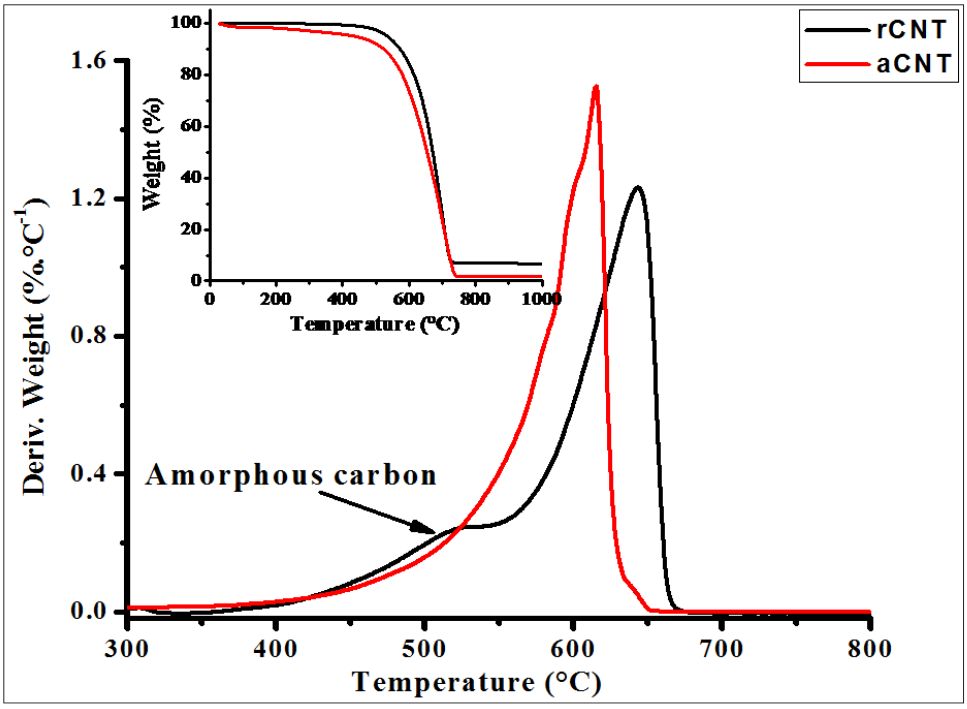

Figure 4. 9 Thermogram pattern of raw and acid treated CNTs, derivative weight pattern (insert).

Reports state that amorphous carbon decomposes at lower temperature (400 ˚C) than graphitic carbon (600 ˚C) [17]. Further analysis from the derivative weight graph showed that after purification there were reduced amounts of amorphous carbon since the shoulder like feature in the derivative weight curve for rCNTs decreased significantly. These results are in agreement with the Raman analysis and TEM analysis which both suggested the removal of amorphous carbons. Multiple oxidation peaks or shoulders are associated with the presence of organic species within the material of study. Thermal stability of materials were deduced from the oxidation temperatures, which are the highest peak position in the derivative weight versus temperature graph. Functionalizing the tubes shifted oxidation temperatures from 643 to 614 ˚C for rCNT and aCNTs respectively. Additionally the aCNTs depicted a narrower oxidation peak, which indicates high purity on the tubes, and a more uniform sample [18]. The decrease in residue in the acid treated CNTs (≈ 2.1 wt. %) as compared to raw CNTs (≈ 7.1 wt. %) also imply that the metal catalyst used during CNTs synthesis has been mostly eliminated.

4.1.3.2 Thermo-gravimetric analysis on SBA-15 coated Carbon Nanotubes

The decomposition behaviour of SBA-CNT composites (**Figure 4.10a**) show that as the SBA-15 content is increased from 10 to 30 wt. % the residual mass decreases as 95, 85 and 70 wt. % respectively. The decomposition temperature of CNTs increased upon introducing SBA-15. This suggested that silica improves the thermal stability of the CNTs.

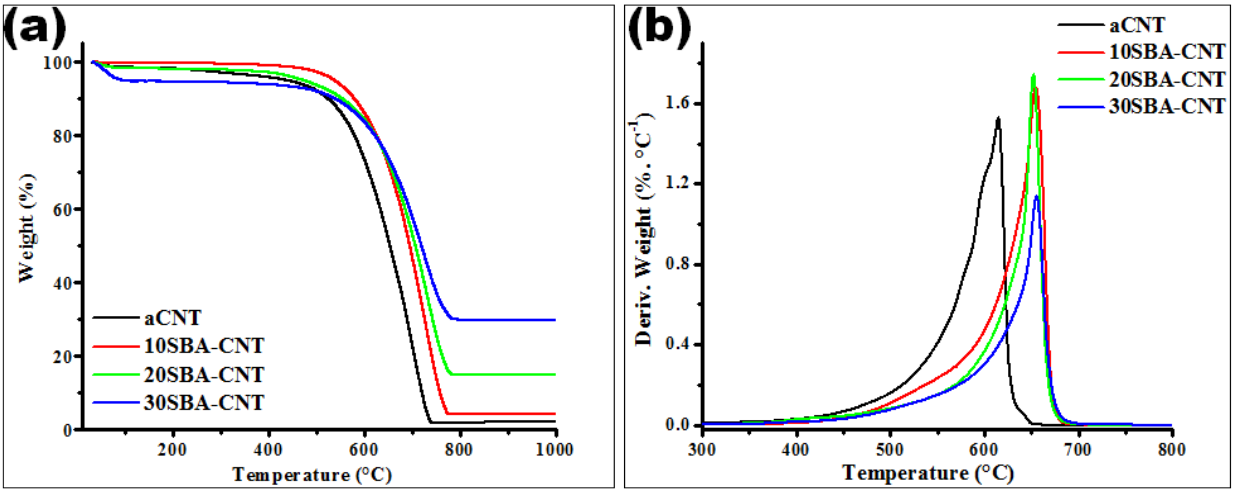

Figure 4. 10 Thermogram patterns of acid treated CNTs and SBA-15 coated CNTs (a), and derivative weight pattern of the respective materials (b).

The derivative weight patterns (**Figure 4.10b**) confirm that the stability of the composites is increased as the SiO_2 content is increased. This phenomenon was observed by Paula et al. [10] and they attributed the trend to the deposition of silica onto the graphitic sheets of the tubes. Analysis showed that the composite residues were approximately 5, 15 and 29 wt. % respectively for the 10, 20 and 30 wt. % SBA-CNT composites after decomposition. The residue can be various oxides corresponding mainly to SiO_2, since the aCNTs also had about ≈2 wt. % residue related to metal catalyst. The formation of silica was confirmed from the Raman spectra and morphological inspections, using electron microscopy, which depicted an increase in wall thickness of the tubes as SBA-15 coating was increased.

4.1.4 X-Ray Diffraction Pattern (XRD) Analysis

A wide range of solid materials can be described as crystalline. When x-rays interact with a crystalline substance, a diffraction pattern is produced. The x-ray diffraction pattern of a pure substance is like a fingerprint of the substance. Thus XRD is a useful non-destructive technique which can be used to identify and understand the crystalline properties of materials, i.e crystal size, crystal structure, phase, orientation and lattice parameters.

4.1.4.1 XRD Pattern Analysis on Raw and Acid treated Carbon Nanotubes

Acid treatment on CNTs did not have any severe effects on the crystallinity of the tubes as can be seen in **Figure 4.11** which depicts the XRD patterns of the raw and treated CNT structures. The characteristic peaks of CNTs appear at 26.00˚ and 43.40˚. The strong and sharp diffraction peak at 2θ = 25.70˚ is indexed as the (002) reflection of graphite [19].

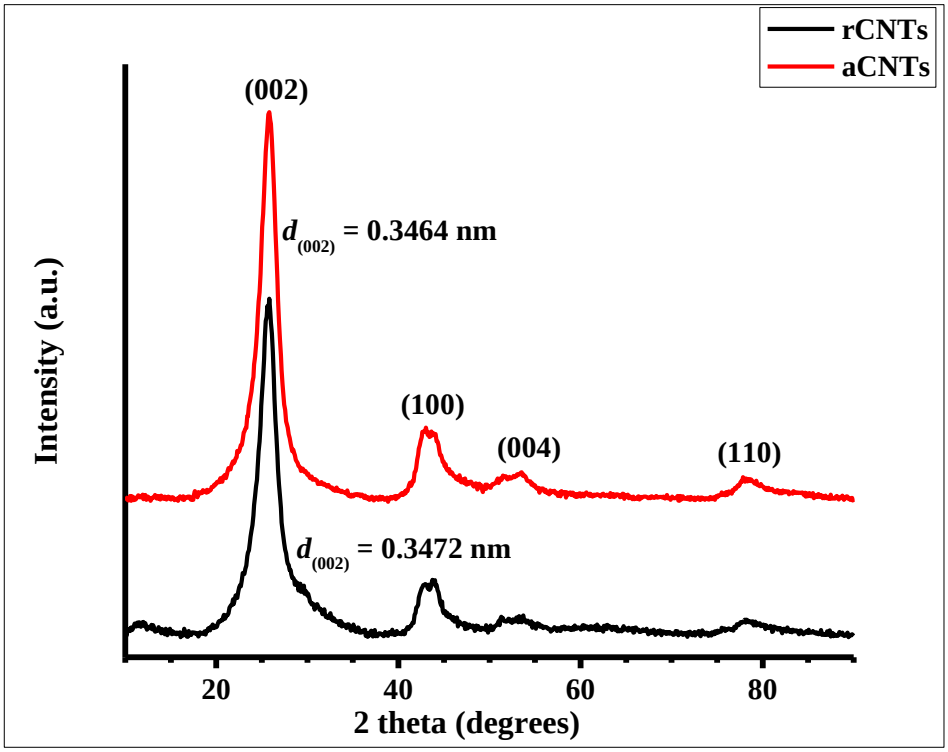

Figure 4. 11 XRD pattern of raw and acid treated CNTs.

The relative sharpness of the peak after acid treatment suggests that the graphitic structure was preserved. The peaks at 2θ = 43.90˚, 53.70˚ and 78.10˚ correspond to the (100), (004) and (110) reflection planes respectively. A slight variation between the interplanar spacing (*d*) was determined by using the Bragg's law ($n\lambda = 2d\sin\theta$) and the intense peak indexed at 2θ = 25.70˚. A slight variation in the interplanar spacing was observed between the materials. It has been reported that a decrease in the order of crystallinity in CNTs causes the XRD peaks to broaden and shift the (002) reflection plane towards lower angles [16].

Functionalizing the tubes narrowed the full width at half maximum (FWHM) from 2.57 to 2.44˚ (**Table 4.2**), a phenomenon that has been reported to occur if the amorphous carbons and residual catalysts have been removed and the functional groups have been introduced to the tube surface. The decrease in thermal stability of the aCNTs also confirmed the presence of functional groups on the tubes. The narrow XRD - FWHM of aCNT is in agreement with the Raman analysis which suggested that the aCNTs were more graphitic than the rCNTs.

Table 4. 2 Summary of raw and acid treated CNTs properties analyzed from the XRD pattern.

Support	2 theta (˚)	FWHM (˚)
rCNTs	25.72	2.57
aCNTs	25.66	2.44

4.1.4.2 XRD Pattern Analysis on SBA-15

The hexagonal arrangement of pores in SBA-15 was further confirmed by the sharp diffraction peaks in the low angle XRD pattern (**Figure 4.12**). The peaks at 2θ = 0.94˚, 1.62˚ and 1.85˚ are indexed to the (100), (110), and (200) planes, which indicate the 2D hexagonal symmetry of SBA-15 [14]. The wall thickness was calculated from the XRD pattern using the equation (Wt = $2d_{(100)}/3^{1/2}$ – pore diameter) to be 5.70 nm. This wall thickness deviates from that measured on the TEM micrographs (4.68 nm); probably because of errors involved during image analysis and measuring. However, the measured wall thickness value corresponds to reported values for SBA-15 [14]. Since SBA-15 is amorphous, the observed broad peak at 2θ = 24.00˚ was attributed to the amorphous SiO_2 character, in accordance with previous studies on TiO_2/SBA-15 composites [20, 21].

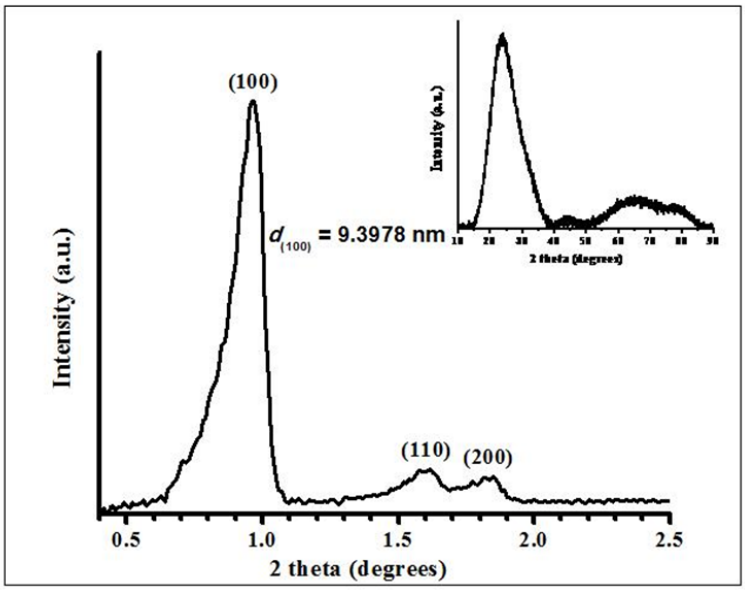

Figure 4. 12 Low and wide (insert) angle XRD pattern of SBA-15.

4.1.4.3 XRD Pattern Analysis on SBA-15 Carbon Nanotubes Composites

Upon introducing SBA-15 to the tube surface, the sharpness of the CNTs peaks in the XRD gradually declined as the silica content increased (**Figure 4.13**). Since the sol-gel method allowed for homogeneous coatings, the graphitic band of the tubes which is crystalline overlaps with the silica peak observed in the insert of **Figure 4.12**. Irrespective of the overlap, it remains evident that the reflection of the tubes in the 30 wt. % composite was most affected. This was attributed to the increased content of silica in the composite.

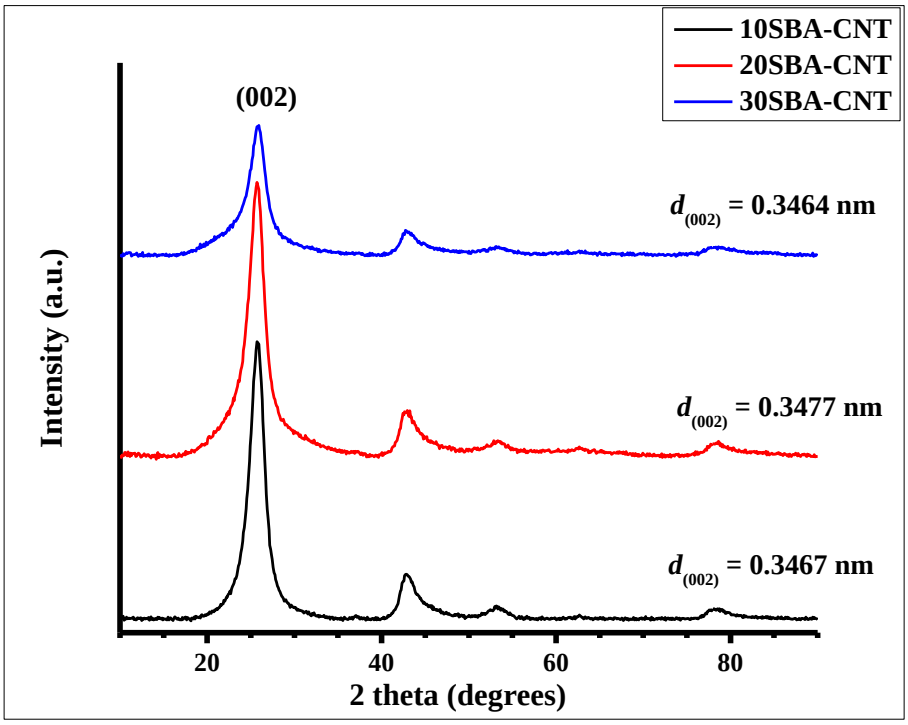

Figure 4. 13 XRD pattern of SBA-15 coated CNTs.

Furthermore, the FWHM of the peak at 2θ = 26.00˚ broadens at higher contents of SBA-15 (**Table 4.3**), this suggested that the order of crystallinity in CNTs was gradually being damaged as a result of interaction between silica and CNTs. The non-overlapping peak of CNTs at 2θ = 43.00˚ was also employed to monitor the effect of SBA-15 coating on CNTs and similar FWHM broadening trends were observed. In support of the deteriorating crystallinity of the tubes, the reflection planes (002) and (100) of CNTs were found to have shifted to higher angles as SBA-15 loadings were increased. This suggested that more disorder was introduced to the CNTs. The increasing disorder on the CNTs was also observed from the increasing Raman I_D/I_G ratio.

Table 4. 3 Summary of material properties analyzed from the XRD pattern.

Support	2 theta (˚)	FWHM (˚)	Interplanar spacing $d_{(100)}$
aCNTs	25.66	2.57	
	43.47	2.47	0.2082
10SBA-CNT	25.71	2.23	
	43.08	1.77	0.2100
20SBA-CNT	25.62	2.57	
	43.11	2.02	0.2098
30SBA-CNT	25.70	2.82	
	43.24	2.20	0.2092

4.1.5 Nitrogen (N_2) Sorption Studies

4.1.5.1 Nitrogen Sorption Studies on Raw and Acid Treated CNTs

Acid treatment of CNTs increased the surface area of the tubes by ≈ 9 m^2 g^{-1} (from 140.34 to 149.10 m^2 g^{-1}). The increase of the surface area was expected since the amorphous carbons have been eliminated while introducing various functional groups, and de-bundling the individual CNTs. The acid treatment also opened the tube ends of the CNTs (see figure) and exposed the inner surface area. **Figure 4.14** showed that the employed CNTs were type IV with H1 hysteresis loop, according to IUPAC classifications [22]. The insert in the figure shows that the pores of the tubes were in the range 20 - 50 nm, with an intense and narrow pore size distribution at approximately 0.2 nm. Such pore sizes, 20 – 50 nm, are characteristic of mesoporous materials, while pores below 2.0 nm would be classified as microporous [14]. Acid treated CNTs adsorbed more nitrogen and had pores distributed over long ranges, this observation can be a result of de-bundling the tubes and opening the tube ends during treatment, therefore, making inner cavities accessible for adsorption [23] and as a result, enhancing the textural parameters of the nanotubes.

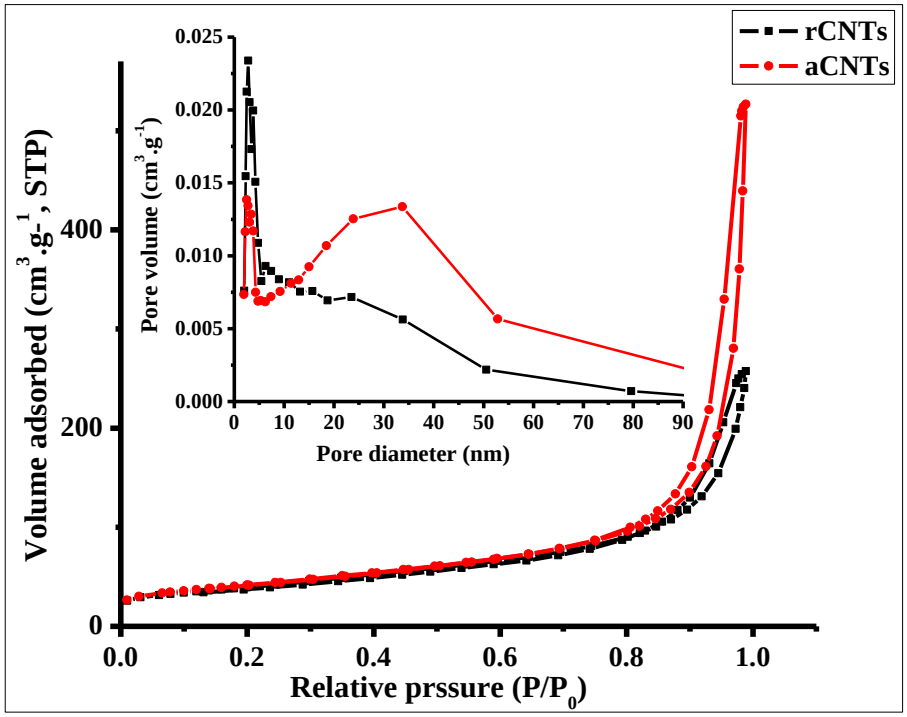

Figure 4. 14 Nitrogen adsorption-desorption isotherm and pore size distribution pattern (insert) of raw and acid treated CNTs.

4.1.5.2 Nitrogen Sorption Studies on SBA-15

Nitrogen sorption analysis on the SBA-15 (**Figure 4.15**) shows that the SBA-15 material has a type IV isotherm, which is associated with capillary condensation involved in the mesoporous material. The steep adsorption – desorption step indicate that the material has regular hexagonal mesopores with a narrow pore size distribution [21]. The hysteresis loop is a H2 type according to IUPAC classifications. The pore size distribution pattern (**Figure 4.15 insert**) confirms that the material possess a narrow pore distribution with pores centred at 4 nm, has a relatively high surface area of 661.59 m^2 g^{-1}, and an average pore diameter of 5.03 nm. The sorption in the hysteresis loops at high relative pressures $0.5 < P/P_0 < 1.0$ represent the spontaneous filling of the mesopores due to capillary condensation [20] and this is indicative of the presence of micropores and mesopores. Such great textural properties are reported to enhance the catalytic properties of SBA-15 through increased diffusion rates of target molecules and increased active sites [24].

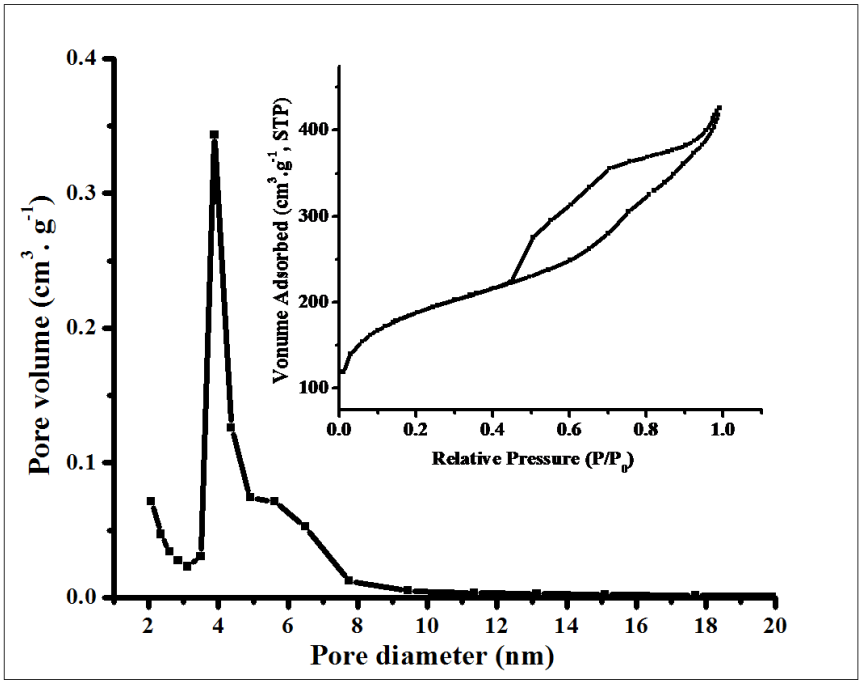

Figure 4. 15 Pore size distribution pattern and adsorption-desorption isotherm curve (insert) of SBA-15.

4.1.5.3 Nitrogen Sorption Studies on SBA-15 Carbon Nanotubes Composites

The surface area of the SBA-CNTs nano-composites increased upon coating with larger weight percentages of SBA-15 (**Table 4.4**). This is because SBA-15 has very high surface area ranging from 500 – 1000 m^2 g^{-1} [14], thus its presence on any structure should enhance the surface area to noticeable degrees. Pore volume increased as the coating weight was increased. This is again a result of the synergy between porous CNTs and SBA-15. Coating thickness was measured to be 3.90 nm, 4.48 nm and 4.31 nm respectively for 10 wt. % SBA-CNT, 20 wt. % SBA-CNT and 30 wt. % SBA-CNT from use of Image j software. The decreased coating thickness at 30 wt. % loading can be attributed to the coating of each CNT tube, or SBA-15 being loosely associated with the CNTs within the composite. The latter possibility requires investigations such as FTIR analysis for the SiO_2-C bond.

Table 4. 4 Textural parameters of materials obtained from N_2 sorption measurements at 77K.

Sample	S_{BET} (m^2 g^{-1})	V_{total} (cm^3 g^{-1})[a]	Average pd (nm)[b]	Coating thickness (nm)[c]
rCNT	140.34	0.34	11.72	no coating
aCNT	149.10	0.56	20.76	no coating
SBA-15	661.59	0.66	5.03	5.699[d]
10SBA-CNT	209.91	0.56	15.25	3.90
20SBA-CNT	256.59	0.69	16.02	4.48
30SBA-CNT	431.41	0.93	12.95	4.61

[a] Total pore volume adsorbed at a relative pressures for N_2 at -196 ˚C.
[b] Average pore diameter/size
[c] Measured from micrographs using image j software
[d] Wall thickness calculated from $Wt = 2d_{(100)}/3^{1/2} – pd$.

Nitrogen adsorption-desorption isotherms of the composites (**Figure 4.16**) show that the curves are typically type IV isotherms as classified by IUPAC [22, 25], and have H1 hysteresis loops which again are characteristic of mesoporous materials [26]. The composites show wider sorption of N_2; which is indicative of the preserved porosity and may be opening of the tube ends. The isotherms show high absorptions at relative pressures (P/P_0) up to 1.0, indicative of formation of large mesopores and micropores. It is interesting to note that the composite with 30 wt. % loadings absorbed at longer relative pressure ranges (0.6 - 1.0 nm) than other composites, and has a hysteresis loop which is associated with capillary condensation of gases within the mesopores.

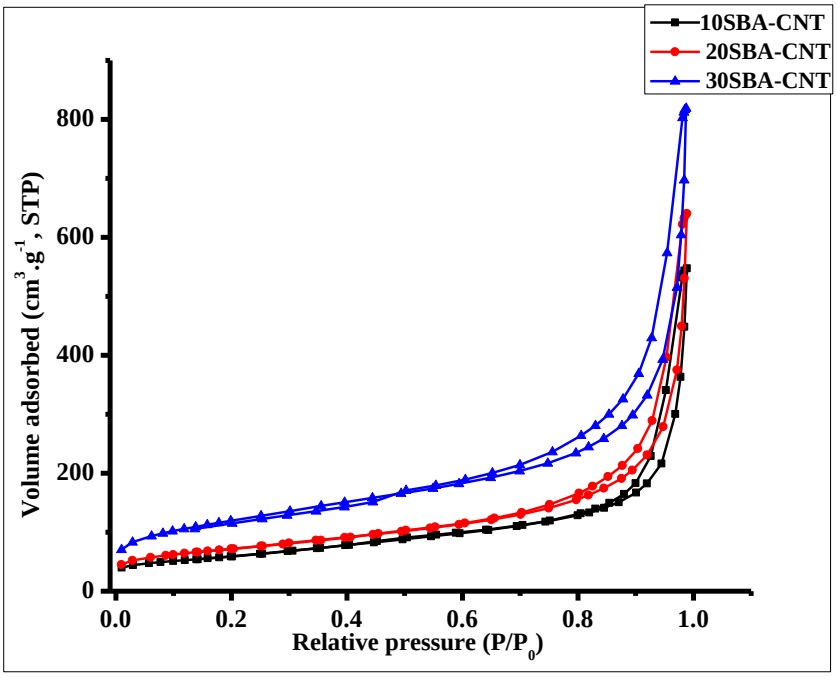

Figure 4. 16 Nitrogen adsorption-desorption isotherms of SBA-CNT composites.

The corresponding pore size distribution for the 30 wt. % SBA-CNT composite (**Figure 4.17**) show narrow and well defined mesopores centered at 4.8 nm. This is attributed to the SBA-15 since a peak at similar pore diameter sizes is identified in the SBA-15 pore size distribution pattern (**Figure 4.15**) and this narrow pore size in 30 wt. % SBA-CNT composite is reported to enhance photo-catalytic activity in materials [27]. The 10 and 20 wt. % SBA-CNT composites have two peaks at ≈ 2.6 and 3.5 nm, similar peaks were observed in aCNTs, and therefore the appearance of these peaks in the composites is associated with CNTs. Also of interest is the small hump between 6 and 11 nm in the 20 and 30 wt. % composites, this hump is attributed to the better de-bundling of the CNTs as the silica was increased which suggest that the coating methods was efficient.

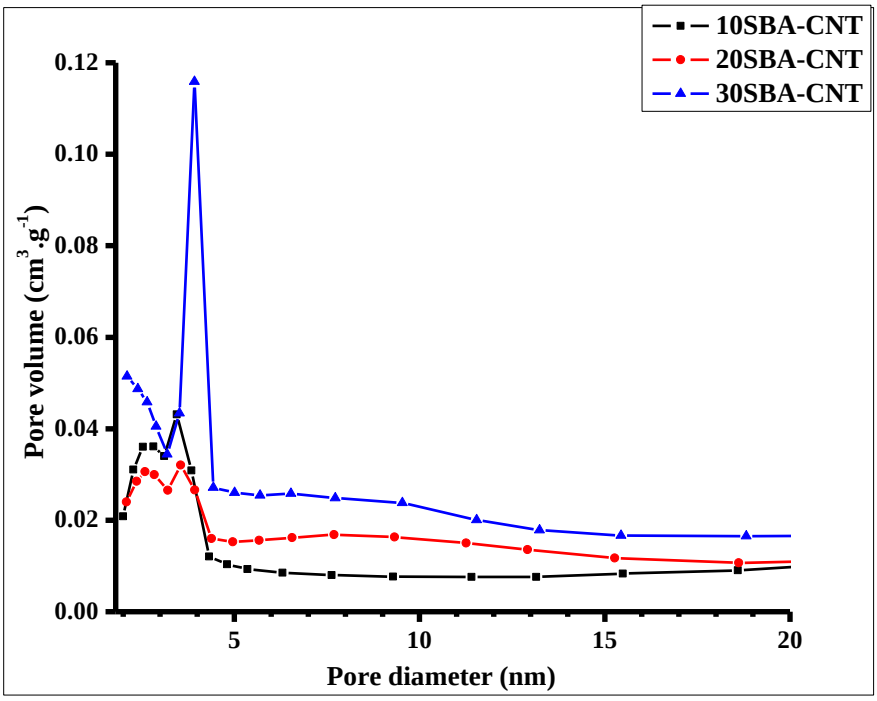

Figure 4. 17 Pore size distribution pattern of SBA-CNT composites.

Analysis on the various characterization techniques allowed us to identify the composite with more desirable physical and chemical properties. The 30 wt. % SBA-15 coated CNTs has uniform silica coating and enhanced properties such as specific surface area, pore volume and good thermal stability. Properties such as this are desirable in catalysis studies. The aCNTs, SBA-15 and 30 wt. % SBA-15/CNTs will be employed to host TiO_2 nano-particles, and determine which support has a better synergistic effect with the titania..

4.2 Properties of Synthesized TiO_2 Embedded on Different Mesoporous Supports at 10 wt. % TiO_2

This section describes the physical and chemical properties of the synthesized TiO_2 nano-particles and TiO_2 nano-composites. The materials presented in this section were prepared according to experimental methods described in section 3.3.3 to 3.3.6. An initial TiO_2 loading of 10 wt. % was chosen and employed to investigate the properties of TiO_2 with the supports. This loading was chosen as an initial loading because it would provide sufficient photo-catalytic material for testing and investigating the optimum catalyst support without significant waste of the catalyst precursor used to make the composites.

4.2.1 Electron Microscopy Investigations of Catalysts

4.2.1.1 HRTEM and SEM Analysis on Unsupported TiO_2

The HRTEM **Figure 4.18(a)** shows well-defined lattice fringes of TiO_2 with an interplanar d-spacing of 0.35 nm. HRTEM interplanar spacing measurements were in agreement with the calculated values for the interplanar spacing using Bragg's law and 2θ values from the JCPDS pattern, reference card number 00-021-1272.

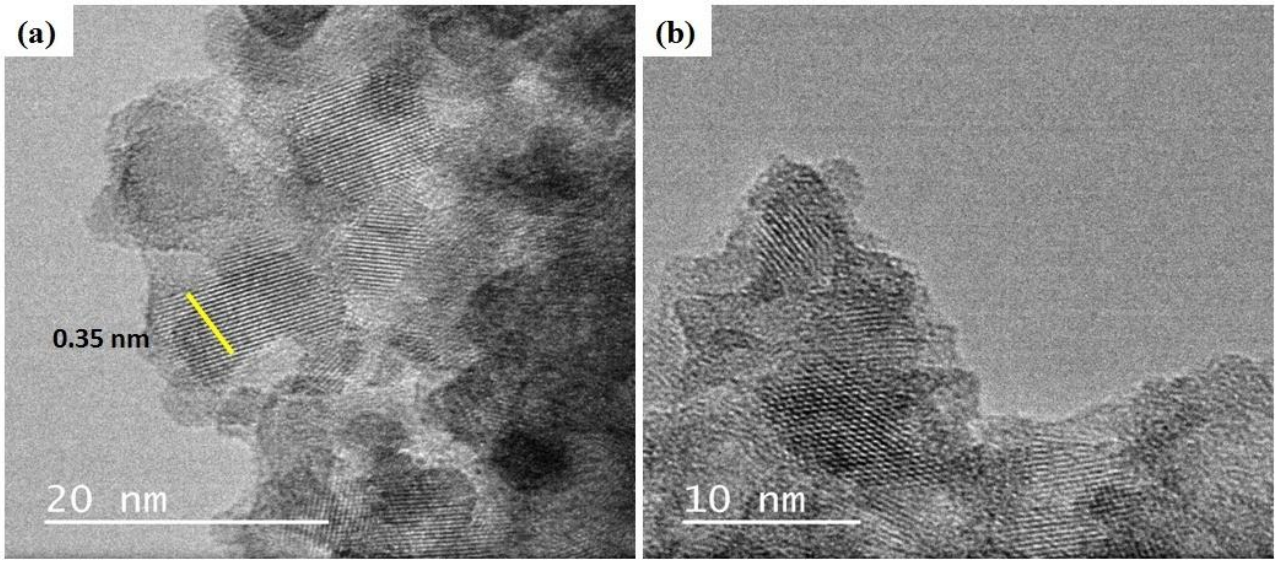

Figure 4. 18 HRTEM microcraphs of mesoporous TiO_2 nano-particles with measured interplanar d-spacing of 0.35 nm (a, yellow line) and consistent lattice fringes at scale bar of 10 nm (b).

The SEM images (**Figure 4.19**) show the agglomerated particles, with a spherical shape. The porosity of the particles is not resolved under SEM analysis, while irregular particle sizes and shapes are observed. The micrographs also show interparticle voids which are typical for loose particle aggregates [28].

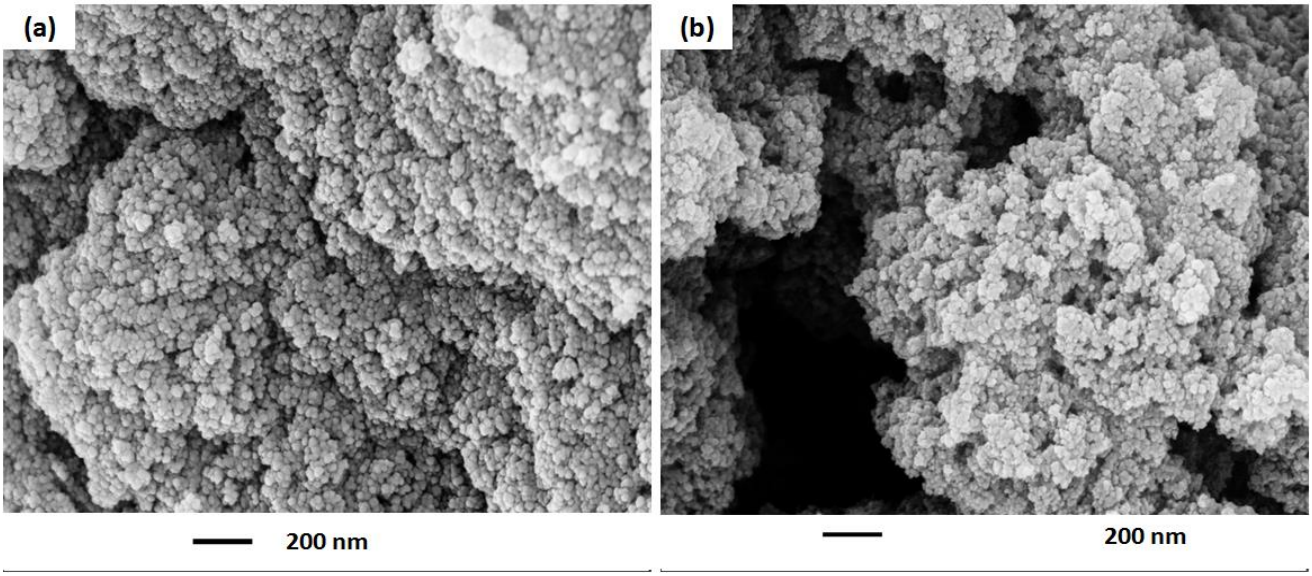

Figure 4. 19 SEM micrographs of mesoporous TiO_2 nano-particles.

4.2.1.2 HRTEM and TEM Analysis on TiO_2 Nano-Composites

Figure 4.20 (a) depicts the morphology of the 10 wt. % TiO_2/SBA-15 composite with well dispersed titania particles on the SBA-15 surface. The titania particles on SBA-15 are well dispersed small particles. Crystal size of TiO_2 as estimated by the Scherrer equation was 5.71 nm and it reduced to 4.57 nm when similar calculations were done on the SBA-15 titania composites. The incorporation of TiO_2 on the surface, rather than in the pores of SBA-15 could be a result of the small pore diameter 5.03 nm of the SBA-15 support. Similar morphological studies have been reported for TiO_2/SBA-15 composites [29].

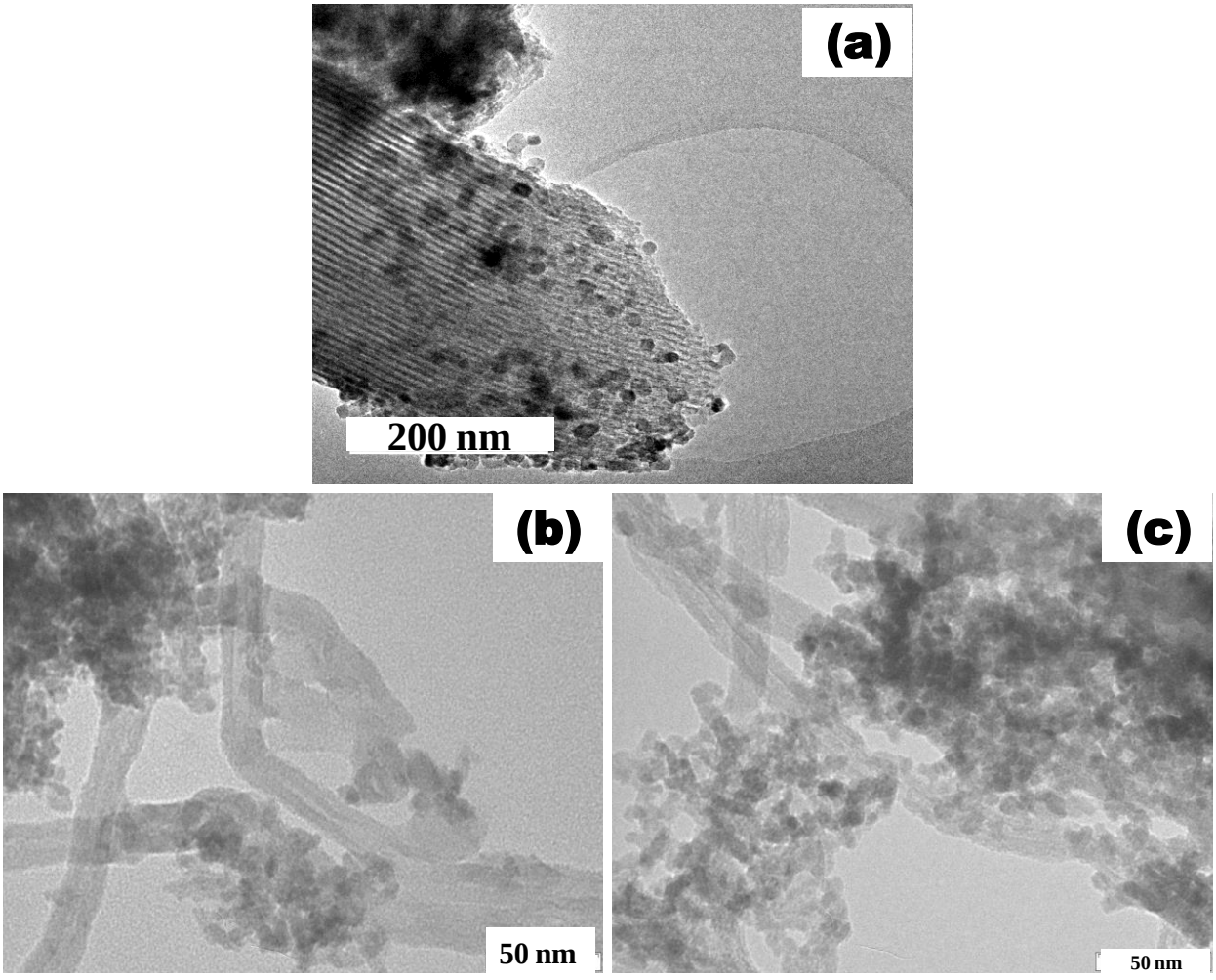

Figure 4. 20 TEM micrographs of TiO_2/SBA-15 (a), TiO_2/CNTs (b) and TiO_2/SBA-CNTs (c) nano-composites.

Figure 4.20 (b) show small agglomerates of titania particles on the acid treated nanotubes. The observed morphology could have been facilitated by the functional groups along the CNT walls. The SBA-15 coated CNTs show (**Figure 4.20 c**) distinct agglomeration of the titania particles. The anatase particles are more concentrated on the silica coated nanotubes than on the uncoated tubes as depicted. This can be attributed to the strong interaction of titania precursor with silica species on the nanotubes wall, which tends to attract the titania to the tube surface that has high concentrations of silica.

4.2.2 XRD Analysis of Catalysts

4.2.2.1 XRD Analysis on Unsupported TiO_2

XRD analysis was conducted to investigate the crystallinity of the sol-gel TiO_2 and corresponding materials. As can be seen in **Figure 4.21** the synthesized mesoporous titania resembles the pure anatase phase TiO_2 with no evidence of the dominant rutile peak that would appear at $2\theta = 27.40^{\circ}$ corresponding to the (110) reflection. Furthermore, no observations were made for the characteristic rutile reflections which appear as sharp and strong peaks at $2\theta = 54/56^{\circ}$. The anatase phase results from the maintenance of low temperature calcinations. The titania crystalline size of the synthesized catalyst was determined from the FWHM of the (101) reflection peak at 25.31°, using the Scherrer equation, and was found to be 5.71 nm. The Scherrer equation suggests an inverse proportionality between the crystal size (d) and FWHM (β). Also a decrease in the 2θ degree value is associated with an increase in crystallinity.

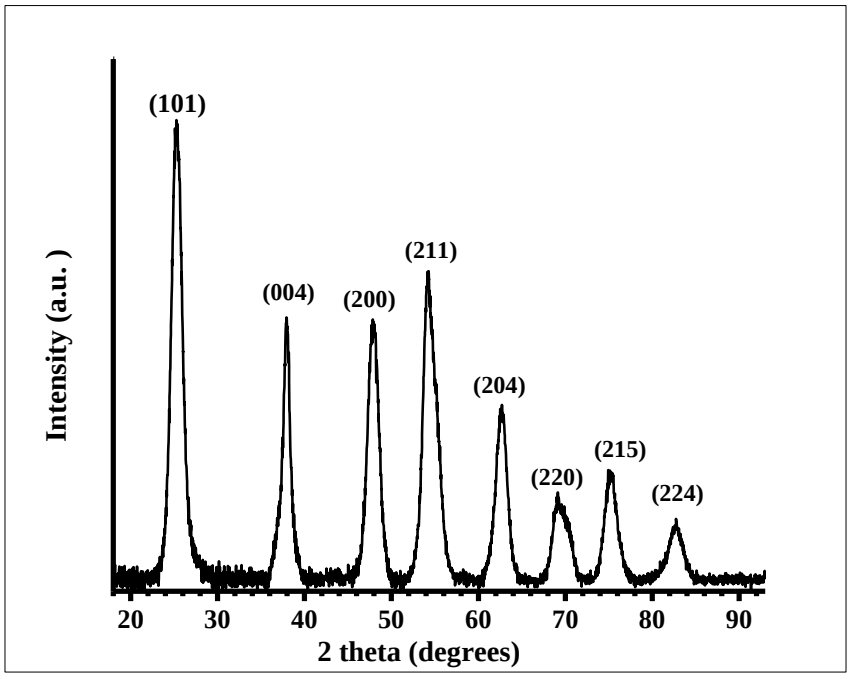

Figure 4. 21 XRD pattern of TiO_2 nano-particles.

4.2.2.2 XRD Analysis of 10 wt. % TiO_2 Nano-Particles on SBA-15

Incorporation of the titania particles onto SBA-15 could be seen to slightly inhibit the growth of the crystals as can be deduced from the small titania crystallite sizes (**Table 4.5**). Similar behavior of TiO_2 in SBA-15 has been reported by Lachheb et al. [30].

Table 4. 5 Properties of 10 wt. % TiO_2 catalyst on supports according to XRD pattern analysis using the (101) reflection peak of anatase TiO_2.

Catalyst	2 Theta (degrees)	FWHM (˚)	Crystal size (nm)
TiO_2	25.31	1.43	5.71
TiO_2/SBA-15	25.80	1.78	4.57
TiO_2/CNT	25.73	1.92	4.25
TiO_2/SBA-CNT	25.57	1.93	4.22

Figure 4.22 depicts the low angle diffraction pattern of SBA-15 and TiO_2/SBA-15 composite. The long range order of pores in SBA-15 was preserved as indicated by the appearance of peaks at low angles. However, incorporation of TiO_2 brought about a shift in the 2θ˚ value of SBA-15, indicating a change in the SBA-15 structure (**Table 4.5**). Shift in the low angle XRD peaks suggest the pores are smaller in the TiO_2/SBA-15 when compared to SBA-15 itself. D-values also show that the distance from the pore centre – centre has decreased, this can only happen if the wall thickness itself has increased, thus suggesting that some TiO_2 is within the pores of SBA-15. TiO_2 particles are thought to be in the pores and not only on the SBA-15 surface because of the shift in the (100) reflection from 0.9 2θ˚ with SBA-15 support alone, to 1.2 2θ˚ with the TiO_2/SBA-15 composite, the decreased d-values for this shift correspond to the distance from the pore centre – centre which suggests that the pore sizes and wall thickness have changed when comparing SBA-15 and TiO_2/SBA-15. Diffraction of the TiO_2/SBA-15 composite at low angle supports the analysis from morphological studies which suggested that the uniform, ordered mesopores of SBA-15 where preserved during incorporation of TiO_2 nano-particles and introducing TiO_2 did not alter the regular, long range ordered pore structure of SBA-15.

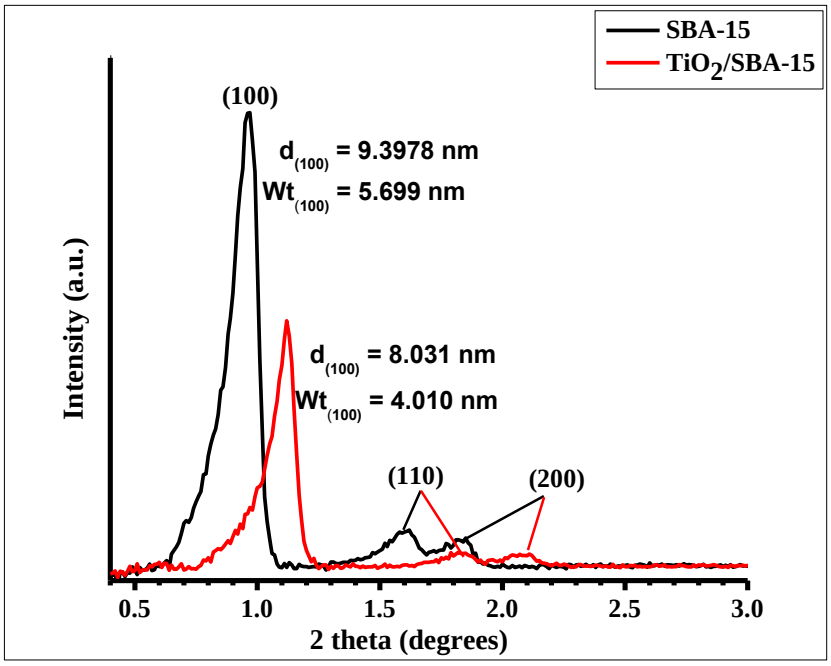

Figure 4. 22 Low angle XRD pattern of SBA-15 and 10 wt. % TiO_2/SBA-15 nano-composite, *Wt* denotes wall thickness.

4.2.2.3 XRD Analysis of 10 wt. % TiO_2 Nano Composite

All catalyst composites had peaks that were similar to those of anatase phase titiania. The appearance of a peak in the composites at 2θ = 42.88˚ did not correspond to any phase found in anatase, rutile nor brookite phase TiO_2. However, the peak was at a similar position as the (100) reflection plane of CNTs (**Figure 4.23**). This confirms that the crystallinity of the CNTs was maintained during the chemical and thermal treatments involved in the synthesis of the composites. The dominant peak of CNTs at 2θ = 25.72˚ could not be identified in the composites containing CNTs. It was no surprise since the dominant peak of the anatase titania also appears around the same position, therefore the peaks overlapped. A phenomena repetitively observed in studies relating to TiO_2/CNTs [31, 32]. TiO_2/SBA-15 composite showed small low intensity diffractions of the anatase peaks, this suggests that the TiO_2 particles were well dispersed on the SBA-15, this was in agreement with the low angle XRD analysis of the composite and the electron microscopy analysis.

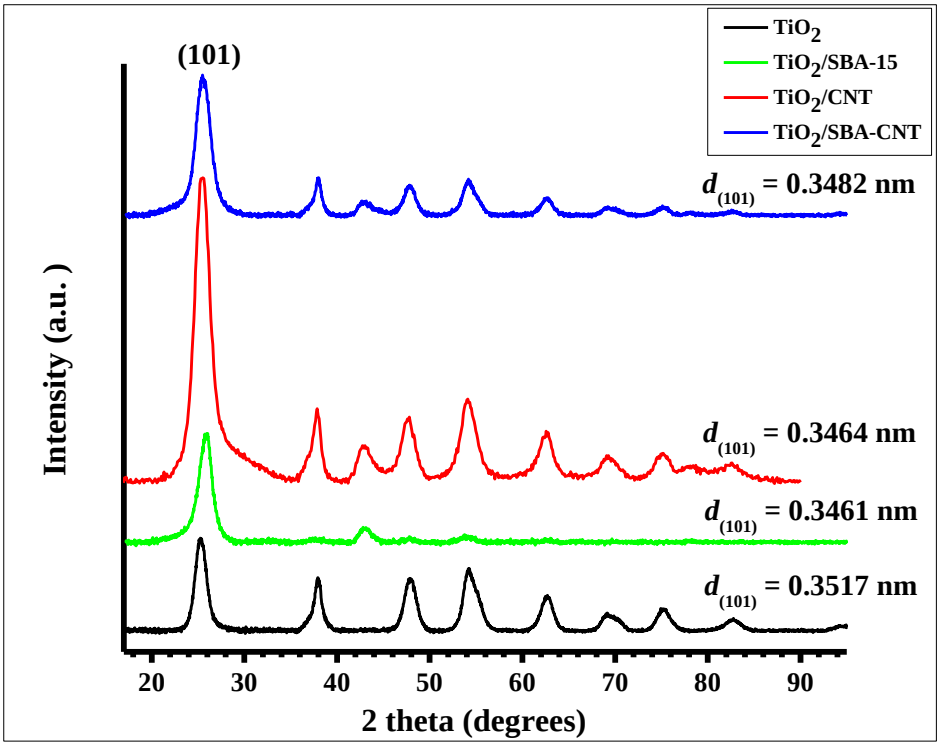

Figure 4. 23 XRD pattern of 10 wt. % TiO_2 nano-particles on SBA-15, CNTs and SBA-CNT composites.

Analysis of the XRD patterns using the overlapping ($2\theta = 26.00^{\circ}$) peak showed slight broadening of the anatase phase TiO_2 particles in the 10 wt. % TiO_2 composites when compared to the unsupported TiO_2. Since, in the composites, the TiO_2 (101) reflection peak of anatase overlapped with the (002) reflection peak of the CNTs and the amorphous peak of SBA-15, further analysis where carried out using the peak at $2\theta = 54.00^{\circ}$, assigned to the (211) reflection plane of anatase and similar trends of broadening when examining the FWHM and reducing titania crystal size were observed. Broad peaks and a shift of peaks to high angles for TiO_2 is associated with a decrease in crystallinity of the particles [16]. An overall effect of the support frameworks on titania particles was the restriction of the TiO_2 nano-particles growth as deduced from the small crystal size of TiO_2 when in the composites. This effect is desirable in catalysis studies since small crystals have high surface areas [33].

Table 4. 6 Properties of 10 wt. % TiO_2 catalyst on supports according to XRD pattern analysis using the (211) reflection peak of anatase TiO_2.

Catalyst	2 Theta (degrees)	FWHM (°)	Crystal size (nm)
TiO_2	54.43	1.91	4.69
TiO_2/SBA-15	54.04	1.97	4.53
TiO_2/CNT	54.18	1.99	4.48
TiO_2/SBA-CNT	54.30	1.84	4.86

4.2.3 Raman Spectroscopy of Unsupported TiO_2 and 10 wt. % TiO_2 Catalyst

The Raman spectra (**Figure 4.24**) depict vibrational bands at 400, 521 and 644 cm^{-1} which correspond to the anatase modes of B_{1g}; A_{1g} overlapping with B_{1g}; and E_g symmetry respectively. These modes are associated with anatase phase titania [20] and the analysis is in agreement with the identified phase from the XRD pattern.

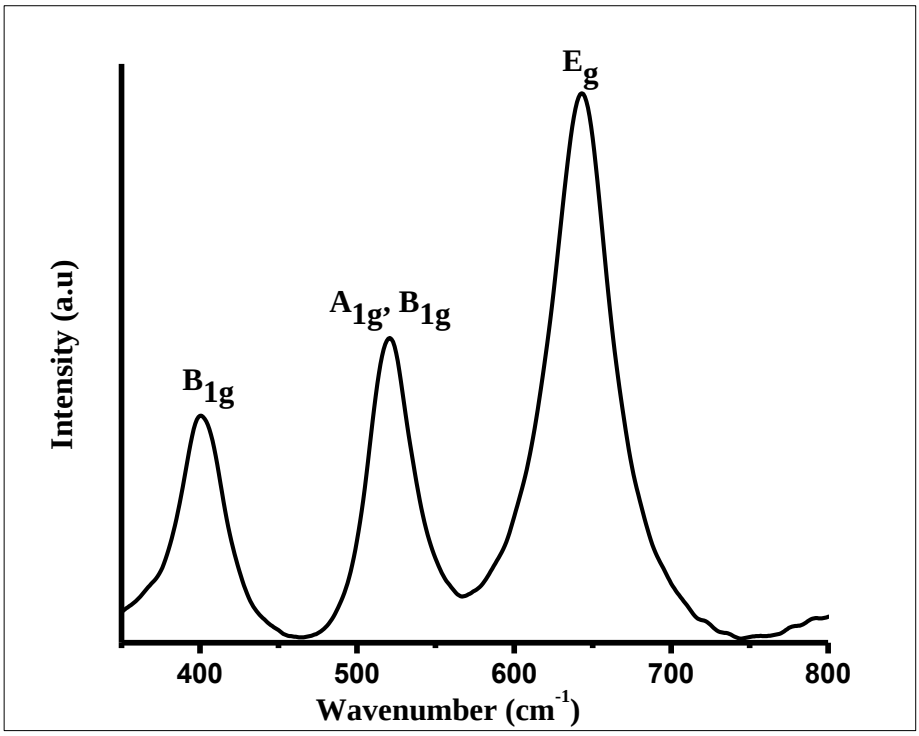

Figure 4. 24 Raman spectra of TiO_2 nano-particles.

None of the characteristic titania Raman spectroscopic bands were identified in the various composites (**Figure 4.25**). Perhaps due to the limited amount of titania incorporated onto the supports. The CNTs containing composites depicts the well-defined D and G bands of the nanotubes at ≈ 1350 and 1600 cm $^{-1}$ respectively. The titania phase within the composites was expected to be anatase, since, introducing SBA-15 and CNTs restricts phase transformation from anatase to rutile form through interaction that takes place between the species that stop the diffusion and nucleation processes [20].

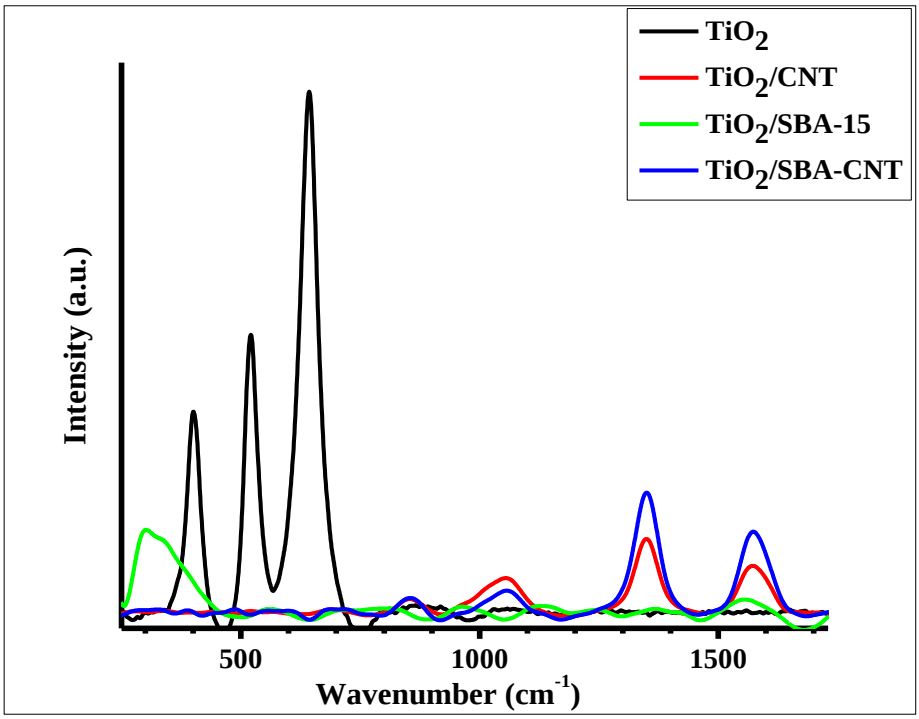

Figure 4. 25 Raman spectra of 10 wt. % TiO_2 on different supports.

4.2.4 Nitrogen Sorption Studies of Unsupported TiO_2 and 10 wt. % TiO_2 Catalysts

The sol-gel synthesized TiO_2 had a type IV isotherm with H2 hysteresis loop and wide adsorption - desorption at relative pressure of 0.4 - 1.0 (**Figure 4.26**). The isotherm and hysteresis loop confirmed the material to be mesoporous. Nitrogen sorption occurring at high relative pressures was indicative of materials with uniform pore arrays. The titania catalyst had an average pore size distribution of 5.2 nm and a specific surface area of 207.75 m^2 g^{-1}.

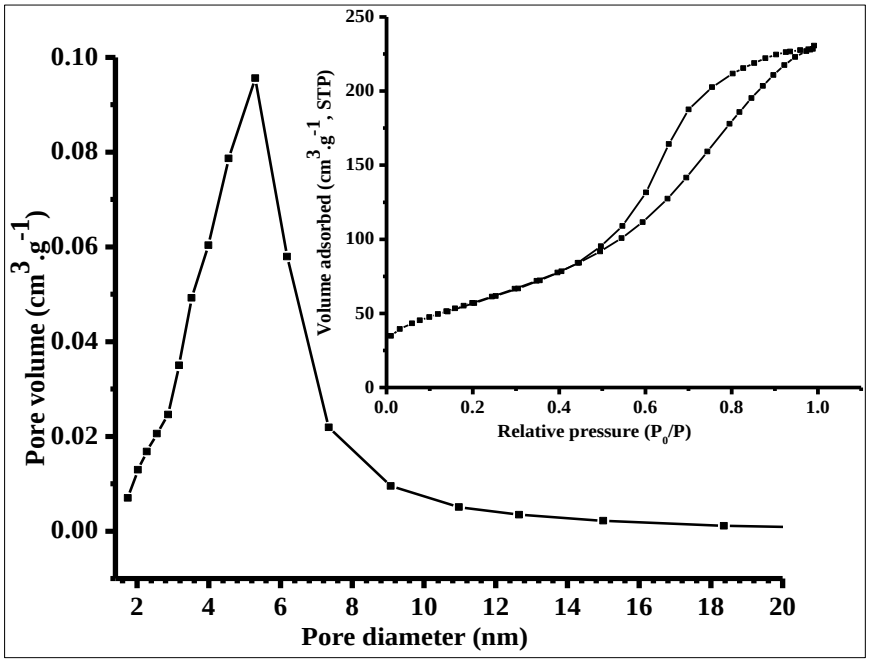

Figure 4. 26 Pore size distribution and nitrogen sorption isotherm (insert) of TiO_2.

The specific surface area of the TiO_2 increased when it was supported on the different materials as opposed to the unsupported TiO_2 nano-particles (**Table 4.7**).

Table 4. 7 Textural parameters of TiO_2 and 10 wt. % TiO_2 nano-composites according to N_2 sorption studies.

Parameter (Units)	**Catalyst Composites**			
	TiO_2	TiO_2/CNT	TiO_2/SBA-15	TiO_2/30SBA-CNT
S_{BET} (m^2 g^{-1})	207.75	241.28	214.00	301.35
Pore vol. (cm^3 g^{-1})	0.35	0.70	0.43	0.89
Pore diameter (nm)	5.10	15.65	5.73	12.56
TiO_2 content (wt. %)[a]	100	14.78	6.48	12.80

[a] Metal content calculated from Inductively Coupled Plasma-Optical Emission Spectroscopy analysis.

There were slight variations of the titanium dioxide content in the composites according to ICP-OES analysis. The TiO_2/SBA-15 composite showed the smallest contents of TiO_2, probably as a result of digestion methods which were not successful in digesting the TiO_2 particles deposited

inside the pores of SBA-15. The low content of TiO_2 in the SBA-15 composite imply that most of the titania that was digested was on the surface of the silica, and these results supports the XRD analysis which suggested that there were some TiO_2 particles deposited into the pores of SBA-15 since the same digestion method on CNT and SBA15/CNT supports provide values closer to the weight loadings expected. Supporting the titania catalyst on various supports did not compromise the meso-porosity of the materials. Although the titania particles on various supports had the same hysteresis loop and pore size distribution values similar to the respective support (**Figure 4.27a and b**).

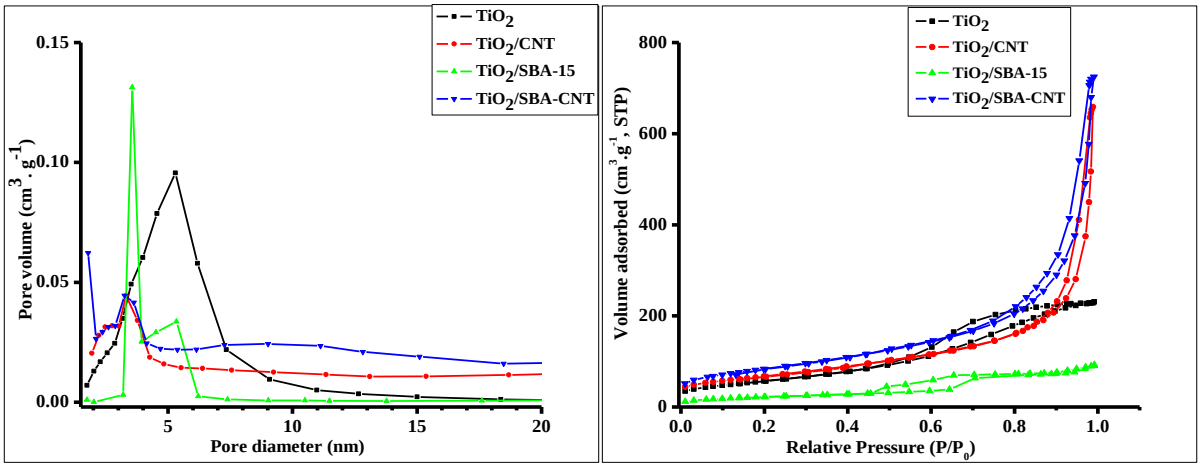

Figure 4. 27 Pore size distribution pattern (a) and sorption isotherms (b) of TiO_2 and 10wt. % TiO_2 nano-composites.

4.2.5 Optical Studies and Photoluminescence Studies on TiO_2 and TiO_2 Nano-Composites

Part of the various hindering factors regarding the activity of TiO_2 in photo activity applications is their wide band gap energy which can be activated by ultra-violet (UV) irradiation, and UV is only a small fraction of the solar energy that reaches the surface of the earth [34]. Reducing the band gap energy has been widely reported to yield positive results and increase catalytic performance of catalysts. **Figure 4.28a** is a representation of the optical responses of employed materials.

Degussa P25 was investigated in these experiments as a reference commercial catalyst to compare the set of prepared materials against. The extrapolated 3.29 eV band gap energy (**Figure 28b**) of Degussa P25 was in agreement with literature reports [45]. The synthesized anatase TiO_2 had decreased band gap energy of 3.1 eV and the other supported titania materials showed red shifts on CNT containing composites. The red shift indicate decrease in band gap energy and this was due to the unique manner in which CNTs can absorb visible, and other, parts of the electromagnetic spectrum. The band gap energy of composites containing CNTs reduced to 3.20 (TiO_2/CNT) and 3.15 eV (TiO_2/SBA-CNT) compared to SBA-15 supported TiO_2 (3.33 eV). The observed decrease of band gap energies brought on by CNTs in titania materials is in agreement with observations by Xu et al [35].

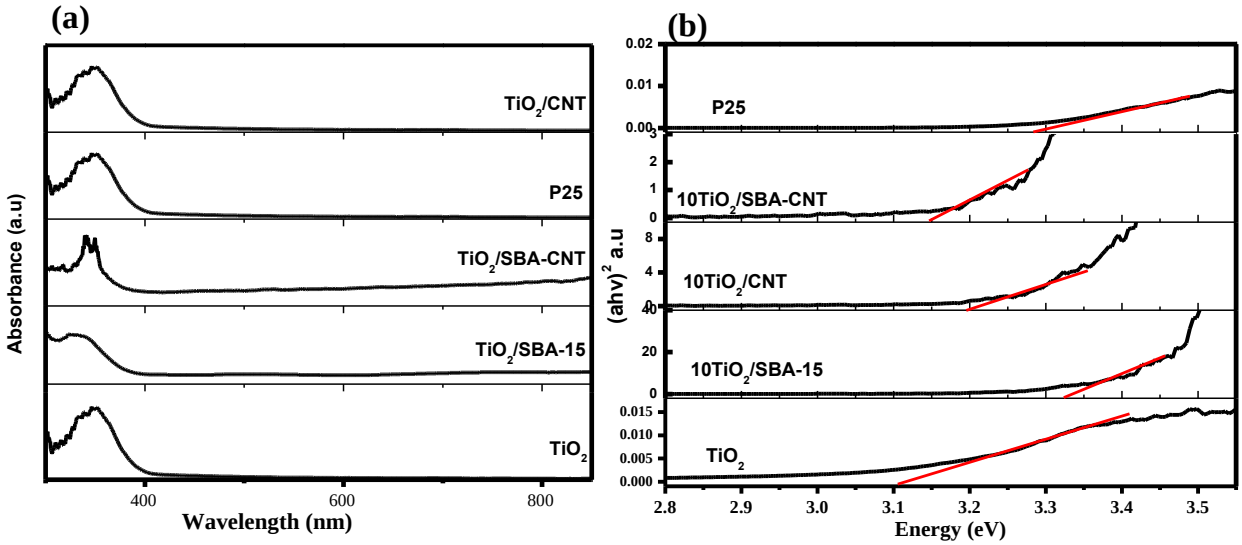

Figure 4. 28 UV-Vis diffuse reflectance measurements (a) and Kubelka Munk plots (b).

Photoluminescence (PL) studies have been employed to determine the electron-hole recombination rate. PL spectroscopy is considered to be a highly sensitive tool to study the photo-physics of the photo-generated species [36]. PL spectra results when excited electrons and holes recombine to their ground states and the intensity of peaks for materials at different wavelengths is indicative of the rate of recombination, for instance, when the peak intensity of the PL is low, then the recombination rate of electrons and holes is slow – a trait desirable in efficient photo-catalytic materials and applications [37].

Figure 4.29 exhibits PL profiles of 10 wt. % TiO_2 composites with peaks at 422, 461, 484, 530 nm for the unsupported TiO_2 and TiO_2/SBA-15 catalysts respectively. The presence of this peaks suggest that the recombination of electrons in this materials is fast. An emission band at 420 nm is attributed to shallow traps emission [38], while a common phenomena is that recombination of mobile electrons with trapped holes results in the emission of peaks at ≈530 nm, while recombination of trapped electrons with valence band holes leads to a broader PL spectrum with a peak at ≈600 nm [39]. The absence of peaks in the TiO_2/CNT and TiO_2/SBA-CNT composites suggest that the rate of electron – hole recombination is very slow. The recombination rate has been slowed by the presence of CNTs in the catalyst, because of the 1D structure of the tubes which make them prone to electron conduction with no resistance [40, 41] and in turn allow for generated electrons in TiO_2 to be easily transferred to the CNTs [6].

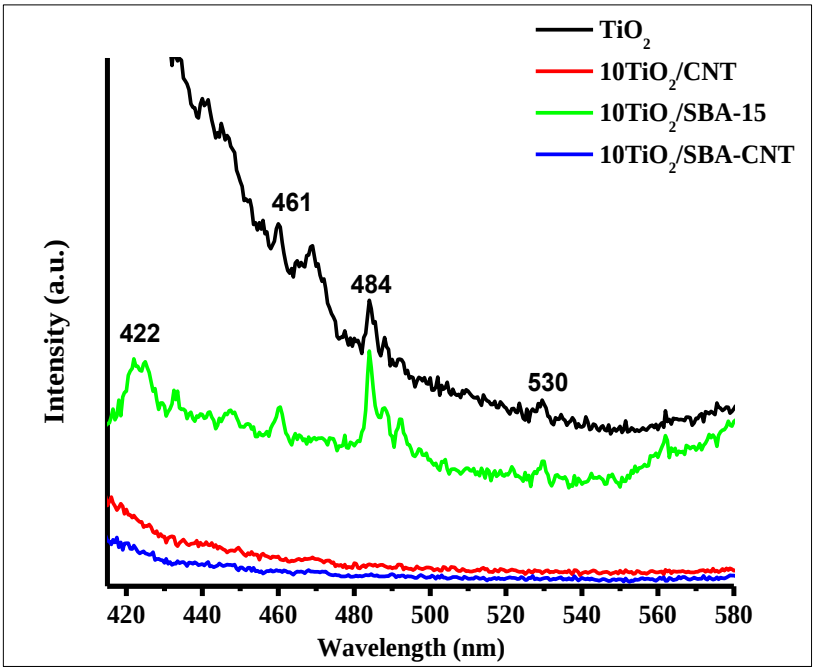

Figure 4. 29 Photoluminescence spectra of TiO_2 nano-particles and 10 wt. % TiO_2 on nano-composites. The spectra were captured at irradiation wavelength of 390 nm, excitation slit 5.0 nm, emission slit 0.0 nm and scan speed 120 nm. min^{-1}.

4.3 Properties of Different TiO_2 Nano-Particles Contents on 30 wt. % SBA-15 Coated CNTs

This section describes the physical and chemical properties of different TiO_2 loadings on SBA-CNT composite, which is an optimum catalyst support. The results presented in this section are based on the materials prepared in experimental section 3.3.6. The high surface area, high crystallinity of TiO_2, small band gap energy and slow electron-hole recombination rate of these composite make it a more attractive catalyst for further investigations amongst the studied catalyst supports **(section 4.2)**. Additionally the TiO_2/SBA-CNT catalyst composite showed enhanced photo-catalytic properties as will be discussed in **Chapter 5**. TiO_2 properties are monitored on the SBA-CNT framework at 5, 10 and 20 wt. % TiO_2 concentrations.

4.3.1 Morphological Studies on 5, 10 and 20 wt. % TiO_2 Nano-Particles on 30 wt. % SBA-CNT composite

Figure 4.30 presents the SEM micrographs which show that the presence of CNTs reduce the agglomeration of TiO_2 nano particles. This separation effect of CNTs has been observed by Wang et al. [42]. Chena et al. [31] reported that at 85 and 95 wt. % TiO_2/MWCNTs composites, titania particles where agglomerating and forming various sizes of particles that were packed together. In **Figure 4.30(d)**, 20 wt. % TiO_2/SBA-CNT composite depicts few agglomerates of TiO_2 particle, this could be observed at such low weight percentages perhaps because of the silica surface groups.

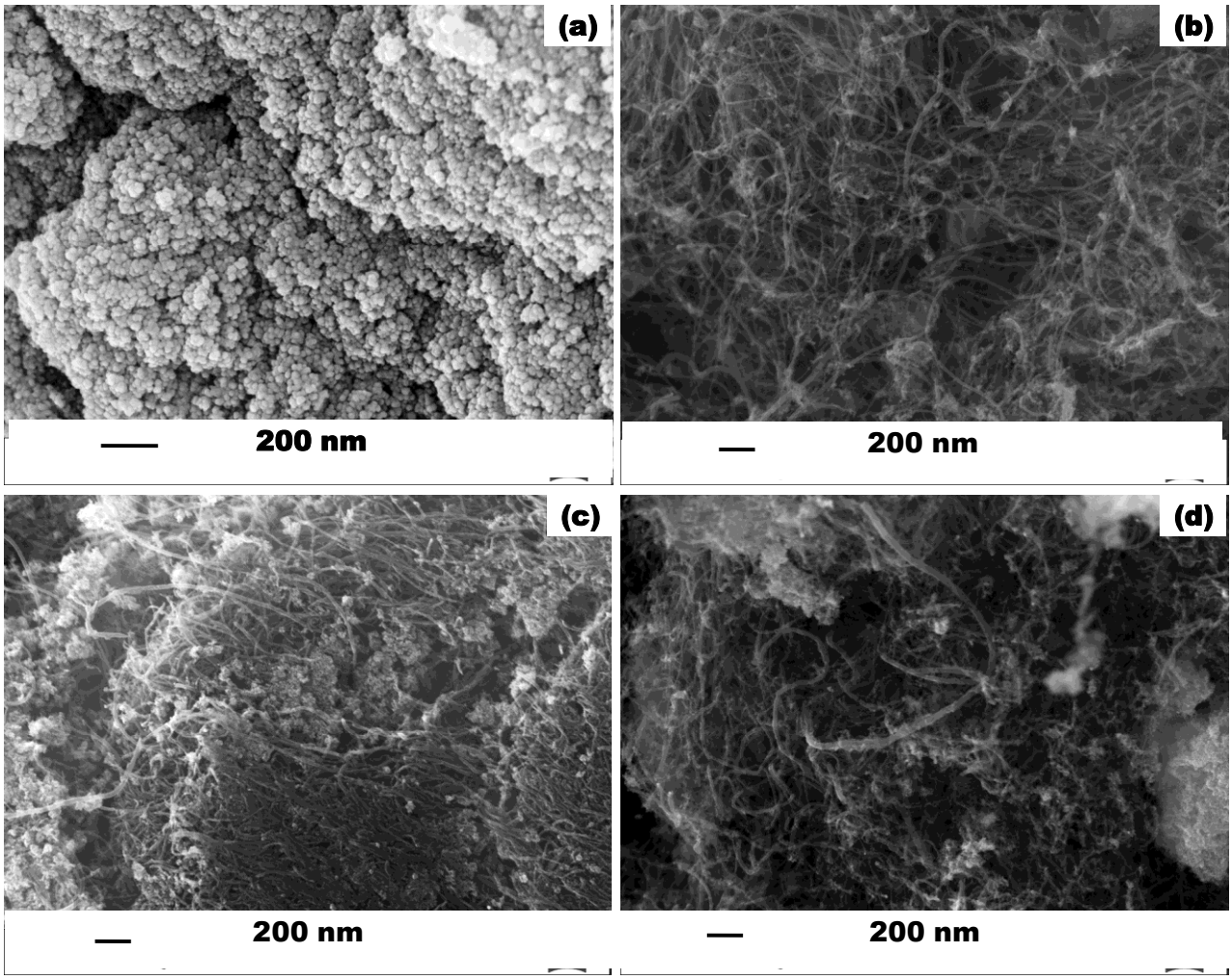

Figure 4. 30 SEM images of TiO_2, 5 wt. %, 10 wt. % and 20 wt. % TiO_2 nanoparticle on 30 SBA-CNT composite (a-d) respectively.

4.3.2 XRD Pattern Analysis of Different [TiO_2] on SBA-CNT

In **Section 4.2.2.1** unsupported anatase phase titania were clearly identified with no evidence of the rutile or the brookite phases, the characteristic anatase peaks appeared at 2θ = 25.31, 37.96, 47.77, 54.18, 62.50, 69.25, 75.11 and 82.87˚ and were assigned to the (110); (004); (200); (211); (204); (220); (215) and (224) reflection planes respectively. **Figure 4.31** depicts peaks corresponding to anatase phase titania. On the 5 wt. % TiO_2/SBA-CNT composite the characteristic peak of anatase at 2θ = 25.00˚ was clearly identified with additional peaks at other positions associated with anatase TiO_2.

As the TiO_2 content was increased on the SBA-CNT support composite, the characteristic peaks for the anatase phase of TiO_2 become more intense. Of importance to note from the XRD pattern was the peak at 43.99˚ which corresponds to the (100) reflection plane of CNTs. The presence of the peak signifies that the crystallinity and probably the SBA-CNT composite properties have been preserved during chemical and thermal treatments.

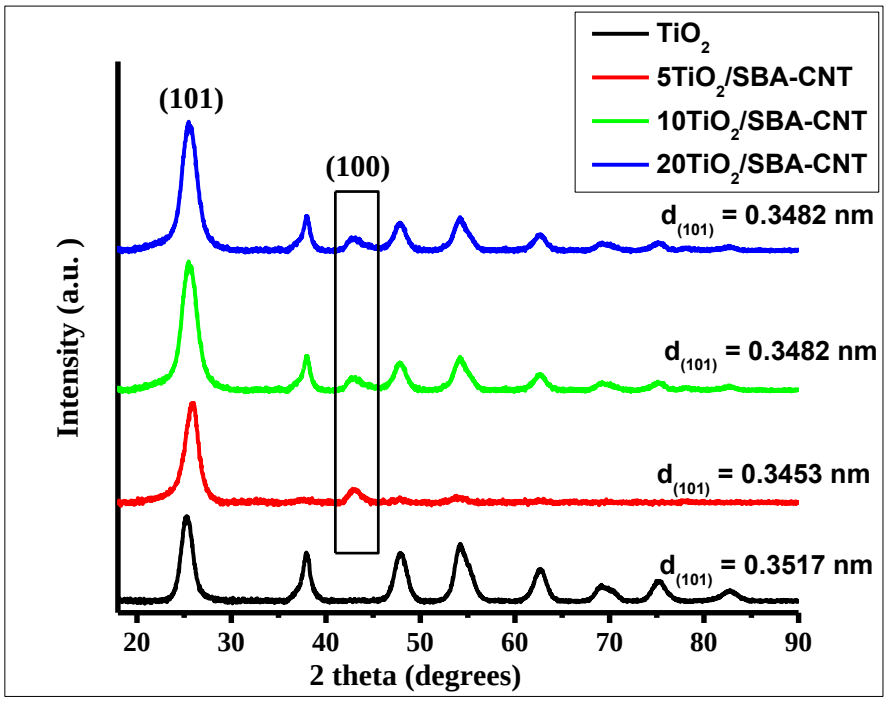

Figure 4. 31 XRD patterns of TiO_2 and 5, 10 and 20 wt. % TiO_2/SBA-CNT composites (rectangular shape highlights the emerging CNTs peaks within the composites).

The interpretation of the FWHM and 2θ degree positions of the peaks were analyzed from the anatase TiO_2 (101) reflection peak and the (211) reflection peak (**Table 4.8**). Both reflection peaks showed that supporting TiO_2 on SBA-CNT composite reduce the growth of the TiO_2 crystals. FWHM of TiO_2 gives details about the crystal size, whereby the narrower the peak, the bigger the crystal size of TiO_2 [43]. The TiO_2 in the 10 wt. % composite had the smallest crystal size from analysis of the FWHM and crystal size calculation using both reflections.

Table 4. 8 Properties of TiO_2 particles within the composites according to XRD pattern analysis.

Catalyst	2 theta (˚)		FWHM (˚)		Crystal size (nm)		Wt (nm)[a]
	(101)	(211)	(101)	(211)	(101)	(211)	
TiO_2	25.13	54.43	1.43	1.91	5.71	4.69	0.2089
5TiO_2/SBA-CNT	25.80	54.04	1.79	1.98	4.57	4.52	0.2051
10TiO_2/SBA-CNT	25.57	54.18	1.93	1.99	4.22	4.48	0.2068
20TiO_2/SBA-CNT	25.57	54.29	1.90	1.72	4.28	5.18	0.2068

[a] Wall thickness calculated from $2d_{(101)}/3^{1/2}$ – pore diameter from Table 4.9, p.109.
(101) denotes the overlapping reflection peak appearing at approximately $2\theta = 26.00^{\circ}$.
(211) denotes the non-overlapping reflection peak appearing at approximately $2\theta = 54.00^{\circ}$.

4.3.3 Raman Spectroscopy and Thermo-gravimetric Analysis of 5, 10 and 20 wt. % TiO_2 on SBA-CNT.

The decreasing I_D/I_G ratio of the CNTs in the nano-composite support what was observed when TiO_2 particles were introduced onto SBA-CNT support (**Table 4.9**). This suggests that the composite becomes more graphitic as the titania nano-particles were introduced. The Raman FWHM of the graphitic band of the nanotubes broadens (69.85, 70.49 and 81.54 cm^{-1}) with an increase in TiO_2 content from 5, 10 and 20 wt. % TiO_2 respectively. The peak broadness is attributed to a decline in the crystal structure of the carbon nanotubes and an increase in the disorder of the tubes [12]. The XRD pattern is in agreement with the loss of crystallinity of the CNTs in the TiO_2/SBA-CNT composites.

Table 4. 9 Effects of TiO_2 particles on Raman vibrations of CNTs coated with SBA-15.

Sample	G band FWHM	G band (cm^{-1})	Ratio (I_D/I_G)
5TiO_2/SBA-CNT	69.85	1572	1.31
10TiO_2/SBA-CNT	70.49	1576	1.36
20TiO_2/SBA-CNT	81.54	1571	0.64

Figure 4.32 shows that unsupported TiO_2 is very thermally stable as can be seen from the percentage weight loss of 5.68. The decomposition at around 100 ˚C in TiO_2 could be due to surface moisture (H_2O). The 30 wt. % SBA-15 coated CNTs decomposes significantly between 460 – 700 ˚C, and this range of temperatures has been reported in the literature [7, 12]. However introducing 5 wt. % TiO_2 to the SBA-CNT composite reduced the decomposition temperature of the composite and then the decomposition temperature gradually changed as the TiO_2 content was increased in the composites. This observation is contrary to that of Da Dalt et al. [44] for TiO_2/CNT composites, probably because of the SiO_2 presence in our composites.

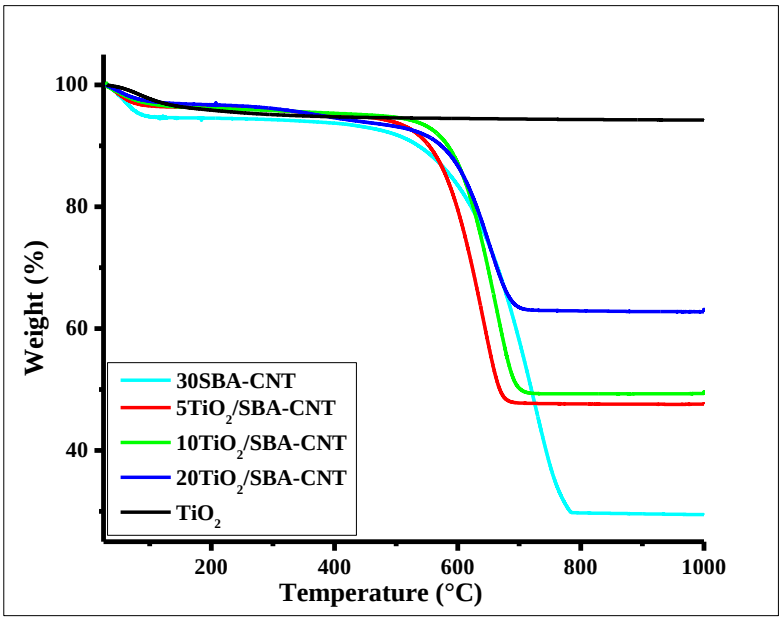

Figure 4. 32 Thermogram patterns of TiO_2, SBA-CNT support and xTiO_2/SBA-CNT composites (x denotes 5, 10 and 20 wt. % TiO_2).

The 20 wt. % TiO_2/SBA-CNT composite experienced the least percentage weight loss of 36.78 wt. %, followed by 50.31 and 52.07 for 10 and 5 wt. % TiO_2/SBA-CNT composites respectively. An increase of TiO_2 concentration in the SBA-CNT support caused a decrease in percentage weight loss of the materials [32]. However, there was a linear increase in thermal stability as the TiO_2 content increased from 5, 10 to 20 wt. % TiO_2. From the thermal behaviour of materials it was evaluated that the weight loss and the amount of mass remaining corresponded to TiO_2 and SBA-15.

4.3.4 Nitrogen Sorption, Optical and PL Studies of Different [TiO_2] on SBA-CNT

Surface area plays a crucial role in the activity of a catalyst, and this is because the surface area is related to the the number of active sites on the surface of the catalyst. **Table 4.10** depicts the analysis of N_2 sorption studies which show a direct proportionality between surface area and TiO_2 loading. The pore volume increases as the TiO_2 loading is increased in the SBA-15 coated CNTs. The increase in pore volume is attributed to the presence of the support framework which has large pore volume of 0.93 nm (**section 4.1.6**). So it could be thought that the presented pore volume in the catalyst system is not a representative of TiO_2 particles but rather of the bulk structure. The textural parameters of the catalyst were enhanced by the support composite, with average pore size distributions of 4.1, 3.2, and 4.2 nm for 5, 10, 20 wt. % TiO_2/SBA-CNT composites respectively (**Appendix A 2.3.2**).

Table 4. 10 Textural parameters and band gap energy of varying TiO_2 loading on SBA-CNT.

Catalyst	S_{BET} (m^2 g^{-1})	Pore vol. (cm^3 g^{-1})	Average Pore diameter (nm)	Bandgap energy (eV) [a]	TiO_2 (wt. %)[b]
5TiO_2/SBA-CNT	252.50	0.83	15.28	2.50	6.72
10TiO_2/SBA-CNT	301.35	0.89	12.56	3.15	11.93
20TiO_2/SBA-CNT	347.74	1.32	17.19	2.85	18.94

[a]Calculated from Kubelka Munk plots similar to those in figure 4.28.
[b]TiO_2 contents calculated from ICP-OES analysis.

Band gap energy of catalysts decreases as the crystal size of TiO_2 in the composite increases. The 20 wt. % TiO_2/SBA-CNT composite had wider band gap energy (2.85 eV) and it was attributed to the agglomerated TiO_2 particles along the support. The morphology of the material consecutively caused a decrease in the crystallinity and increased crystal size of the titania as was observed from XRD analysis. The 10 wt. % TiO_2/SBA-CNT composite had reduced band gap energy of 3.15 eV and this was attributed to agglomerated titania particles in the composite. The 5 wt. % composite showed narrower band gap energy of 2.50 eV amongst the investigated composite materials. This was attributed the very small crystal size, well dispersed and synergic interaction of TiO_2 particle with SBA-CNTs composite [35].

Figure 4.33 shows the PL spectra of materials and from the suppression of peaks in the different catalyst composites it can be established that the lower the titania content, the lower the electron - hole recombination rate of self-trapped excitation in titania. Yen et al. [23] also observed that the introduction of CNTs reduced the e^- - h^+ recombination rate according to PL studies, although their ratio of CNTs to TiO_2 was (0-8 : 100-92). Peak positions in TiO_2 are similar to those encountered and discussed in **section 4.2.5**. The weak intensity of PL from TiO_2 nano-particles could result from a lower density of intra-band-gap states and/or from improved transport [39].

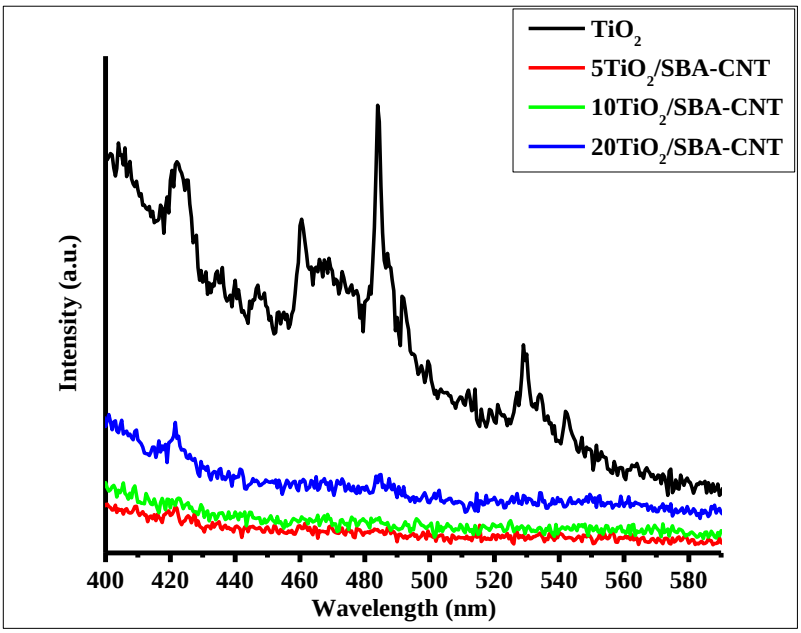

Figure 4. 33 Photoluminescence spectra of TiO_2 and SBA-CNT supported TiO_2.

4.3.5 Conclusions

The characterization analysis demonstrated that the sol-gel method was efficient in synthesizing composite materials. In particular, coating silica to acid treated multi-walled carbon nanotubes. The SBA-CNT composites demonstrated that CNTs are good materials to be considered for composites since their properties are very stable when they are alone and enhanced when in composites. A hydrothermally and chemically stable SBA-15 material with high surface area was successfully synthesized. The sol-gel method adapted using surfactants was able to synthesise high surface area, mesoporous TiO_2 anatase nano-particles. Introducing TiO_2 to different supports namely, SBA-15, acid treated multi-walled carbon nanotubes (aCNTs) and silica coated aCNTs (SBA-CNT) showed that the supports are stable and enhance the physical and chemical properties (thermal, surface, electronic, and structural) of the catalyst (TiO_2). The titania particles had a small crystal size when they were on supports than when they were unsupported. This small crystal size caused a decrease in the band gap energy of the catalyst. Supporting different weight percentages of TiO_2 on the SBA-CNT composite further enhanced the properties of TiO_2 catalyst.

4.4 References

1. Popov, V. N., *Carbon nanotubes: properties and application.* Materials Science and Engineering: R: Reports, 2004. **43**(3): p. 61-102.
2. Zhang, W.-H., Lu, J., Han, B., Li, M., Xiu, J., Ying, P. and Li, C., *Direct synthesis and characterization of titanium-substituted mesoporous molecular sieve SBA-15.* Chemistry of materials, 2002. **14**(8): p. 3413-3421.
3. Hou, P.-X., Liu, C. and Cheng, H.-M., *Purification of carbon nanotubes.* Carbon, 2008. **46**(15): p. 2003-2025.
4. Serp, P., Corrias, M. and Kalck, P., *Carbon nanotubes and nanofibers in catalysis.* Applied Catalysis A: General, 2003. **253**(2): p. 337-358.
5. Rosca, I. D., Watari, F., Uo, M. and Akasaka, T., *Oxidation of multiwalled carbon nanotubes by nitric acid.* Carbon, 2005. **43**(15): p. 3124-3131.
6. Fu, X., Yang, H., He, K., Zhang, Y. and Wu, J., *Enhanced photocatalytic activity of nano titanium dioxide coated on ethanol-soluble carbon nanotubes.* Materials Research Bulletin, 2013. **48**(2): p. 487-494.
7. Gerber, I., Oubenali, M., Bacsa, R., Durand, J., Gonçalves, A., Pereira, M. F. R., Jolibois, F., Perrin, L., Poteau, R. and Serp, P., *Theoretical and Experimental Studies on the Carbon-Nanotube Surface Oxidation by Nitric Acid: Interplay between Functionalization and Vacancy Enlargement.* Chemistry – A European Journal, 2011. **17**(41): p. 11467-11477.
8. Delhaes, P., Couzi, M., Trinquecoste, M., Dentzer, J., Hamidou, H. and Vix-Guterl, C., *A comparison between Raman spectroscopy and surface characterizations of multiwall carbon nanotubes.* Carbon, 2006. **44**(14): p. 3005-3013.
9. Das, N., Eckert, H., Hu, H., Wachs, I. E., Walzer, J. F. and Feher, F. J., Bonding states of surface vanadium (V) oxide phases on silica: structural characterization by vanadium-51 NMR and Raman spectroscopy. The Journal of Physical Chemistry, 1993. **97**(31): p. 8240-8243.

10. Paula, A. J., Stéfani, D., Souza Filho, A. G., Kim, Y. A., Endo, M. and Alves, O. L., *Surface Chemistry in the Process of Coating Mesoporous SiO_2 onto Carbon Nanotubes Driven by the Formation of Si-O-C Bonds.* Chemistry-A European Journal, 2011. **17**(11): p. 3228-3237.
11. Liu, X., Spencer, J., Kaiser, A. and Arnold, W. *Manipulation and purification of multi-walled carbon nanotubes. in Electrical Insulation and Dielectric Phenomena*, 2004. CEIDP'04. 2004 Annual Report Conference on 2004 IEEE.
12. Osswald, S., Havel, M. and Gogotsi, Y., *Monitoring oxidation of multiwalled carbon nanotubes by Raman spectroscopy.* Journal of Raman Spectroscopy, 2007. **38**(6): p. 728-736.
13. Iijima, S., *Helical microtubules of graphitic carbon.* nature, 1991. **354**(6348): p. 56-58.
14. Meynen, V., Cool, P. and Vansant, E., *Verified syntheses of mesoporous materials.* Microporous and Mesoporous Materials, 2009. **125**(3): p. 170-223.
15. Coats, A. and Redfern, J., *Thermogravimetric analysis. A review.* Analyst, 1963. **88**(1053): p. 906-924.
16. Chiang, Y.-C., Lin, W.-H. and Chang, Y.-C., *The influence of treatment duration on multi-walled carbon nanotubes functionalized by H_2SO_4/HNO_3 oxidation*. Applied Surface Science, 2011. **257**(6): p. 2401-2410.
17. Shamsuddin, S. A., Halim, N. H. A., Deraman, N. and Hashim, U. *The characterization study of functionalized multi-wall carbon nanotubes purified by acid oxidation. in Micro and Nanoelectronics (RSM)*, 2011 IEEE Regional Symposium on 2011 IEEE.
18. Mansfield, E., Kar, A. and Hooker, S., *Applications of TGA in quality control of SWCNTs.* Analytical and Bioanalytical Chemistry, 2010. **396**(3): p. 1071-1077.
19. Lambin, P., Loiseau, A., Culot, C. and Biro, L., *Structure of carbon nanotubes probed by local and global probes.* Carbon, 2002. **40**(10): p. 1635-1648.
20. Acosta-Silva, Y. J., Nava, R., Hernández-Morales, V., Macías-Sánchez, S. A., Gómez-Herrera, M. L. and Pawelec, B., *Methylene blue photodegradation over titania-decorated SBA-15.* Applied Catalysis B: Environmental, 2011. **110**: p. 108-117.

21. Naik, B., Manoratne, C. H., Chandrashekhar, A., Iyer, A., Prasad, V. S. and Ghosh, N. N., *Preparation of TiO_2, Ag-doped TiO_2 nanoparticle and TiO_2-SBA-15 nanocomposites using simple aqueous solution-based chemical method and study of their photocatalytical activity*. Journal of Experimental Nanoscience, 2013. **8**(4): p. 462-479.
22. Pierotti, R. and Rouquerol, J., *Reporting physisorption data for gas/solid systems with special reference to the determination of surface area and porosity*. Pure Applied Chem, 1985. **57**(4): p. 603-619.
23. Yen, C.-Y., Lin, Y.-F., Hung, C.-H., Tseng, Y.-H., Ma, C.-C. M., Chang, M.-C. and Shao, H., *The effects of synthesis procedures on the morphology and photocatalytic activity of multi-walled carbon nanotubes/TiO_2 nanocomposites*. Nanotechnology, 2008. **19**(4): p. 045604.
24. Dong, W., Sun, Y., Ma, Q., Zhu, L., Hua, W., Lu, X., Zhuang, G., Zhang, S., Guo, Z. and Zhao, D., *Excellent photocatalytic degradation activities of ordered mesoporous anatase TiO_2-SiO_2 nanocomposites to various organic contaminants.* Journal of Hazardous Materials, 2012. **229-230**: p. 307-320.
25. Donohue, M. D. and Aranovich, G. L., *Classification of Gibbs adsorption isotherms.* Advances in Colloid and Interface Science, 1998. **76–77**(0): p. 137-152.
26. Enterria, M., Suarez-Garcia, F., Martinez-Alonso, A. and Tascon, J. M. D., *Avoiding structure degradation during activation of ordered mesoporous carbons.* Carbon, 2012. **50**(10): p. 3826-3835.
27. Yu, J. C., Yu, J. and Zhao, J., *Enhanced photocatalytic activity of mesoporous and ordinary TiO_2 thin films by sulfuric acid treatment.* Applied Catalysis B: Environmental, 2002. **36**(1): p. 31-43.
28. Oseghe, E. O., Ndungu, P. G. and Jonnalagadda, S. B., *Synthesis of mesoporous Mn/TiO_2 nanocomposites and investigating the photocatalytic properties in aqueous systems.* Environmental Science and Pollution Research, 2014: p. 1-12.
29. Wang, X. J., Li, F. T., Hao, Y. J., Liu, S. J. and Yang, M. L., *TiO_2/SBA-15 composites prepared using H_2TiO_3 by hydrothermal method and its photocatalytic activity.* Materials Letters, 2013. **99**: p. 38-41.

30. Lachheb, H., Ahmed, O., Houas, A. and Nogier, J. P., *Photocatalytic activity of TiO_2-SBA-15 under UV and visible light.* Journal of Photochemistry and Photobiology A: Chemistry, 2011. **226**(1): p. 1-8.
31. Chena, L., Pangb, X., Yua, G. and Zhanga, J., *In-situ coating of MWNTs with sol-gel TiO_2 nanoparticles.* Adv Mater Lett, 2010. **1**(1): p. 75-8.
32. Jitianu, A., Cacciaguerra, T., Benoit, R., Delpeux, S., Béguin, F. and Bonnamy, S., *Synthesis and characterization of carbon nanotubes-TiO_2 nanocomposites.* Carbon, 2004. **42**(5-6): p. 1147-1151.
33. Di Paola, A., Bellardita, M., Palmisano, L., Barbieriková, Z. and Brezová, V., *Influence of crystallinity and OH surface density on the photocatalytic activity of TiO_2 powders.* Journal of Photochemistry and Photobiology A: Chemistry, 2014. **273**(0): p. 59-67.
34. Han, F., Kambala, V. S. R., Srinivasan, M., Rajarathnam, D. and Naidu, R., *Tailored titanium dioxide photocatalysts for the degradation of organic dyes in wastewater treatment: A review.* Applied Catalysis A: General, 2009. **359**(1–2): p. 25-40.
35. Xu, Y.-J., Zhuang, Y. and Fu, X., *New insight for enhanced photocatalytic activity of TiO_2 by doping carbon nanotubes: a case study on degradation of benzene and methyl orange.* The Journal of Physical Chemistry C, 2010. **114**(6): p. 2669-2676.
36. Abazovic, N. D., C˘omor, M. I., Dramicanin, M. D., Jovanovic, D. J., Ahrenkiel, S. P. and Nedeljkovic, J. M., *Photoluminescence of anatase and rutile TiO_2 particles.* The Journal of Physical Chemistry B, 2006. **110**(50): p. 25366-25370.
37. Pany, S., Parida, K. M. and Naik, B., *Facile fabrication of mesoporosity driven N-TiO_2@CS nanocomposites with enhanced visible light photocatalytic activity*. Royal Society of Chemistry Advances, 2013. **3**(15): p. 4976-4984.
38. Knorr, F. J., Zhang, D. and McHale, J. L., *Influence of $TiCl_4$ treatment on surface defect photoluminescence in pure and mixed-phase nanocrystalline TiO_2*. Langmuir, 2007. **23**(17): p. 8686-8690.
39. Mercado, C. C., Knorr, F. J. and McHale, J. L., *Observation of charge transport in single titanium dioxide nanotubes by micro-photoluminescence imaging and spectroscopy*. American Chemical Soviety Nano, 2012. **6**(8): p. 7270-7280.

40. Ruoff, R. S., Qian, D. and Liu, W. K., *Mechanical properties of carbon nanotubes: theoretical predictions and experimental measurements*. Comptes Rendus Physique, 2003. **4**(9): p. 993-1008.
41. Shi, E., Zhang, L., Li, Z., Li, P., Shang, Y., Jia, Y., Wei, J., Wang, K., Zhu, H., Wu, D., Zhang, S. and Cao, A., *TiO_2-coated carbon nanotube-silicon solar cells with efficiency of 15%*. Scientific Reports, 2012. **2**.
42. Wang, W., Serp, P., Kalck, P., Silva, C. G. and Faria, J. L., *Preparation and characterization of nanostructured MWCNT-TiO_2 composite materials for photocatalytic water treatment applications*. Materials Research Bulletin, 2008. **43**(4): p. 958-967.
43. Chen, X. and Mao, S. S., *Titanium dioxide nanomaterials: synthesis, properties, modifications, and applications.* Chemical reviews, 2007. **107**(7): p. 2891-2959.
44. Da Dalt, S., Alves, A. K. and Bergmann, C. P., *Photocatalytic degradation of methyl orange dye in water solutions in the presence of MWCNT/TiO_2 composites*. Materials Research Bulletin, 2013. **48**(5): p. 1845-1850.
45. Hintsho, N., Petrik, L., Nechaev, A., Titinchi, S. and Ndungu, P., *Photo-catalytic activity of titanium dioxide carbon nanotube nano-composites modified with silver and palladium nanoparticles.* Applied Catalysis B: Environmental, 2014. **156–157**(0): p. 273-283.

Chapter 5
Photo-Catalytic Studies

5.1 Photo-catalytic Activity of 10 wt. % TiO_2 on Supports (CNTs, SBA-15 and SBA-CNT)

This section explores the activity of the 10 wt. % TiO_2 on different support frameworks namely, CNT, SBA-15 and 30 wt. % SBA-15 coated CNTs. These materials were prepared according to Chapter 3, sections 3.3.1-3.3.3 and 3.3.4. The photo-catalytic activities of these materials were conducted on methylene blue (MB) as a model pollutant dye in order to study the effect of support systems on TiO_2 nano-particle photo-catalysts. The catalyst support composite that worked best to decolorize MB was chosen as the optimum support and it was employed for further investigations.

Figure 5.1a shows the adsorption properties of the various catalysts during the period of stirring in the dark before the solution was irradiated with visible light. The synthesized catalysts were able to effectively adsorb pollutant molecules and facilitate MB de-colorization within the first hour of contact and before irradiating with light. P25 represents the commercial (Degussa P25) TiO_2 catalyst which was employed as a reference material for the photo-catalytic studies. It was anticipated that the mesoporous structure and high surface area of the synthesized TiO_2 material would enhance its catalytic performance and outperform P25. However, the catalysts (P25 and mesoporous TiO_2) were highly competitive with regards to their adsorption of the MB in the dark (represented by sharp slope before 0 minutes), while mesoporous titania particles did not have a greatly enhanced adsorption of MB molecules. A significant amount of MB was adsorbed by the TiO_2/SBA-15, TiO_2/CNT and the TiO_2/SBA-CNT nano-composite catalysts. These high adsorptions are attributed to the high specific surface areas of the composites and the synergistic effect between titanium dioxide and the respective supports.

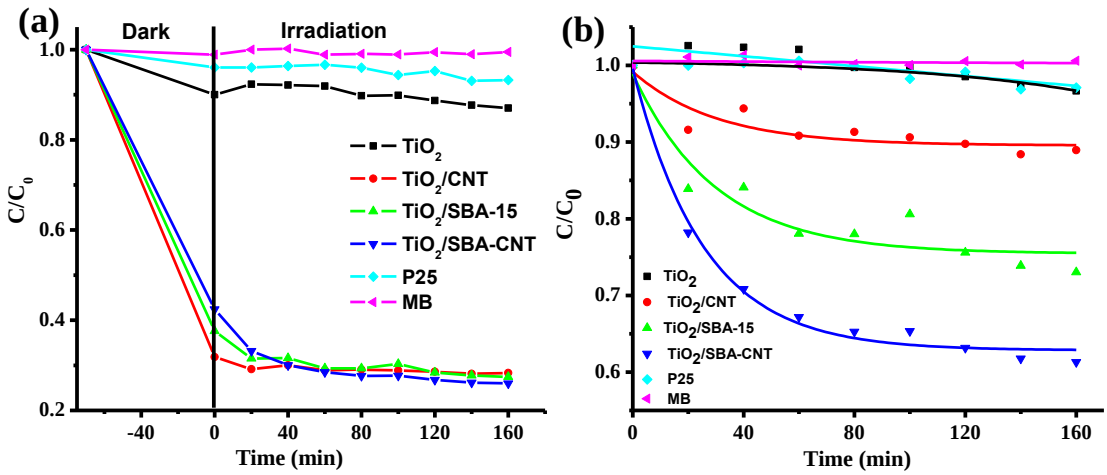

Figure 5. 1 **S**orption equilibrium properties of materials while in the dark and after irradiation (a) photo-catalytic activity of materials under visible light irradiation (b).

Figure 5.1b represents the photo-activity of the catalysts after irradiation with a 32 W visible day light halogen lamp. The titania particles supported on the composite of TiO_2/SBA-CNT de-colorized the MB molecules better than the other composites. The activity of these catalyst composite was attributed to their relatively high surface area (301.35 m^2 g^{-1}), small band gap energies (3.15 eV) and very slow electron – hole recombination rates. The enhanced photo-catalytic de-colorization of MB by the TiO_2/SBA-CNT as compared to the TiO_2/CNTs and TiO_2/SBA-15 composite might be due to the synergy between CNTs, SBA-15 and TiO_2 which enables the catalyst to adsorb MB dye molecules and facilitate movement of pollutants and products during the reaction.

Unexpectedly, the TiO_2/SBA-15 composite performed better than the TiO_2/CNT composite which had small TiO_2 crystals, reduced band-gap energy, high surface area, and slow electron-hole recombination rates. The photo-catalytic performance was attributed to the morphological structure of TiO_2/SBA-15 composite which showed a long range order of the curved pore walls that are reported to facilitate the movements of pollutant and products during catalytic reactions.

The photo-activity of TiO_2/SBA-15 was expected to be low because of the white color of the material which could have reflected the visible light energy and in turn generate a small population of electron-hole that are responsible for generating the active species that de-colorize the MB. Also, photoluminescence studies of TiO_2/SBA-15 showed oxygen vacancies which suggested that the sample could have fast rates of electron – hole recombination, a characteristic reported to influence photo-performance negatively during catalysis [1]. The study of Acosta et al. [2] attributed the high surface area, good adsorption properties but low de-colorization efficiencies of TiO_2/SBA-15 composites to possibilities of competitive co-adsorption of MB and recalcitrant by-products which might have absorbed at the same wavelength as MB.

MWCNTs could have enhanced the photo-catalytic activity of TiO_2 under visible light irradiation through good adsorptive abilities and photochemical properties of CNTs once functionalized. Yu et al. [3] attributed the enhanced photo-catalytic activity of titania-carbon nanotubes composites to the electronic synergy between TiO_2 and CNTs. It is well known that electrons can move freely within the cylindrical structure of the CNTs at room temperature without any scattering from atoms or defects, a phenomenon referred to as ballistic transport. Such excellent transport properties, regarding electrons, may play a role in the effective separation of electrons and holes during the photo-catalytic process. The PL studies showed a decrease in e-h recombination rate and thus support this idea, and in addition, similar results have been reported in the literature. Recent studies by Hintsho et al. [4] demonstrated that functionalized CNTs alone can remove methylene blue up to 20% during 6 hours of irradiation with a 12 W UV lamp. The photo-activity of the nanotubes was attributed to the presence of functional groups, which could have served as centres for radical species generation. The same study decolorized 53% MB within 6 hours of irradiation with 10 wt. % TiO_2/CNT composite which was synthesized through MOCVD method. Comparatively our 10 wt. % TiO_2/CNT composite synthesized with the solution method decolorized a total of 70% MB in 30 minutes of catalyst and pollutant interaction. Such variations are thought to be a result of composite properties which is brought about by the involved synthesis chemistry. The distinctive performance of these materials supports the view that the sol-gel method is highly effective for coating and enhancing properties of CNTs, and ultimately enhancing photo-catalytic activity of TiO_2.

These results showed that the photo-catalytic activity of materials, in particular, the efficiency of the catalyst composites does not only depend on the adsorption properties of the material surfaces, rather, on the physico-chemical properties of the catalyst composites which is brought about by the synergy between the TiO_2 and support.

5.2 Photo-catalytic Activity of 5, 10 and 20 wt. % TiO_2 supported on SBA-CNT

This section describes and analyses the results on the use of SBA-CNT composite to support and study the photo-catalytic activity of TiO_2 at different catalyst (TiO_2) weight loadings. The support composites hosted 5, 10 and 20 wt. % TiO_2 nano-particles on SBA-CNT. These materials were prepared according to Chapter 3, section 3.3.4. The activity of the catalysts was monitored by observing the de-colorization of MB and the composite that decolorized MB effectively was identified for further photo-catalytic activity investigations.

Figure 5.2 (dark) shows that the SBA-CNT supported TiO_2 composites were highly adsorptive before irradiation. The unsupported TiO_2 was able to adsorp ≈ 10% MB molecules while Degussa P25 showed very little adsorption. This is attributed to the high surface area and porous structure of the prepared unsupported titanium material. The 5 wt. % TiO_2/SBA-CNT composite showed the greatest adsorption of the MB molecules, and this could have been because the catalyst composite had little weight loading of TiO_2 and more of the SBA-CNT support. The relatively high surface area SBA-CNT support was therefore exposed to the MB molecules for adsorption during pre-treatment of the pollutant and catalyst mixture before irradiating with light.

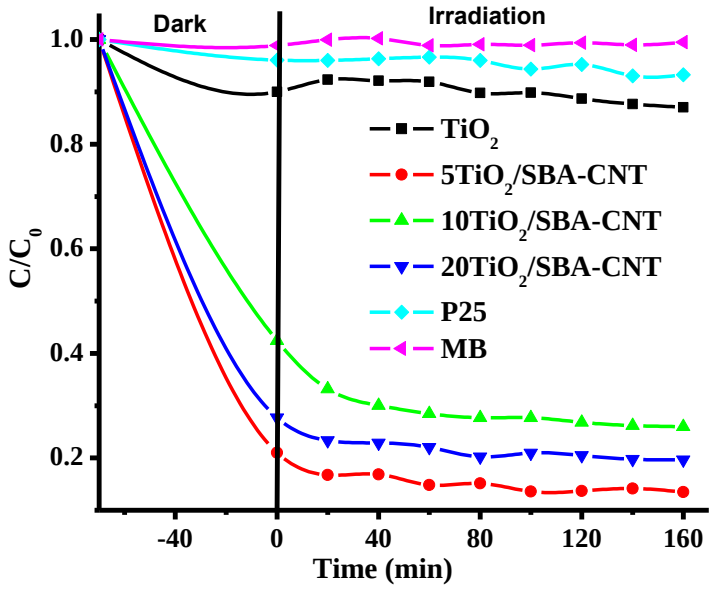

Figure 5. 2 Catalytic activity of materials before and after irradiation with visible light irradiation.

After irradiation with light the activity of catalysts showed that 5 wt. % TiO_2 composite was the most active photo-catalyst. The activity of the catalyst was attributed to the small crystals of titanium (4.28 nm) and low band gap energy (2.50 eV). From **Chapter 4, section 4.3** the crystal sizes were 4.28, 4.48 and 4.57 nm and the band gap energies were 2.50, 3.15 and 2.85 eV respectively for the 5, 10, and 20 wt. % composites. PL studies also showed that the 5 wt. % composite had the slowest electron-hole recombination rates as compared to the 10 and 20 wt. % composites. The low electron-hole recombination rate imply that the oxidizing agents remain in the system long enough to degrade as many pollutant molecules as possible [4]. This mechanism of photo-de-coloration explains the reason the 5 wt. % composite was able to efficiently decolorize 84% MB molecules (**Figure 5.3**).

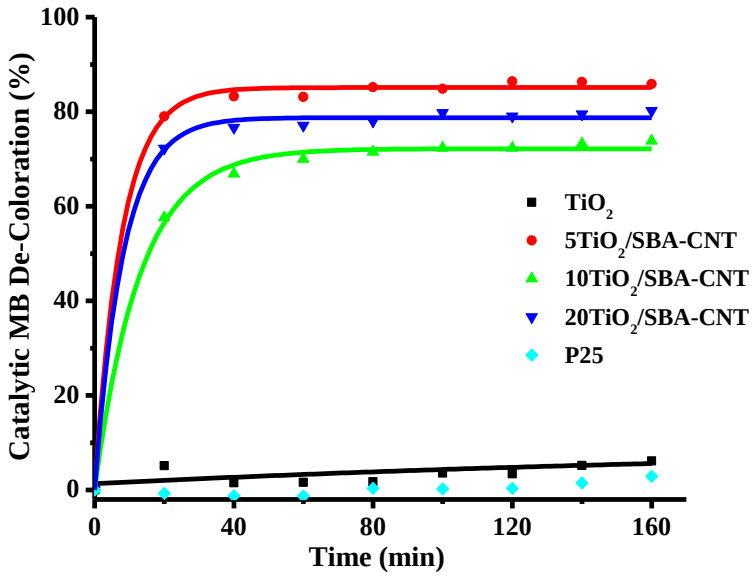

Figure 5. 3 Photo-catalytic efficiency of the catalysts (0.13 g L^{-1}) to decolorize MB (10 mg L^{-1}). The samples were run at neutral solution pH, stirring rate 140 RPM and irradiating with 32 W visible lamp.

The total de-colorization of the pollutant by 5 wt. % TiO_2/SBA-CNT catalyst showed that the synergistic effect between the electronic properties of TiO_2 and CNTs was the most influential factor that enhances the efficiency of the catalyst composite. The large surface area and pore volume of the 10 and 20 wt. % composites did not exhibit the best degradation rates as anticipated from the understanding of high active sites and ease of pollutant molecules transportation. Perhaps the TiO_2 crystallinity within the materials is the draw back to the material activity and thus minimizes the interaction of the SBA-CNT composite with titania particles at high TiO_2 contents. The photo-catalytic activities of the catalyst were directly proportional to the band gap energy of the catalysts.

The photo-catalytic de-coloration of methylene blue is well established in literature, and follows a pseudo first order kinetics model. The first order rate constant of the materials were normalized with respect to the surface area of the composites as a way to account for the catalytic activity of materials prepared and studied under similar condition (**Table 5.1**).

Table 5. 1 Methylene blue de-colorization kinetic studies with prepared catalysts.

Catalyst	Rate constant, K (min^{-1})	Normalized K ($min^{-1} m^{-2}$)	S_{BET} ($m^2 g^{-1}$)*
TiO_2	-4.5694×10^{-4}	-1.09974×10^{-4}	207.75
$5TiO_2$/SBA-CNT	-1.6420×10^{-3}	-3.25149×10^{-4}	252.50
$10TiO_2$/SBA-CNT	-1.5316×10^{-3}	-2.54123×10^{-4}	301.35
$20TiO_2$/SBA-CNT	-1.2602×10^{-3}	-1.81199×10^{-4}	347.74
P25 (commercial TiO_2)	N/A[≠]	N/A[≠]	8.81

*Specific surface area from N_2 sorption studies.
[≠]The reaction time for P25, with the lamp used, and the extent of the reaction was very low (less than 5%) and thus the data collected could not be used to calculate the rate constant.

The rate constants K, of the catalyst showed that the composite catalysts had a fast rate of de-coloration on MB as compared to the unsupported TiO_2 and P25 catalysts. This is supported by the steep slope observed from the de-colourization graphs (**Figure 5.2**). The fast de-colorization rate constant before normalizing was attributed to the high surface area and the porosity of the materials. Compared to the P25 photo-catalyst, the prepared materials were more efficient in de-colourizing MB according to the total percentage removal graph (**Figure 5.3**). The enhanced de-colourization and % removal efficiency of MB by the 5, 10 and 20 wt. % TiO_2/SBA-CNT materials was attributed to the reduced band gap energies and the slow electron – hole recombination rates of the composites, together with the high surface area, small TiO_2 crystal sizes, which could have influenced the activity of these materials under visible light irradiation. In overall, the rate constant results show that high surface area TiO_2 and composite TiO_2 catalyst enhance the de-coloration activity of the catalyst under visible light irradiation.

5.3 Photo-catalytic Activity of 5, 10 and 20 wt. % TiO_2 on SBA-CNT on the Photo-degradation of MCPA

This section explores the photo-catalytic activity of the 5 wt. % TiO_2/SBA-CNT composite catalyst on the transformation of 4-chloro-2-methylphenoxy acetic acid (MCPA), a common herbicide. In this section effects of different variables, namely, solution pH, catalyst concentration and pollutant concentration were investigated. The catalyst with the best de-colourization efficiency in the dye experiments was chosen for MCPA optimization and catalyst efficiency tests, the 5 wt. % TiO_2/SBA-CNT composite. Transformation concentrations were studied on the High Performance Liquid Chromatography (HPLC) following methods in Chapter 3, section 3.2.9 and 3.4.

5.3.1 Effects of solution pH on catalyst efficiency

Solutions of MCPA with a concentration of 8 mg L^{-1} were prepared at pH 2.98, 8.20 and at the natural pH of the MCPA solution (pH = 4.68). A mass of 0.1 g L^{-1} of the 5 wt. % TiO_2/SBA-CNT catalyst nano-composite was employed to study the effect of pH on the degradation of MCPA.

Figure 5.4 shows that photo-degradation of MCPA was enhanced at solution pH 8.20. After 160 minutes of irradiating with the 32 W visible light lamp, the solution pH was found to have decreased to ≈7.74. The drop in pH as the reaction proceeds could be attributed to the breakdown of MCPA and the production of acidic chlorine ions which form HCl in the aqueous solution [8, 9].

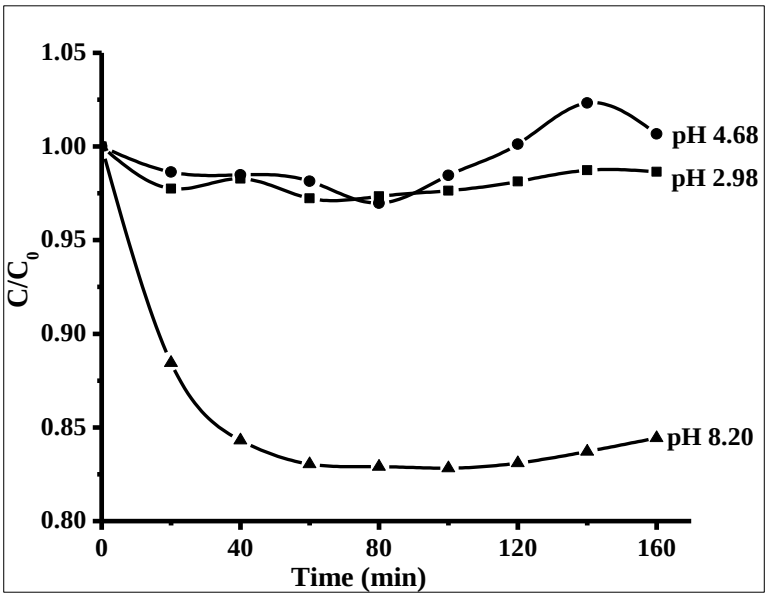

Figure 5. 4 Photo-degradation of 8 mg L^{-1} MCPA with 0.1 g L^{-1} 5 wt. % TiO_2/SBA-CNT composite at different pH conditions.

The pKa value of MCPA is reported to be 3.07 [10]. Understanding of the Columbic interactions, suggest that the best working pH solution would be higher than 3.07 since the herbicide molecules movement would be facilitated towards the catalyst surface, therefore allowing for greater interaction between catalyst, pollutant and photon energy for the absorption and transformation of MCPA. The photo-catalytic activity of the 5 wt. % TiO_2/SBA-CNT composite showed that transformation of MCPA can be enhanced at high pH values [11, 8]. At natural (4.68) and acidic (2.98) pH an increase in concentration of MCPA was observed during the photo-catalysis reactions. Pirozzi et al. [9] attributed this to the transformation of MCPA into more acidic groups (HCl). Or alternatively, the apparent increase in MCPA concentration could be due to the transformation product having overlapping peaks with that of MCPA [12]. It has been reported that at very acidic pH solution the main pathway of transformation is through photo-chemical rearrangement. Before irradiating with light, the catalyst absorbed most the pollutant molecule when the pH was 8.20 followed by the solution at 4.68. When the solution pH was 2.98 no significant absorption of MCPA was noted on the catalyst surface.

5.3.2 Effect of catalyst concentration

The effect of catalyst concentration has been studied and understood to affect catalysis. The effect of catalyst concentration on the transformation of MCPA (**Figure 5.5**) was studied within the range 0.1 – 0.5 g L^{-1} 5 wt. % TiO_2/SBA-CNT catalyst concentrations at pH 8.20 with 8 mg L^{-1} concentration of MCPA. In a heterogeneous regime, the mass of the catalyst is directly proportional to the photo-catalytic reaction rate. It was observed that at low catalyst concentrations (0.1 g L^{-1}), MCPA was efficiently degraded when compared to other catalyst concentrations (0.25 and 0.5 g L^{-1}). It could be that increasing the catalyst concentration caused particle aggregations which reduce the number of active sites for photo-catalysis, therefore decreasing the reaction rate since less pollutant could be degraded with fewer active sites availble [13]. In addition, at high mass loadings of the catalyst into the solution, the light could not penetrate the solution due to some of the catalyst absorbing and thus blocking light from reaching any catalyst 'further in' – i.e. a screening effect due to large amounts of particulates in the solution. As the concentration of the catalyst increased in the solution medium, possibilities of light scattering also increase with screening effects [14].

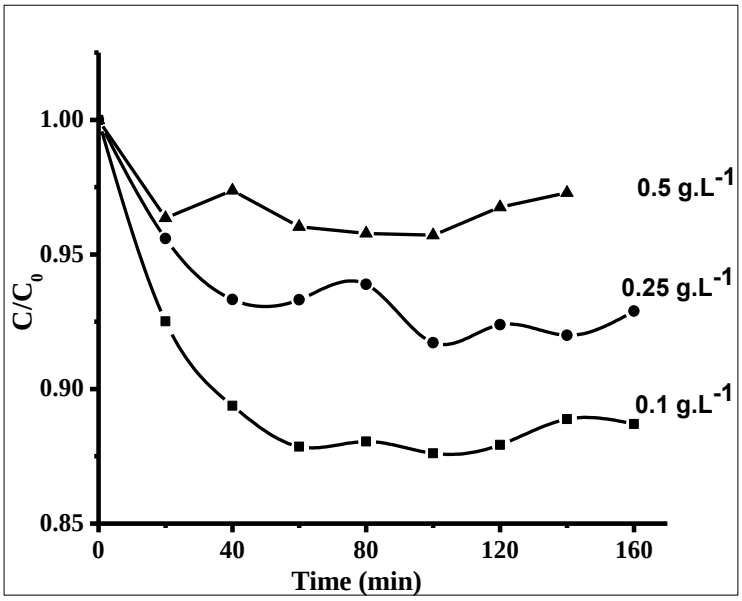

Figure 5. 5 Influence of catalyst concentration on the transformation of 8 mg L^{-1} MCPA under irradiation.

5.3.3 Effect of pollutant concentration

During photo-catalytic oxidation reactions, the degradation of the organic pollutant becomes dependent on the amount of light irradiating on the catalyst surface over time [14]. At high pollutant concentrations the catalyst efficiency decreases as the catalyst surface becomes saturated and leads to minimized photo-activities. At high pollutant concentrations the pollutants can also trap the generated electron-holes at the surface of the catalyst and thus prevent the formation of active radicals which are responsible for degrading the pollutant. Several studies on various organic pollutants have shown that increasing the pollutant concentration causes a decrease in the catalyst degradation efficiency [15]. However our studies on MCPA showed otherwise according to **Figure 5.6**. We observed that the maximum photo-catalytic efficiency of our catalyst composite was attained when the concentration of MCPA was at higher concentrations (8 mg L^{-1}) as opposed to lower concentrations (2 mg L^{-1}). At MCPA concentrations of 4 mg L^{-1} no degradation was observed, instead we observed a phenomenon that suggests the presence of overlapping peaks from by products of MCPA which in turn appear as if the MCPA concentrations increase. This has been related to the formation of HCl into the solution and can also be related to photochemical rearrangements [9, 16].

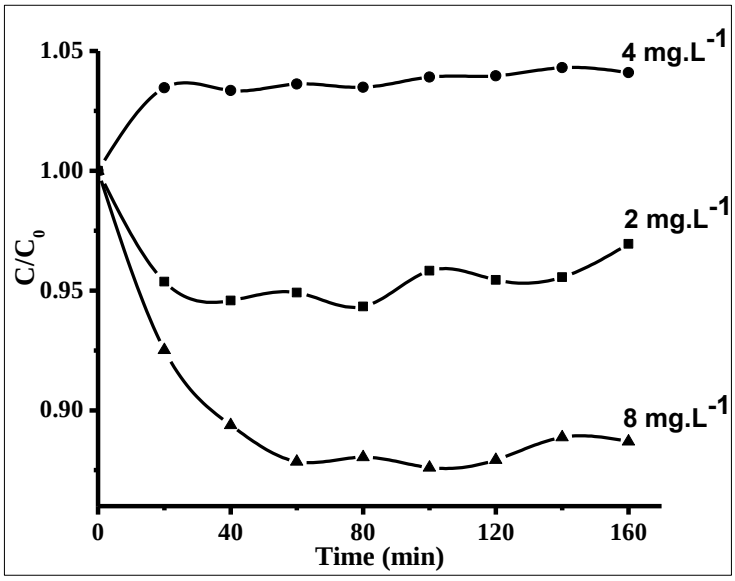

Figure 5. 6 Influence of MCPA concentration during photo-catalytic degradation with 0.1 g L^{-1} 5 wt. % TiO_2/SBA-CNT at pH 8.2.

5.4 Photo-catalytic transformation of MCPA under optimum conditions

The photo-degradation of the herbicide aromatic ring takes place simultaneously with chloride evolution, whereby the reaction in both cases follows first-order kinetics [15]. **Figure 5.7** show the activity of commercial TiO_2, Degussa P25 catalysts under the conditions found to be optimum with the 5 wt. % TiO_2/SBA-CNT composite. MCPA herbicide was not stable, since its concentrations seemed to be increasing when irradiated with visible light in the absence of a catalyst. P25 could not initiate MCPA transformation under the set conditions, however 5 wt. % TiO_2/SBA-CNT catalyst was able to initiae MCPA transformation.

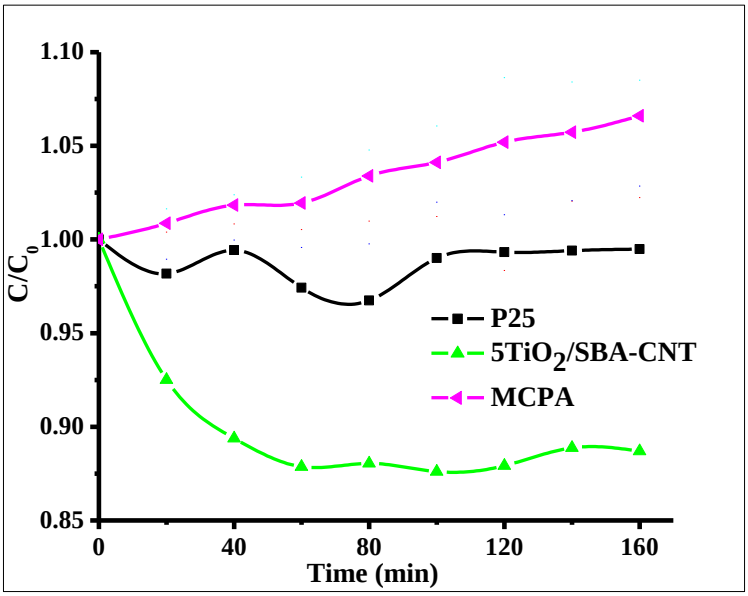

Figure 5. 7 Photo-catalytic activity of catalysts on 8 mg L^{-1} MCPA solution with 0.1 g L^{-1} catalyst concentration at pH 8.2.

Several peaks have been identified by other authors to appear on the HPLC chromatograms at retention times of about 4.9 minutes. The peak has been repeatedly associated with the main by-product, 4-chloro-2-methylphenol [16]. In this work we did not identify any significant new peaks during the transformation reactions. This was attributed to the very slow decrease of the herbicide concentration which could not allow the formation of by-products or it could mean that the transformation by-products have overlapping peaks with MCPA.

The differences in the efficiency of our catalyst with two substrates of different structures imply that photo-catalytic activity was greatly influenced by the molecular structure of the pollutant. Lowering band gap of titanium and increasing surface area does not always favour photo-catalytic degradation depending on the substrate of target; however it offers advantages of activity under the visible light irradiation, adsorption and slow electron – hole recombination rate. The study of Sojic et al. [16] illustrated that the efficiency of photo-catalytic degradation in particular to herbicides was highly influenced by molecular structure rather than physicochemical properties of the catalyst. However, a catalyst with pores and high surface area enhances the transformation and degradation of organic pollutants irrespective of their structures.

5.4 References

1. Stevanovic, A., Büttner, M., Zhang, Z. and Yates Jr, J. T., *Photoluminescence of TiO_2: effect of UV light and adsorbed molecules on surface band structure.* Journal of the American Chemical Society, 2011. **134**(1): p. 324-332.
2. Acosta-Silva, Y. J., Nava, R., Hernández-Morales, V., Macías-Sánchez, S. A., Gómez-Herrera, M. L. and Pawelec, B., *Methylene blue photodegradation over titania-decorated SBA-15.* Applied Catalysis B: Environmental, 2011. **110**: p. 108-117.
3. Yu, Y., Yu, J. C., Yu, J.-G., Kwok, Y.-C., Che, Y.-K., Zhao, J.-C., Ding, L., Ge, W.-K. and Wong, P.-K., *Enhancement of photocatalytic activity of mesoporous TiO_2 by using carbon nanotubes.* Applied Catalysis A: General, 2005. **289**(2): p. 186-196.
4. Hintsho, N., Petrik, L., Nechaev, A., Titinchi, S. and Ndungu, P., *Photo-catalytic activity of titanium dioxide carbon nanotube nano-composites modified with silver and palladium nanoparticles.* Applied Catalysis B: Environmental, 2014. **156–157**(0): p. 273-283.
5. Di Paola, A., Bellardita, M., Palmisano, L., Barbieriková, Z. and Brezová, V., *Influence of crystallinity and OH surface density on the photocatalytic activity of TiO_2 powders.* Journal of Photochemistry and Photobiology A: Chemistry, 2014. **273**(0): p. 59-67.
6. Wei, W., Yu, C., Zhao, Q., Qian, X., Li, G. and Wan, Y., *Synergy effect in photodegradation of contaminants from water using ordered mesoporous carbon-based titania catalyst*. Applied Catalysis B: Environmental, 2013.
7. Xu, H., Pan, Y., Kou, H., Zhu, Y. and Guo, J., *Preparation of transparent ordered mesoporous carbon/silica composites and their optical limiting properties*. Journal of Alloys and Compounds, 2010. **502**(1): p. L6-L9.
8. Zertal, A., Sehili, T. and Boule, P., *Photochemical behaviour of 4-chloro-2-methylphenoxyacetic acid: Influence of pH and irradiation wavelength.* Journal of Photochemistry and Photobiology A: Chemistry, 2001. **146**(1–2): p. 37-48.
9. Pirozzi, D. and Sannino, F., *Design of a multi-stage stirred adsorber using mesoporous metal oxides for herbicide removal from wastewaters.* Journal of Environmental Chemical Engineering, 2014. **2**(1): p. 211-219.

10. Irmak, S., Kusvuran, E. and Erbatur, O., *Degradation of 4-chloro-2-methylphenol in aqueous solution by UV irradiation in the presence of titanium dioxide*. Applied Catalysis B: Environmental, 2004. **54**(2): p. 85-91.
11. Djebbar, K., Zertal, A. and Sehili, T., *Photocatalytic Degradation of 2, 4-Dichlorophenoxyacetic Acid and 4-Chloro-2-Methylphenoxyacetic Acid in Water by using TiO_2*. Environmental technology, 2006. **27**(11): p. 1191-1197.
12. Sofia, B., Tiago, S., Garrido, J., Andrade, B. P., Sottomayor, M. J., Fernanda, B. and Garrido, E. M., *Effects of chlorophenoxy herbicides and their main transformation products on dna damage and acetylcholinesterase activity*. BioMed Research International, Hindawi, 2014. **2014** (709036): p.10.
13. Saquib, M. and Muneer, M., *Titanium dioxide mediated photocatalyzed degradation of a textile dye derivative, acid orange 8, in aqueous suspensions*. Desalination, 2003. **155**(3): p. 255-263.
14. Gaya, U. I. and Abdullah, A. H., *Heterogeneous photocatalytic degradation of organic contaminants over titanium dioxide: A review of fundamentals, progress and problems*. Journal of Photochemistry and Photobiology C: Photochemistry Reviews, 2008. **9**(1): p. 1-12.
15. Ahmed, S., Rasul, M. G., Brown, R. and Hashib, M. A., *Influence of parameters on the heterogeneous photocatalytic degradation of pesticides and phenolic contaminants in wastewater: A short review*. Journal of Environmental Management, 2011. **92**(3): p. 311-330.
16. Sojic, D. V., Despotovic, V. N., Comor, M. I. and Abramovic, B. F., *Photocatalytic degradation of selected herbicides in aqueous suspensions of doped titania under visible light irradiation.* Journal of hazardous materials, 2010. **179**(1): p. 49-56.

Chapter 6
Conclusions and Outlook

6.1 Conclusions

Multi-walled carbon nanotubes were treated with nitric acid and the protocol adapted produced a material that was significantly different from the as-received CNTs. The Raman analysis showed that nitric acid treatments removed amorphous carbons and introduces surface groups, the XRD characterizations also showed that functionalised CNTs were free from residual catalyst and amorphous carbons, the TGA showed that treating CNTs with acid enhances their thermal and oxidation properties. The sol gel method was successfully employed to produce mesoporous silica (SBA-15), mesoporous titania, and successfully coat MWCNTs with silica thin film. The physical-chemical properties of the SBA-15 were similar to what has been reported in the literature with a surface area of 661.59 m^2 g^{-1}, low angle reflections at 2θ = 0.94˚, 1.62˚ and 1.62˚, a classic hysteresis on the N2 isotherms showing capillary condensation in mesopores, and characteristic mesoporous channels seen with HRTEM. The mesoporous titania had a surface area of 207.75 m^2 g^{-1}, and a clear hysteresis with the isotherm that showed the catalyst had uniform pores. The SBA-15 on CNTs materials had high surface areas that increased directly proportional to SBA-15 coating. Thermal properties of the SBA-CNT composites were also enhanced as silica coating was increased on the CNT surface. Physical and chemical properties of the materials revealed that supporting TiO_2 particles on mesoporous materials could restrict the growth of the titania particle; increase the crystallinty, surface area, active sites and absorption edge; while decreasing electron – hole recombination rate, and band gap energy. The physical and chemical properties of the supports and composite materials confirmed that the sol-gel method was sufficient for the fabrication of nano-composites of enhanced properties.

Photo-catalytic de-coloration of methylene blue using TiO_2, TiO_2/SBA-15, TiO_2/CNTs and TiO_2/SBA-CNT catalyst revealed that anatase phase titania was effective in the de-coloration of pollutants using visible light.

The studies also showed that surface area, pore volume, band gap energy and e^- - h^+ recombination rates were not the only limiting factors to a highly efficient photo-catalyst. Mesoporous supports behave differently in catalysis because of their properties, in particular electronic properties.

Further investigations on the TiO_2/SBA-CNT composite showed that titania particles had different catalytic activities at different concentrations. An increase in titania content decreased the catalytic activity of the composite on MB tests. We attributed the catalytic activity to the crystallinity and electron – hole recombination rate of the catalyst systems. A different activity of the same catalyst systems was observed on the transformation of the herbicide 2-methy-4-chlorophenoxyacetic acid. The variation in the activity of the catalyst was attributed to the difference in the substrate structures which influenced the oxidative mechanisms during the photo-catalytic reaction.

The use the novel TiO_2/SBA-CNT catalyst showed that decreasing the band gap of titanium and increasing surface area does not always favor photo-catalytic de-coloration. However, composites of TiO_2 with electron trapping species such as carbon nanotubes reduces one of the core problems associated with TiO_2 semiconductor which is electron – hole recombination rate. Such composites offer the advantage of using the catalyst under visible light energy and the catalyst can be employed to de-colorize/degrade organic pollutants in solution medium. This study showed that organic pollutants with different properties cannot be effectively destroyed by one catalyst, this could be due to the photo-catalytic degradations mechanisms adopted by the different pollutants. However an efficient catalyst such as TiO_2/SBA-CNT remains inefficient in efficiently initiating pollutant degradation.

6.2 Outlook and challenges

Titania nano-particles are mainly activated by UV light, this pose challenges for indoor applications and means that titania catalysts that can be activated by visible wavelengths need to be developed. The most efficient systems with suitable substrate have to be identified for different applications in order to ensure maximal efficiency, activity, and longevity of the catalyst. Electron – hole recombination rate still remains a challenge in the efficiency of the catalyst. One way of addressing the challenge is through enhancing the catalyst properties which results from preparation methods. Methods such as sol-gel, ultrasound and chemical vapor can be employed. The method selection can be complimented with careful choice of precursors that are less expensive and obey the green chemistry principles. Another challenge is the use of titania nano-particle for inorganic environmental remediation applications.

Research needs to be focused on these titania nano-materials for environmental remediation from organic and inorganic pollutants. Developments on efficient catalyst will require technology developments for reactors that will immobilize the catalyst and maximize its efficiency at industrial scale. Such efficient catalysts will also require lab scale research to test their efficiencies on water bodies that have multi-component pollutants. Such waters can be sampled from waste or potable water plants. The most desirable developments would be that of finding alternative, inexpensive, recyclable and less toxic structure directing agents which will be used during synthesis strategies. Distinct research into the catalyst's photo activity needs to be performed to facilitate the development of catalysts that will be efficient on multiple organic pollutants. A catalyst system such as TiO_2/SBA-CNT requires synthetic methods engineering which will allow the catalyst to be effective irrespective of pollutant structure. The current study showed that the catalyst system has limitations of their effective application to different pollutants. However, the catalyst's physical-chemical properties, ease of recovery after use are desirable for a photo catalyst. Further research relating to TiO_2/SBA-CNT catalyst may be focused on studying the effect of SBA-15 concentrations on the photo-catalytic activity of the catalyst. Also, experiments on hydroxyl radical generation of the catalyst should be considered in order to account for the catalyst activity for degradation of different pollutants.

Manuscripts are being prepared for submission under the titles:

"Photo-catalytic Properties of Anatase TiO_2 supported on CNTs, SBA-15 and silica coated MWCNTs nano-hybrid" and

"Photocatalytic activity of TiO_2 supported on SBA-15 coated CNTs composites"

Appendices

Dosimetry and Critical Micelle Concentration Data

A 1.1 Dosimetry Results for OH Radical Generation using Terephtalic Acid

Hydroxyl radical generation experiments were carried from chemical dosimetry chemistry based on terephtalic acid (TA). Aqueous solution of TA was prepared from 2 mM TA and 5 mM NaOH dissolved in de-ionized water. Fluorescence spectrophotometer was used for measurements at wavelengths ranging from 300 – 600 nm with an excitation wavelength at 310 nm. The rest of the parameters were set the same as in the PL studies (**section 3.2.6)**. Similar photo-catalytic experiments to those described in **Section 3.4** were followed with the use of terephtalic acid instead of methylene blue. These results were not discussed in the dissertation because the results are not conclusive and not reproduced due to the catalyst materials running out. The aim of the dosimetry experiment was to determine the amount of OH radicals produced during photo-catalytic test for the respective catalysts.

Figure A1 show that commercial TiO_2 which is denoted P25 produces a lot of OH radicals as compared to the other catalyst. These suggest that P25 is likely to photo-catalytically perform better that the other catalyst. This is postulated because it is reported that the pollutants are degraded by OH radical species which are produced during the catalysis reaction.

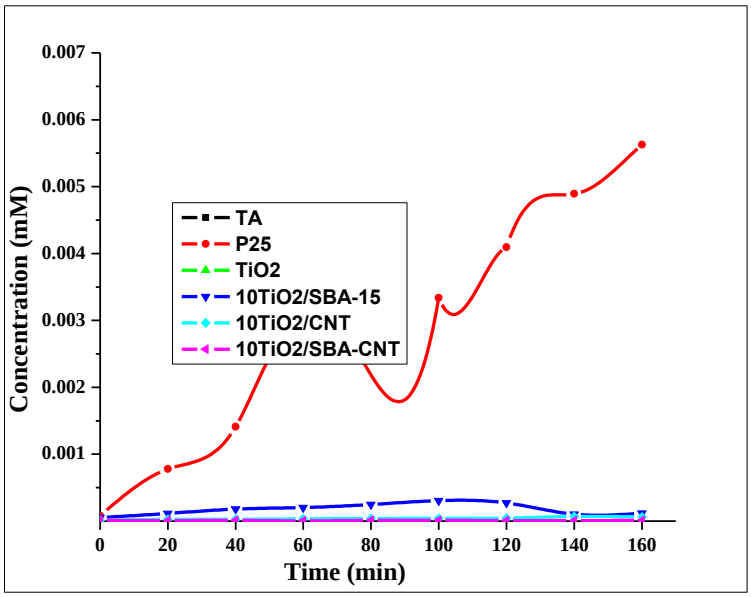

Figure A1. Graph showing the amount of OH radicals generated during photo-catalytic experiments for respective catalysts (comparison with commercial Degussa P25 TiO_2).

Figure A2 shows the magnified OH radical generation data from Figure 1. The 10 wt. % TiO_2/SBA-15 catalyst has the maximum concentration of terephtalic acid, this suggest that the composite produces the most OH radicals as compared to the other TiO_2/CNT and TiO_2/SBA-CNT composites.

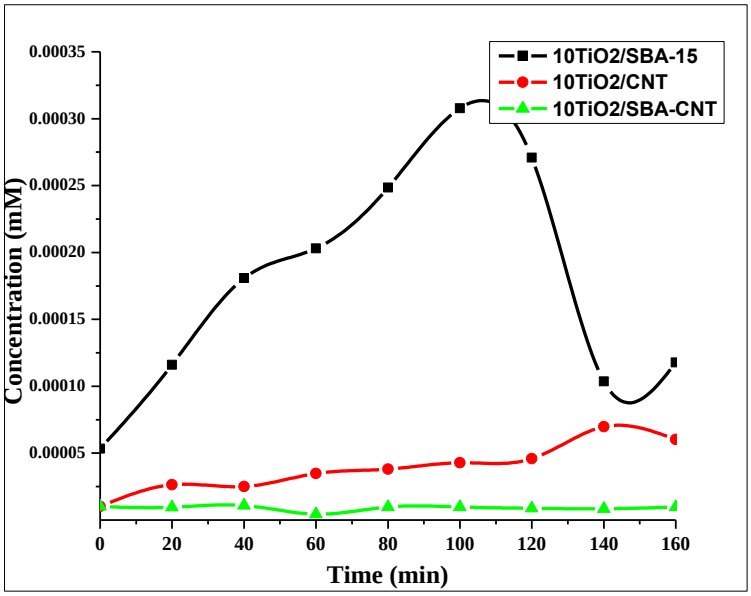

Figure A2. Graph showing the amount of OH radicals generated during photo-catalytic experiments for respective catalysts.

A 1.2 Experimental Calculations

These calculations refer to synthetic methods found in section 3.3.3.

The amounts of TEOS used during the respective experiments were calculated according to **equation 1.** The preparation of 10 wt. % SBA-15 on CNTs is used below to illustrate the calculations followed for the other 20 and 30 wt. % SBA-CNT composites.

$$\frac{xSBA\ 15}{xSBA\ 15 + 0.5g\ aCNTs} = 10\% \qquad (1)$$

$$0.1x + 0.05 = xSBA\ 15$$

x = 0.0555 g SBA-15 will be prepared if 0.5 g of aCNTs is to be employed at the beginning of the synthesis. However, since SBA-15 does not exist as a starting material, the precursor TEOS has to be used to prepare the 0.0555 g SBA-15. To calculate the volume of TEOS **equation 2**and **2**were considered.

$$n_{(SBA\text{-}15)} = \frac{m}{Mr} \qquad (2)$$

$n_{(SBA\text{-}15)} = \frac{0.0555\ g}{60.08\ g/mol} = 0.925 \times 10^{-3}$ moles of SBA-15 are in 0.0555 g SBA-15.

So: 1 mol SBA-15 = 1 mol TEOS

$m_{(TEOS)} = n \times Mr_{(TEOS)}$ (3)

$= 0.925 \times 10^{-3} \times 208.33\ g\ mol^{-1}$

= 0.193 g TEOS precursor was employed during the synthesis of 10 wt. % SBA-15 coated CNTs.

These calculations refer to synthetic methods found in section 3.3.6.

The preparation of the 10 wt. % TiO_2 on SBA-15 coated aCNTs is used below to illustrate the calculations followed for the 5 and 20 wt. % TiO_2/SBA-CNT composites.

$$\frac{xTiO_2}{x + 0.8\ g\ SBA{-}CNT} = 10\% \qquad (4)$$

$$0.1x + 0.08 = xTiO2$$

x = 0.0888 g TiO_2 will be prepared if 0.8 g of the SBA-CNTs is to be employed at the beginning of the synthesis. However, since TiO_2 was to be prepared from the precursor TIP, further calculations where necessary to find out the mass of TIP required to getting the desired amount of 0.0888 g TiO_2. To calculate the mass of TIP **equation 5 – 6** were considered.

$$n_{(TiO2)} = \frac{m}{Mr} \qquad (5)$$

$n_{(TiO2)} = \frac{0.0888\ g}{79.88\ g/mol}$ = 1.1117×10^{-3} moles of TiO_2 are in 0.0888 g of TiO_2.

So: 1 mol TiO_2 = 1 mol TIP

$$m_{(TIP)} = n \times Mr_{(TIP)} \qquad (6)$$

$= 1.1117 \times 10^{-3} \times 284.22$ g mol^{-1}

= 0.3160 g TIP precursor was employed during the synthesis of 10 wt. % TiO_2/SBA-CNT composite.

Appendix A 1 has instrumental data and workbooks referred to in Chapter 3. The folders in the appendix are provided as a disc and they appear as:

A 1.1 OH Radical Generation Experimental Results

A 1.2 OH Radical Generation Experimental Data

A 1.3 CMC Experimental Data and Figures

A 2 Characterization Data on rCNTs, aCNTs, SBA-15 and SBA-CNT composites

Appendix **A 2** has folders with instrumental data and workbooks for the results presented in **Chapter 4**. The folders in the appendix are provided as a disc and they appear in the order:

Folder A 2.1 Characterization Data for Section 4.1 (rCNTs, aCNTs, SBA-15 and SBA-CNT composites). In this folder, subfolders appear as:

- A 2.1.1 Electron Microscopy
- A 2.1.2 Nitrogen Sorption Studies
- A 2.1.3 Raman Spectroscopy
- A 2.1.4 Thermo-gravimetric Analysis
- A 2.1.5 X-Ray Diffraction

Folder A 2.2 Characterization Data for Section 4.2 (10 wt. % TiO_2 on SBA-15, CNTs and SBA-CNT composite respectively). In this folder, subfolders appear as:

- A 2.1.1 Electron Microscopy
- A 2.1.2 Nitrogen Sorption Studies
- A 2.1.3 Photoluminescence Spectroscopy
- A 2.1.4 Raman Spectroscopy
- A 2.1.5 UV-Vis Diffuse Reflectance
- A 2.1.6 X-Ray Diffraction

Folder A 2.3 Characterization Data for Section 4.3 (5, 10 and 20 wt. % TiO_2/SBA-CNT). In this folder, subfolders appear as:

- A 2.1.1 Electron Microscopy
- A 2.1.2 Nitrogen Sorption Studies
- A 2.1.3 Photoluminescence Spectroscopy
- A 2.1.4 Raman Spectroscopy

A 2.1.5 Thermo-gravimetric Analysis

A 2.1.6 UV-Vis Diffuse Reflectance

A 2.1.7 X-Ray Diffraction

A 3 Photo-Catalytic Studies

Appendix A 3 folder has photo-catalytic studies instrumental data and workbooks. The folders in the appendix are provided as a disc and they appear in the order:

Folder A 3.1 Methylene blue studies workbook.

Folder A 3.2 MCPA transformation studies

A 3.2.1 MCPA transformation HPLC instrument data files